Title

A Study of Mid-Latitude Clouds in Saturn's Moon, Titan: Phenomenology, Dynamics and Persistence

Permalink

https://escholarship.org/uc/item/6fc1k382

Author

Arias-Young, Tersi Marcela

Publication Date

2021

Peer reviewed|Thesis/dissertation

UNIVERSITY OF CALIFORNIA

Los Angeles

A Study of Mid-Latitude Clouds in Saturn's Moon, Titan:

Phenomenology, Dynamics and Persistence

A dissertation submitted in partial satisfaction

of the requirements for the degree

Doctor of Philosophy in Atmospheric and Oceanic Sciences

by

Tersi Marcela Arias-Young

2021

ABSTRACT OF THE DISSERTATION

A Study of Mid-Latitude Clouds in Saturn's Moon, Titan:

Phenomenology, Dynamics and Persistence

by

Tersi Marcela Arias-Young

Doctor of Philosophy in Atmospheric and Oceanic Sciences

University of California, Los Angeles, 2021

Professor Jonathan Lloyd Mitchell, Chair

Saturn's largest moon, Titan, provides a new perspective on planetary climate. It is larger than Mercury, has a 16-day rotation period, 29.5-year annual cycle, and a ~1.5-bar nitrogen atmosphere. Titan has a fully developed atmosphere, analogous to that of Earth, and methane plays a similar role to water in the hydrological cycle on our planet, generating clouds, storms and precipitation. Titan's clouds have been under investigation since their detection in 1995 with ground-based telescopes and were observed in detail during the Cassini-Huygens mission to the Saturn system. "Cassini" orbited Saturn and its moons from 2004 to 2017, giving unparalleled views that have led to countless discoveries and clouds are one of many fascinating Titan phenomena revealed by it. To this day, cloud formation mechanisms, dynamics and duration of the associated storms are still not fully understood and are the subject of ongoing study.

The central goal of this work is to provide a general physical interpretation of observed storms and their relation to atmospheric dynamics of the moon. Two previous studies are the foundation for this research: Mitchell et al. (2011), who developed a process for interpreting Titan's cloud

morphologies and precipitation through a combined analysis of observations and general circulation model (GCM) simulations; and Turtle et al. (2011), who reported the first evidence of seasonal changes on the moon obtained from Cassini cloud data.

This dissertation presents a survey of Titan's mid-latitude clouds, as seen from space by the Cassini Imaging Science Subsystem (ISS) instrument, compares a subset of the observed clouds to the methane storms produced in a climate model of Titan, and infers the underlying storm dynamics by connecting the two. ISS is a multi-wavelength – ultraviolet to near-infrared – camera specifically designed to take high resolution images from the top of the atmosphere to the surface of Titan piercing through the thick haze located in the stratospheric layer of the moon, which typically blocks the view of tropospheric clouds underneath it.

This study starts with an analysis of the physics of clouds applied to Titan's conditions and a microphysical cloud scheme to show how the abundant haze particles in the atmosphere are likely the seeds for methane droplets that catalyze cloud formation. Next, the ISS image archive is searched for cloud phenomena and various types of storms are surveyed. This is followed by Image processing, that require the conversion of raw images into maps with global locations of the clouds and the production of enhanced views of cloud features against the surface background to reveal their morphology. We then search for storms with temporally resolved observations and use their spatio-temporal distributions to identify the atmospheric dynamics behind them, including Rossby and gravity waves. Although many clouds/storms are identified, only two of them provide clear spatial and temporal information that allow this type of analysis.

The manuscript then pivots to analysis of methane storms in model simulations of Titan's climate using the Titan Atmosphere Model (TAM; Lora et al. 2015) with full surface hydrology (Faulk et al., 2019). The spatio-temporal features of observed clouds combined with the simulated storms

at the same season as the observations suggest that just as waves organize storms on Earth, they do so on Titan as well. The results of the study strongly indicate that Titan's cloud formation and propagation are associated with Rossby and equatorial Kelvin waves, and perhaps combinations thereof, and that the clouds/storms can persist for weeks and perhaps much longer as they propagate around the moon's globe – a phenomenon referred to in this work as "persistence". These findings offer a glance into the complex phenomenology, dynamics and persistence of Titan's clouds. The methodology developed in the course of this work for comparing the spatio-temporal distribution of observed clouds to analog storms in TAM is novel, while also being consistent with previous studies focused either on the spatial distribution or seasonal evolution of observed clouds. Future missions to Titan, including the funded Dragonfly mission, will facilitate further model-data comparisons, for instance the long-term persistence of the Kelvin wave in TAM. This methodology, documented in detail in a "cookbook", provides a set of useful tools and guidance for future explorations of the clouds and storms of Titan.

The Dissertation of Tersi Marcela Arias-Young is approved.

Jochen Peter Stutz

David A. Paige

Aradhna K. Tripati

Jonathan Lloyd Mitchell, Committee Chair

University of California, Los Angeles

2021

I dedicate this dissertation to my husband, Jack, my partner in science and life.

TABLE OF CONTENTS

xv

LIST OF TABLES

ACKNOWLEDGEMENTS

I would like to thank my very dedicated advisor Jonathan Mitchell for his endless guidance and support throughout this research project. This dissertation is not solely the product of my work but also the hard work and perseverance of my advisor, who patiently provided his help to keep me going even in the most difficult of times to get the project done. I am honored to have worked with such an inspiring scientist and glad to know more students had and will continue having the opportunity to work with and learn from him.

I also would like to give special thanks to the members of my dissertation committee – Dr. Jochen Stutz, Dr. David Paige, and Dr. Aradhna Tripati – who made themselves available when I needed them to review previous drafts of this dissertation, for their valuable suggestions during my defense that helped me bring this work to its completion, and for their open-ended support of my future academic endeavors. Additionally, I express my appreciation to the UCLA Atmospheric and Oceanic Sciences department for giving me the opportunity to join their ranks and be part of it. In particular, I owe gratitude to the Chair of my department, Dr. Suzanne Paulson, and the current and former Student Affairs Officers, Denise Lopez and Kimberly Perez for their constant help and support.

I would like to acknowledge the most important people in my life – my family. My extraordinary parents, Maria and Luis (Verita), my amazing siblings and niece, Andrea, Alejandro, Adrian, Susana and Anais, whose unconditional love and support gave me the strength to follow my dream of becoming a scientist. Their words of encouragement and their belief in my potential allowed me to never give up and become the first woman to obtain a degree in my family, even continuing to earn a PhD. Thank you all from the bottom of my heart.

The support I have received over the years does not end there, and I wish to further acknowledge everyone who has been involved with and contributed to my success. My extended family, Ana, Maisa, Ryan and Mayu. My wonderful in-laws, John, Luisa, John Oliver, Bobby, Patsy and Theresa, and in particular my phenomenal mother in-law, Erica, whose absolute love, endless support and cheering words always uplift me.

A special thanks to my fantastic friends Bea and Victor, who generously dedicated time to ensure I could get through the last steps of my defense by giving me their sincere advice and their limitless support. And, to all my dearest friends who have accompanied me on this journey, Baird, Prudence, Alex, Jayshri, Gautam, Aurore, Cyril, Maren and Ron. Thank you for bringing enjoyment and happiness to my life and for your heartfelt support.

Above all, I want to thank and I dedicate this work to my husband, Jack, whose infinite love, continuous support, and whose shared passion for science has provided me with a fascinating way to integrate my personal and professional life in a way I never envisioned I would, with the best partner one could ever have. Since the moment we met in the Physics and Astronomy Department at San Francisco State University he has been my partner in science and life and I can honestly say I would not have completed this endeavor without him.

Tersi Arias-Young

Camarillo, California

September, 2021

EDUCATION

2013	M.S., University of California, Los Angeles
	Atmospheric and Oceanic Sciences
2012	M.S., California State University, Northridge
	Physics
2007	B.S., San Francisco State University
	Astrophysics, Cum Laude

ACADEMIC EMPLOYMENT

2017 – 2021	Astronomy Adjunct Faculty, Santa Monica College, CA
2010 – 2019	Teaching Assistant/Associate/Fellow, AOS, UCLA
2011 – 2015	Research Assistant, TPACE group, EPSS, UCLA
2009 – 2010	Research Assistant, Physics and Astronomy, CSUN
2008 – 2010	Telescope Operator and Researcher, San Fernando Observatory, CSUN
2007 – 2010	Teaching Assistant/Lab Instructor, Astronomy, CSUN
2004 – 2007	Research Assistant, Astronomy Cool Group, SFSU

AWARDS

2019 – 2020	Dissertation Year Fellowship, Graduate Division, UCLA
2011	Morris Neiberger Award – Excellence in graduate teaching, AOS, UCLA
2010	APPT Outstanding Astronomy TA Award, CSUN
2004, 2007	Eden Award – Outstanding academic achievement in BS physics, SFSU

PUBLICATIONS

Arias-Young, T., Mitchell, J. L. (*In Preparation*) Phenomenology, Dynamics and Persistence of Mid-Latitude clouds on Titan: Observations to Model Connection.

Cool, A. M., Haggard, D., **Arias, T**., Brochmann, M., Dorfman, J., Gafford, A., & Anderson, J. (2013). HST/ACS Imaging of Omega Centauri: Optical Counterparts of Chandra X-Ray Sources. *The Astrophysical Journal*, *763*(2), 126.

Jensema, R. J., **T. M. Arias-Young**, A. N. Wilkins, A. Ermakov, C. Bennett, A. Dietrich, D. Hemingway et al. "Core to Atmosphere Exploration of Ice Giants: A Uranus Mission Concept Study." In *AGU Fall Meeting Abstracts*, vol. 2014, pp. P23A-3967. 2014.

Arias, Tersi Marcela. *Search for super-saturation in late-type stars*. MS Thesis. California State University, Northridge, 2012.

Christian, D. J., Mathioudakis, M., **Arias, T**., Jardine, M., & Jess, D. B. (2011). The Search for Super-saturation in Chromospheric Emission. *The Astrophysical Journal*, *738*(2), 164.

Chapman, G. A., Dobias, J. J., & **Arias, T**. (2011). Facular & Sunspot Areas During Solar Cycles 22 and 23. *The Astrophysical Journal*, *728*(2), 150.

Haggard, D., Cool, A. M., **Arias, T**., Brochmann, M. B., Anderson, J., & Davies, M. B. (2010). A Deep Multiwavelength View of Binaries in Omega Centauri. *arXiv preprint arXiv:1012.3647*.

Arias, Tersi M. *A Catalog of Candidate High-redshift Blazars for GLAST*. No. SLAC-TN-2006-025. United States. Abstracts for Summer Internship catalog for the Department of Energy, 2006.
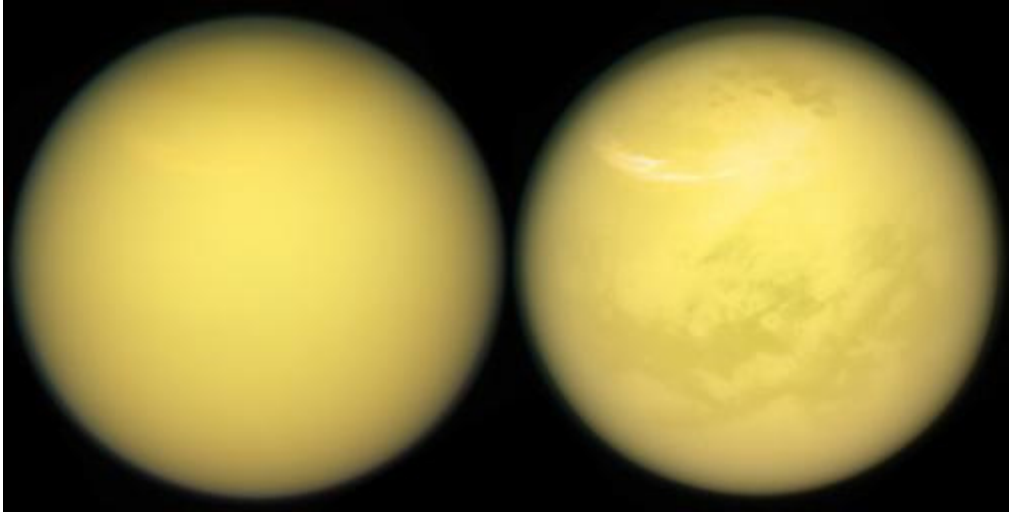
Figure 1.1: Two views of Titan showing its thick haze (left) covering what lies beneath where surface features are seen, together with clouds forming on the tropospheric layer (right). [Image credit: NASA/JPL-Caltech/Space Science Institute]

CHAPTER 1

Introduction and Background

1.1 Introduction

Titan, the largest moon of Saturn, is surrounded by an extensive gas layer, and it is the only moon known to have a substantial atmosphere. Titan's dense atmosphere consists mainly of nitrogen, as Earth's, but with a higher surface pressure, and a much lower surface gravity.

First discovered by Dutch astronomer Christiaan Huygens in 1655, Titan has been observed ever since from Earth and space. However, before the arrival of the spacecraft mission Cassini-Huygens in mid-2004, all that could be seen was an orange world surrounded by a hazy layer that blocked most of the visible light (Figure 1.1 - left). Cassini-Huygens exposed surface features and cloud formations (Figure 1.1 - right) that were hidden by that dense photochemical

haze, whose main layer terminates about 300 kilometers above Titan's surface.

Perhaps one of the most interesting aspects of Titan having an atmosphere is the formation of clouds. Although the reason why Titan has a fully developed atmosphere is still unknown, what we do know is that methane plays a similar role on Titan as water on Earth, causing similar meteorological processes such as cloud formation.

1.2 Titan Data

1.2.1 General Characteristics

Titan undegoes synchronous rotation around Saturn, with a < 1° orbit inclination, and it revolves around the Sun, along with the Saturn system, every 29.5 years. Saturn's axial tilt of ~27°, with respect to the ecliptic, gives rise to a seasonal cycle on Titan. Figure 1.2 shows a diagram of Titan's path around the Sun, seasons' dates, and the chronology of the Voyager and Cassini-Huygens
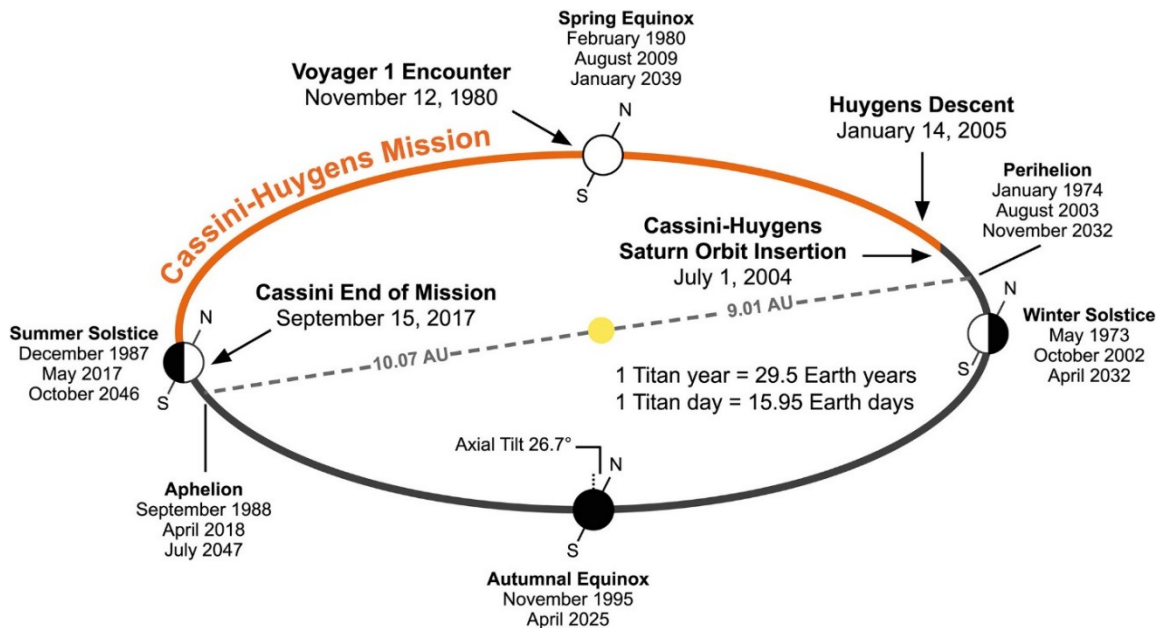
Figure 1.2. Schematic of Titan's orbit around the Sun, which notes season dates (each ~7 years long) and chronology of the Voyager mission visit (flyby) and the length and timing of the Cassini-Huygens space mission. [Image Credit: Hörst, S.M, 2017]

missions that have visited Saturn's largest moon.

Titan's measured physical characteristics are listed on Table 1.1, which shows the most useful and important data of Titan obtained from space missions such as Voyager 1 and, most recently, from Cassini-Huygens. Values are compared to Earth's.

Characteristic	Titan	Earth
Surface gravity (m s^{-2})	1.35	9.8
Heliocentric semimajor axis (AU)	9.54	1
Heliocentric period (yr)	29.5	1
Length of day (day)	15.95	1
Eccentricity	0.029	0.0167
Axial tilt	26.7°	23.4°
Bond albedo	0.2	0.29
Effective temperature (K)	82	255
Mean surface temperature (K)	94	288
Surface pressure (bar)	1.467	1.013
Surface air density (kg m^{-3})	5.3	1.2
Column density (km am)	92	8
Specific heat, c_p (J K^{-1}kg^{-1})	1100	1040
Dry adiabatic lapse rate (K/km)	1.26	9.8
Moist adiabatic lapse rate (K/km)	0.6	5.5
Surface saturated mixing ratio	0.114	0.017
Heat of vaporization (J/kg)	0.51×10^6	2.5×10^6
Pressure scale height (km)	20	8.4
Brunt-Vaisala frequency (s^{-1})	3×10^{-3}	5×10^{-3}
Surface condensable (m)	~1	2,700
Atmosphere condensable (m)	5	0.026

Table 1.1 **Titan's physical characteristics** and atmospheric properties from Cassini-Huygens measurements [Müller-Wodarg et al., 2014]. Some of these values were known before the Cassini-Huygens mission and were confirmed by the new measurements. Earth characteristics are included for comparison.

1.2.2 Cassini-Huygens

The data used in this research study come from the Cassini-Huygens mission, a joint robotic

spacecraft mission that was launched in 1997 and entered into orbit around the Saturn system on July 1, 2004. While the Cassini spacecraft was built to orbit Saturn and its moons and take data with its numerous instruments, the Huygens probe was designed to enter the atmosphere of Titan and land on its surface while taking data on its way down.

1.2.3 Huygens – Atmospheric Composition, Vertical Flow, Density and Temperature Profiles
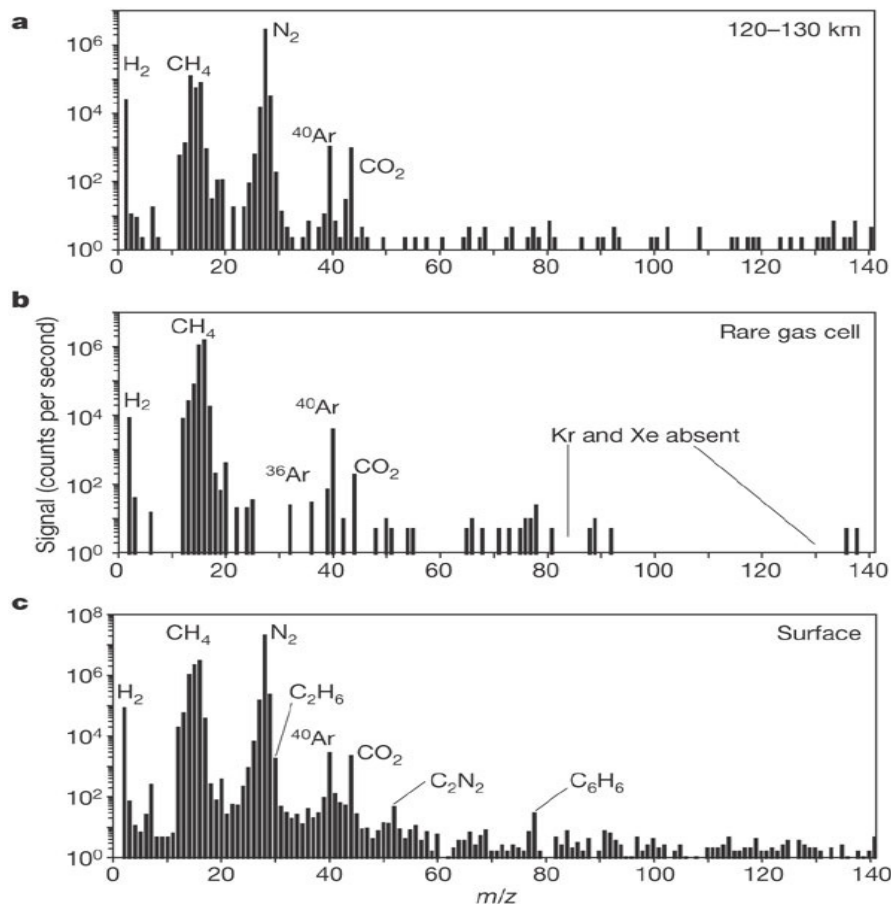
Figure 1.3. The abundances of constituents of Titan's atmosphere from the Gas Chromatograph Mass Spectrometer, (GCMS) instrument on the Huygens probe [Niemann et al., 2005]. a. An upper atmosphere spectrum from altitudes of approximately 120 to 130 km, averaging 104 mass spectra over 244 sec. b. The rare-gas cell measurements (about 75–77 km, averaging 43 mass spectra over 81 sec), showing the lack of heavy primordial noble gases. c. A surface spectrum (432 mass spectra), averaged over 70 min from surface impact until loss of signal.

The Huygens probe, built by the European Space Agency, was designed to study the composition and structure of Titan's atmosphere and to collect information about Titan's surface. It made detailed measurements of atmospheric composition as it descended on the moon, as seen in Figure 1.3).

Huygens collected data that have allowed scientists to determine the vertical component of atmospheric flow on Titan as measured by the Huygens Atmospheric Structure Instrument, or HASI (Figure 1.4), the density with respect to height (Figure 1.5), and the temperature as a function of pressure and height (Figure 1.6) to show how Titan's variation of vertical temperature defines the layers of its atmosphere (Figure 1.7).
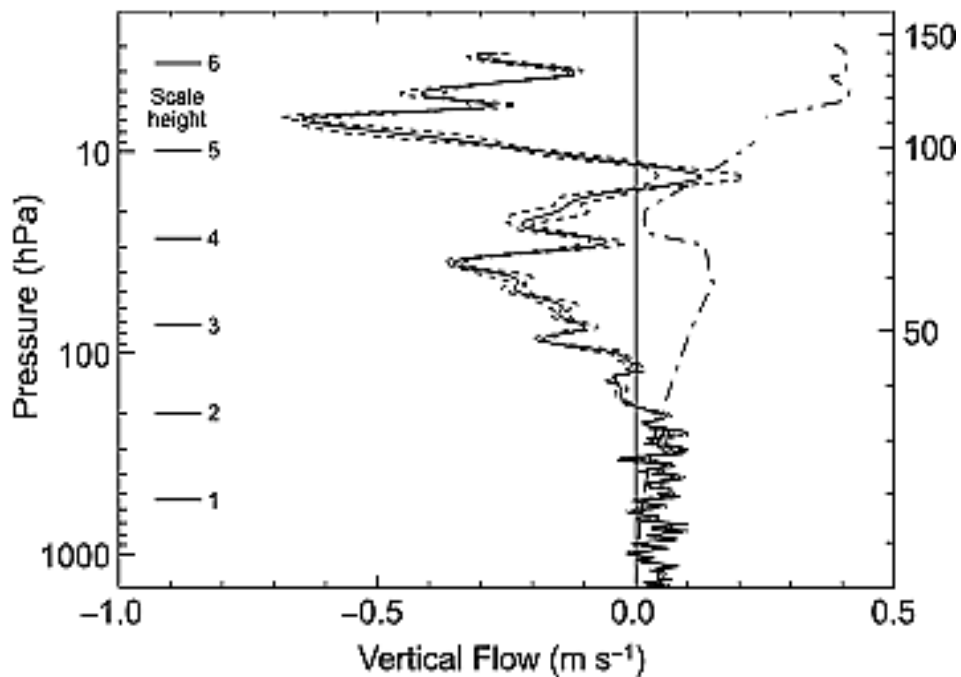
Figure 1.4. The vertical component of the atmospheric flow on Titan along the descent trajectory of the Huygens probe, with error margins based on estimated instrument performance [Fulchignoni et al., 2005], and the horizontal component derived from radio telemetry [Bird et al., 2005], scaled down by a factor of 1/250 for easier comparison (dash-dotted line).
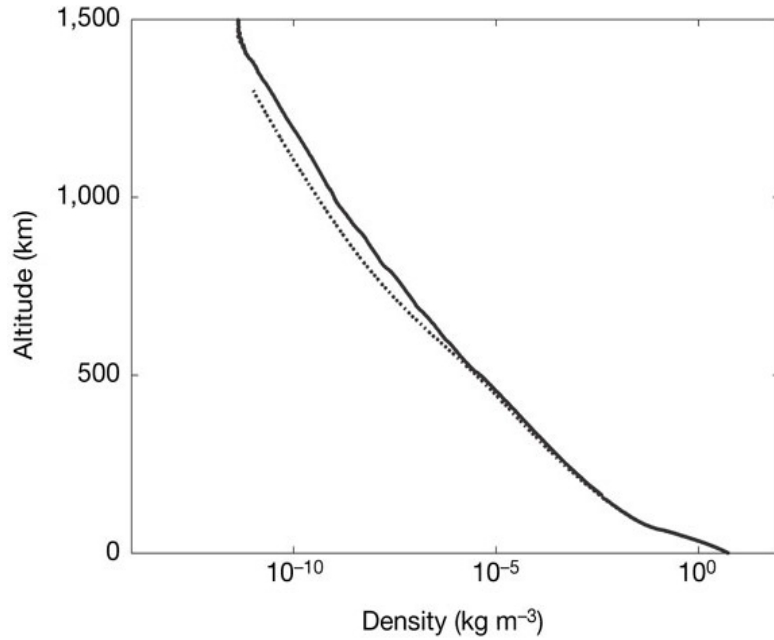
Figure 1.5. The atmospheric density profile of Titan as derived from HASI measurements (solid line) is shown in comparison with the engineering model of Titan's atmosphere derived from Voyager 1 data (dashed line).
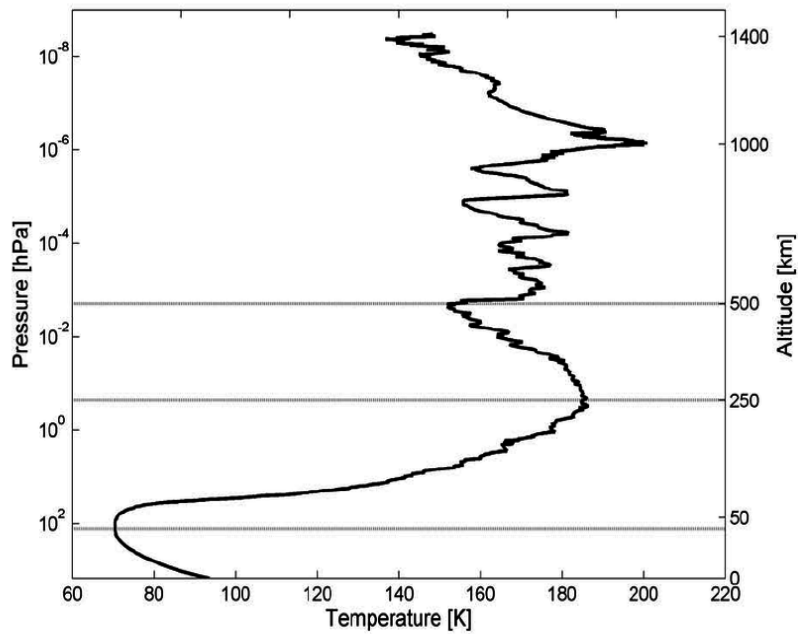
Figure 1.6. Titan's temperature profile as derived from Huygens/HASI measurements. [Fulchignoni et al., 2005]. Image Credit: ESA
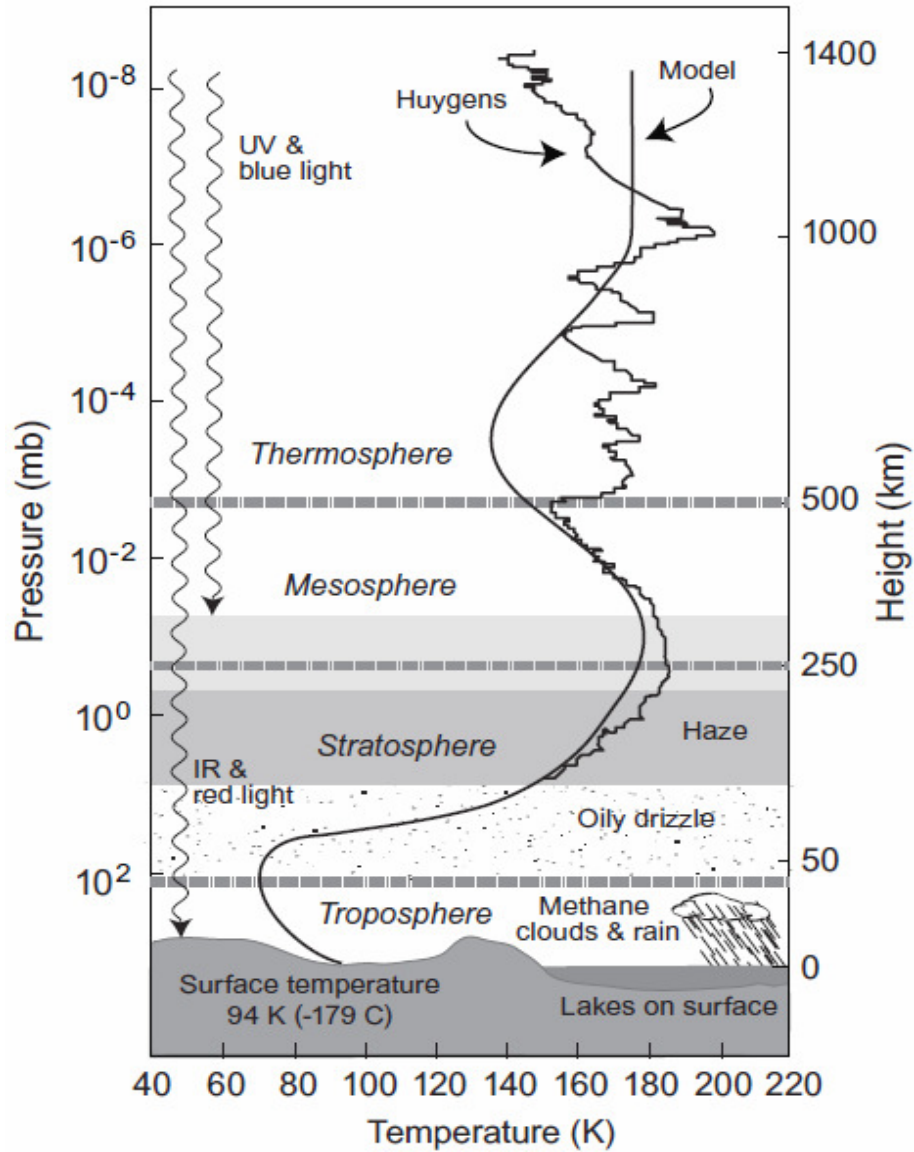
Figure 1.7. Titan atmospheric temperature profiles from Huygens descent measurements [Fulchignoni et al., 2005] superposed on a model atmosphere based on global measurements by infrared remote sensing. The variation of vertical temperatures on Titan defines the layers of its atmosphere (as on Earth) [Taylor, 2010].

Huygens also took images of the surface terrain, with its Descent Imager Spectral Radiometer (DIRS), which revealed fluvial features that indicate precipitation (Figure 1.8), and precipitation indicates the existence of storm clouds.
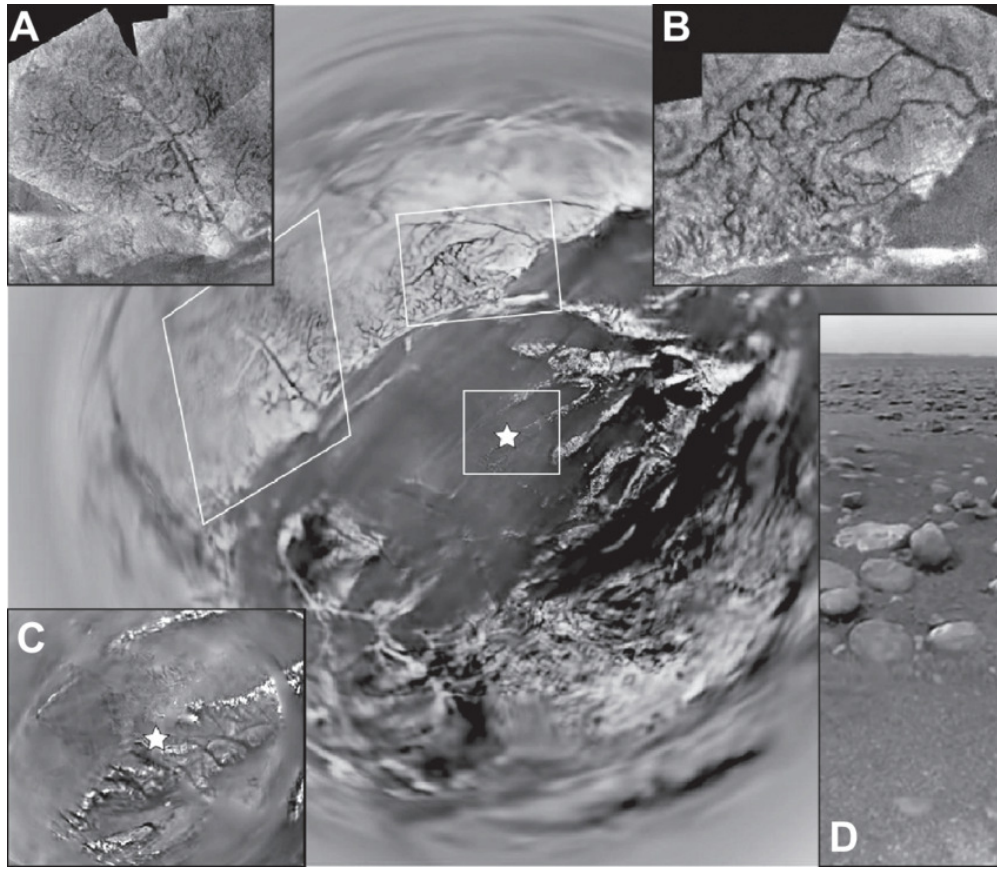
Figure 1.8. Huygens (DISR) mosaics of features around the Huygens probe landing site, at ~10°S, 168°E. Background: view from 6 km above the surface, centered on the landing site, marked with a star. North is up. Scale varies across image. White boxes are insets A-C. Insets: (A) Western drainage networks. Width is ~8 km. (B) Northern drainage networks. Width is ~6 km. (C) Stereographic projection of the landing site from 600 m above the surface. Width is ~2 km. (D) View from the landing site, looking toward the horizon. Diameter of the largest clasts in middle distance is ~15 cm. Dark zones stretching suggest scour tails.

1.2.4 Cassini - Cloud Data

On its way around the Saturn system, Cassini pointed at Titan for periods of 1 or 2 days every several weeks and observed the moon with an array of on-board instruments that could detect features at different altitudes from the top of the atmosphere to the surface. Some wavelengths of light penetrate farther into the atmosphere than others. Materials with different compositions preferentially absorb different wavelengths of light, so images at different wavelengths can

produce vertical maps of the atmosphere.

Cassini exposed surface and cloud features over Titan's globe never seen before, due to the moon's thick atmosphere, with instruments such as the Visual and Infrared Mapping Spectrometer (VIMS) and the Imaging Science Subsystem (ISS). The observational cloud analysis for this research work was solely completed with ISS data.

Titan's clouds are located low in the atmosphere, and they are best seen with the near infrared filter images (Figure 1.9). These raw images show the difference between data taken with the same pointing, only a few minutes apart, with two sets of near infrared filter combinations. If you look carefully, the cloud seen on the right is barely visible on the left image.
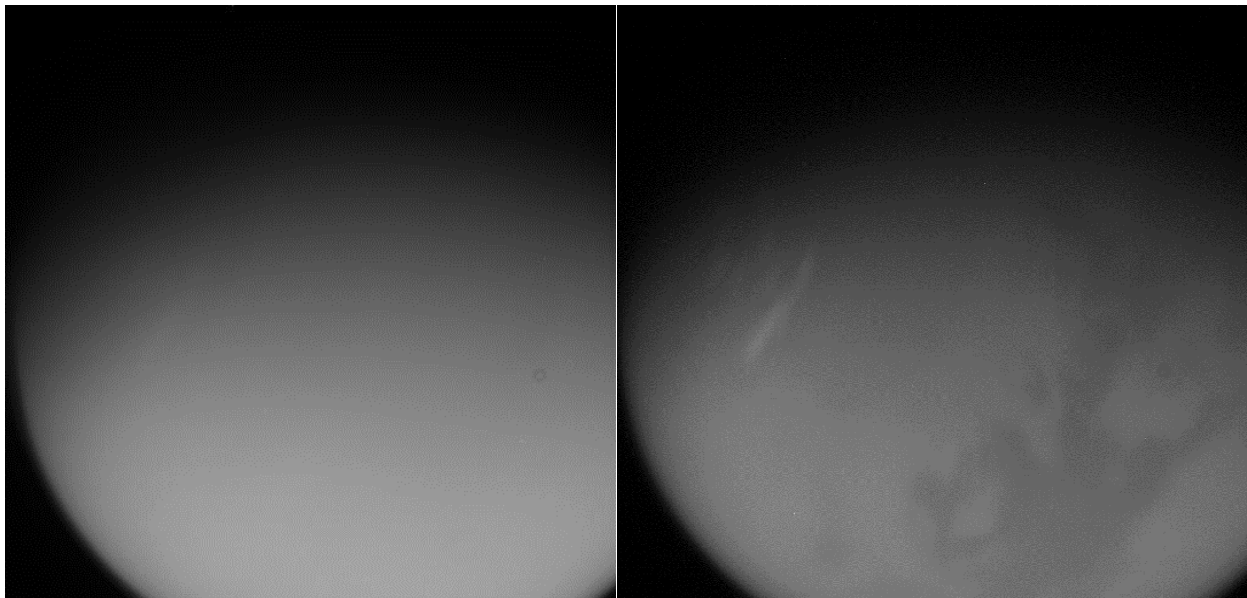
Figure 1.9. Titan seen from the Cassini–Huygens spacecraft on Sept. 23, 2009 – Left: (611-nm wide, 619-nm narrow). Right: (611-nm wide, 938-nm narrow). Images are taken 4 minutes apart.

1.3 Motivations and Previous Work

Two previous studies are the basis for this research: Mitchell et al. (2011), who developed a

process for interpreting Titan clouds' morphologies and precipitation through a combined analysis of observations and general circulation model (GCM) simulations; and Turtle et al. 2011, who reported the first evidence of seasonal changes on the moon when Cassini images showed a shift in cloud location as the seasons on the moon changed.

1.3.1 Mitchell et al.

In the 2011 paper titled "Locally Enhanced Precipitation Organized by Planetary-Scale Waves on Titan", Mitchell et al. demonstrate that planetary-scale Kelvin waves naturally arise in a new
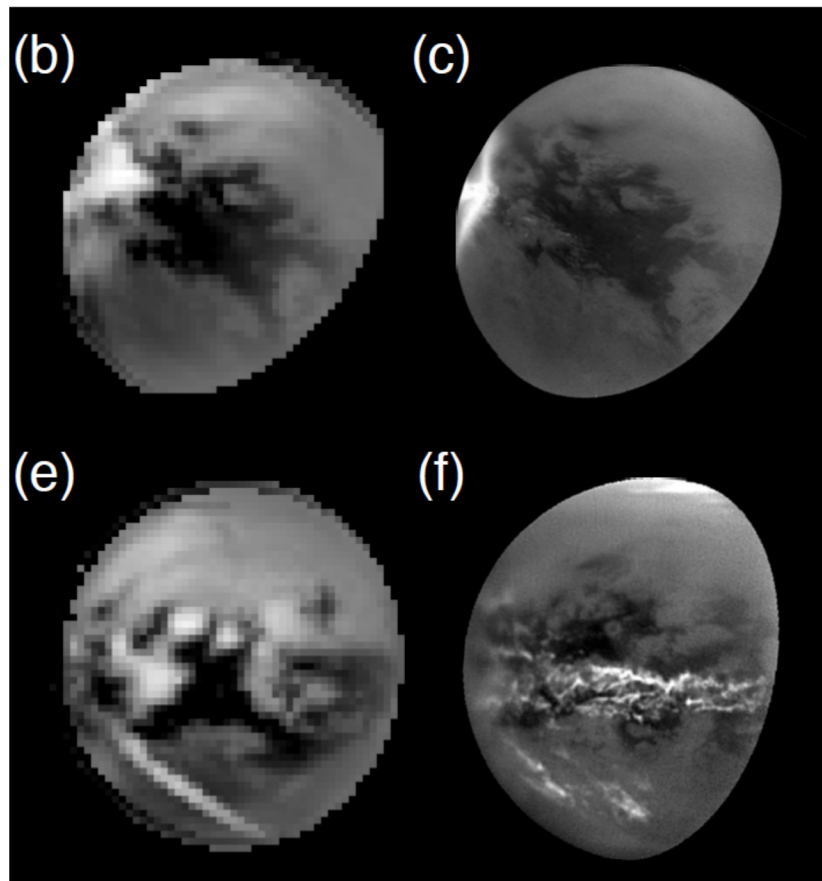
Figure 1.10. Simulated observations of two events during the equinoctial transition using GCM (b and e) and two cloud events observed by Cassini ISS: (c) a cloud shaped like a chevron at the equator pointing eastward was observed on 27 September 2010, followed on 18 October 2010 by (f) a streak of clouds extending southeastward from low-latitudes to high-latitudes [image credit: Mitchell et al., 2011].

three-dimensional version of their Titan GCM and organize convection into chevron-shaped storms at the equator during the equinoctial season, as seen in Cassini ISS observations from September 27, 2010. A second and much slower wave mode organizes convection into southern-hemisphere streaks oriented northwest-southeast, similar to another cloud observed on October 18, 2010 (Figure 1.10).

This work provides a general physical interpretation of observed storms, their relation to atmospheric dynamics and their aggregate effect on surface erosion through a combined analysis of cloud observations and the new and improved 3-D general circulation model simulations.

1.3.2   Turtle et al.

In the 2011 paper titled "Seasonal Changes in Titan's Meteorology", Turtle et al. report first evidence of seasonal shifts in locations of tropospheric methane clouds. They present observations of Titan's clouds (Figure 1.11), of different shapes found at varied latitudes from mid-2004 to the end of 2010, and show the changes in the temporal distribution and activity across the globe (Figure 1.12).

Titan's seasons have progressed from southern summer to early southern autumn since 2004, and changes in the distribution and activity of tropospheric methane clouds are observed in Figure 10. South-polar convective cloud activity, common in late southern summer, is found to become rare as autumn approaches, while north-polar and northern mid-latitude clouds appear during the approach to the northern spring equinox in August 2009.

The occurrence of clouds in northern mid-latitudes have implications for global circulation patterns. Turtle et al. compare two Titan circulation models that incorporate moist processes and document the seasonality of clouds and/or precipitation (Rannou et al.,

2006; Mitchell, 2008; Mitchell et al., 2009). Both models are two-dimensional, limiting their ability

to portray atmospheric variability, but the models incorporate different physics, leading to very

different predictions of the seasonal variation of clouds and precipitation; however, both models

produce clouds at the poles and in mid-latitudes, as observed by the Cassini ISS.
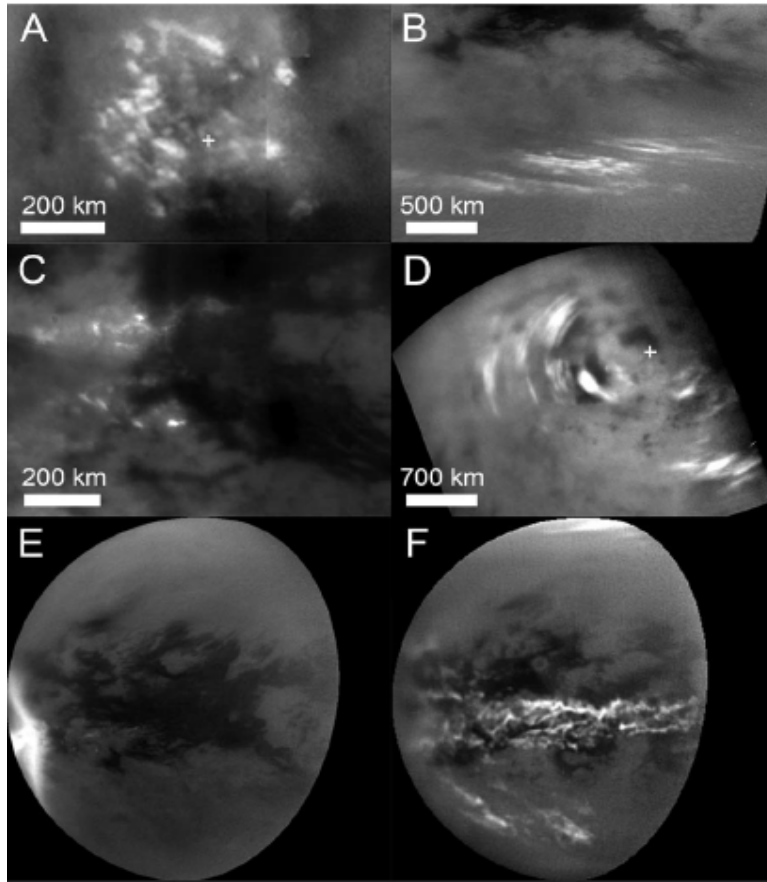
Figure 1.11. A. South-polar field of clouds, July 2004. B. Elongated streaks at southern mid-latitudes, Dec. 2009 (24-hour sequence). C. Discrete cells near ~15°S, Dec. 2006. D. Clouds at high northern latitudes, Sept. 2009 (24-hour sequence). E. Equatorial arrow-shaped cloud, Sept. 2010. **F**. Equatorial, southern mid-latitude & high-northern latitude clouds, Dec. 2009. Bright features are the tropospheric methane clouds; grey and darker shades are surface features. All images in Turtle et al. have been mapped and processed to enhance cloud features, as is done in this study.
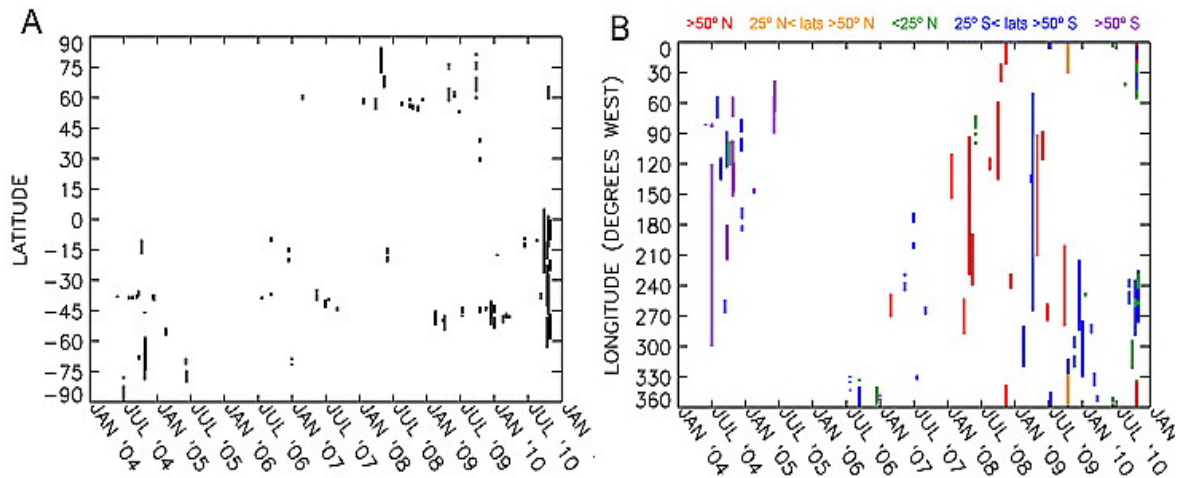
Figure 1.12. Latitudes (A) and longitudes (B) of clouds observed by ISS as a function of time through October 2010 (color indicates latitude range) (from Turtle et al., 2011)

1.4   This Work - Objectives and Organization of the Dissertation

The principal objective of this dissertation is the development of a physical understanding of the cloud formation and evolution under Titan's atmospheric conditions. This is accomplished by:

i.   Developing a microphysics model for the nucleation and growth of methane cloud droplets and cloud droplet size distribution to understand cloud formation under Titan's conditions (Chapter 2).

ii. Processing hundreds of Cassini cloud observations with image reduction and mapping to produce enhanced images of the cloud features that are plotted and analyzed (Chapter 3).

iii. Examining the morphology of the observed clouds to provide a general physical interpretation of the propagation of the observed storms and their relation to atmospheric dynamics of the moon, and comparing simulations with cloud observations to constrain these results (Chapters 4 and 5).

Chapter 2 begins with an analysis of the physics of clouds applied to Titan's conditions and a microphysical cloud scheme to show how the abundant haze particles in the atmosphere are likely the seeds for methane droplets that catalyze cloud formation. In Chapter 3, the methods employed to analyze the data are presented, starting with the image survey and each of the image processing steps that lead to the production of spatio-temporal plots. Included, also, is a brief introduction of the General Circulation Model that is used in chapter 5 as part of the analysis methods. Chapter 4 is dedicated to the study of a prominent cloud storm event from the observational data, which is the basis for most of the observational results and the primary connection with the model. Chapter 5 connects the work done with observations to simulations produced in a climate model of Titan to present the final findings. Chapter 6 is a summary of the findings of this dissertation, as well as proposed future work with both observational data and model simulations to continue exploring the clouds on Titan.

CHAPTER 2

Developments on the Microphysics of Methane Cloud Droplets

Figure 2.1. Earth clouds

2.1 Introduction to the Physics of Clouds

To understand Titan's clouds, it is imperative to develop a microphysical model for cloud nucleation and growth which requires an answer to the question of how cloud particles form in the first place.

Cloud physics is usually regarded as the study of the formation of clouds and the development of precipitation (Rogers, 1989). Clouds consist of a collection of droplets or ice crystals, not necessarily made of water, as on Earth. Lifting agents cause air containing vapor to

rise adiabatically and cool to its dew point, the temperature at which the air becomes saturated. Atmospheric pressure decreases with altitude and the rising air expands and cools, which reduces its capacity to hold the vapor. If the air is cooled and becomes saturated it normally sheds vapor it can no longer retain which condenses into a cloud. This begins to happen at the lifting condensation level (LCL), which roughly determines the height of the cloud base as depicted in Figure 2.2.
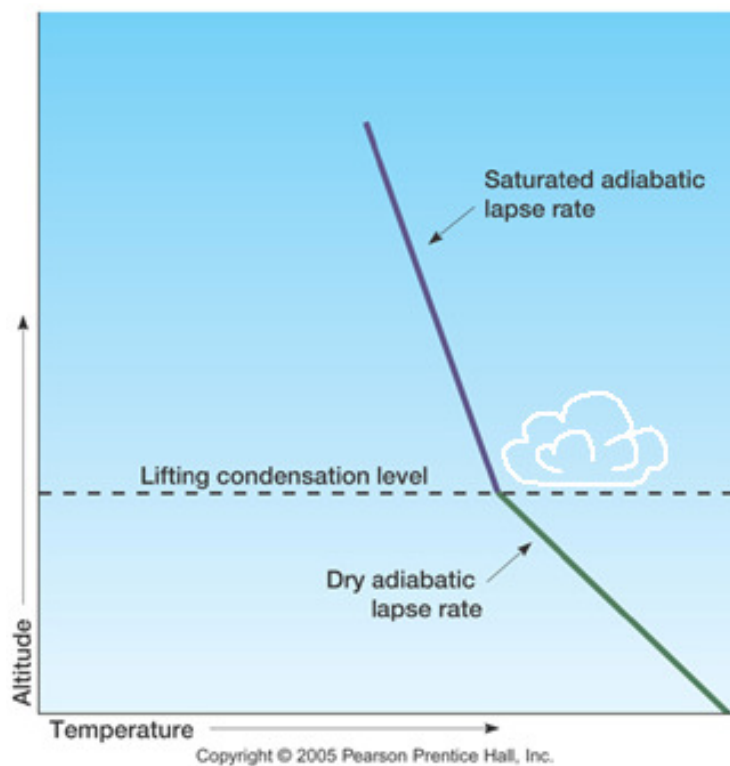
Figure 2.2. Diagram for cloud formation with cloud base at the LCL, the intersection of the dry and the moist (or saturated) adiabatic lapse rate – the rate at which atmospheric temperature decreases with an increase in altitude for dry and moist air – respectively [Image credit: Pearson Prentice Hall].

2.2 Cloud Droplet Formation

Cloud droplet formation requires phase changes. These transitions do not occur at thermodynamic equilibrium, but in the presence of a strong free energy barrier. The Gibbs free

energy, G, can be used to examine the thermodynamic stability of a system, and it is defined as:

$$G = U - TS + pV \ ,$$

Where p, V, S, T and U are the pressure, volume, entropy, temperature and internal energy of the system, respectively. A differential change in the Gibbs free energy is expressed as:

$$dG = dU + pdV + Vdp - TdS - SdT$$

where $\qquad\qquad\qquad dU = TdS - pdV$

Then: $\qquad\qquad\qquad dG = -SdT + Vdp$

If a system is in equilibrium at constant temperature and pressure, G is at its minimum.

Some phase changes require a nucleation process; for instance, ice nucleation or gas-to-particle formation of aerosols. Phase nucleation main categories for forming a new phase of a single compound (e.g., water) are homogeneous nucleation (uniform parent phase, no external agent) and heterogeneous nucleation (multiple phases, external agent involved) (Lamb et al., 2011).

2.2.1 Homogenous Nucleation

This type of nucleation involves the formation of droplets from vapor in a pure environment. Cloud water droplet formation requires several hundred percent supersaturation. The first step in the theory of homogeneous nucleation is to calculate the energy to form a molecular cluster of individual vapor molecules in the vapor phase (Figure 2.3). We expect that this energy of formation depends on cluster size and the concentration of vapor. We assume that the cluster is
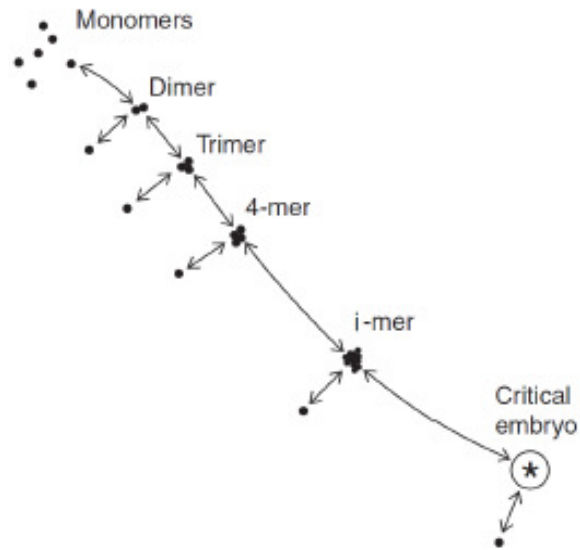
Figure 2.3. Nucleation process steps (Image credit: Lamb and Verlinde, 2011].

spherical and has the same surface properties as macroscopic droplets. We also assume constant pressure and temperature and that the cluster is in moist air with a vapor saturation ratio:

$$S = \frac{e}{e_s(T)}$$

where e is the water partial pressure and $e_s(T)$ is the equilibrium vapor pressure of pure, flat water at temperature T.

2.2.2 Kelvin Effect

The Kelvin effect is the change in vapor pressure of a species A due to a curved liquid/vapor interface with radius R_p. The vapor pressure of a curved surface is higher than that of a non-curved (or flat) surface. This effect relates saturation vapor pressure over the curved surface P_{env} to P_{sat} over the flat surface, where the saturation ratio, S:

$$S = \frac{P_{env}}{P_{sat}(\infty)}$$

In thermodynamic equilibrium $dG=0$ and G has a minimum and a maximum. We use the Gibbs free energy to derive Kelvin's equation starting with an initial number of molecules of vapor, N_T, considering the change in G, with the formation of a single drop of radius R_p, containing n molecules of the substance, and obtain:

$$\Delta G = G_{droplet} - G_{vapor}$$

$$\Delta G = N_1 g_v + n g_l + 4\pi R_p^2 \sigma + N_T g_v$$

$$\Delta G = n(g_v - g) + 4\pi R_p^2 \sigma$$

where g_v and g_l are the free energies of single molecules in the vapor and liquid phases, respectively. The number of vapor molecules remaining is: $N_1 = N_T - n$, and $4\pi R_p^2 \sigma$ is the free energy associated with an interface with radius of curvature R_p and surface tension σ. The total number of molecules in the drop, n, and the drop radius, R_p, are related by $n = \dfrac{4\pi R_p^3 \sigma}{3 v_l}$, where v_l is the volume occupied by a molecule in the liquid phase. The equation can be rewritten as:

$$\Delta G = -\frac{4}{3}\pi R_p^3 (g_l - g_v) + 4\pi R_p^2 \sigma$$

where:

$$g_l - g_v = (v_l - v_v) dp \qquad assuming \quad v_v \gg v_l \quad v_v = \frac{kT}{p}$$

$$g_l - g_v = -kT \int_{p_A^o}^{p_A} \frac{dp}{p}$$

$$= -kT \ln \frac{p_A}{p_A^o}$$

with $\dfrac{p_A}{p_A^o}$ the ratio of the vapor pressure of substance A over a flat surface to the actual

equilibrium partial pressure over the liquid, the saturation ratio S. We obtain the Gibbs free energy expression as follows:

$$\Delta G = -\frac{4}{3}\pi R_p^3 \frac{kT}{v_\ell}\ln(S) + 4\pi R_p^2 \sigma$$

This equation gives different outcomes – two curves in Figure 2.4 – that depend on the value of the surface droplet tension, σ, and the saturation ratio, S:

If $S \le 1$, $\Delta G \ge 0$, which is a forbidden process

If $S > 1$, $\Delta G < 0$, which is a spontaneous process
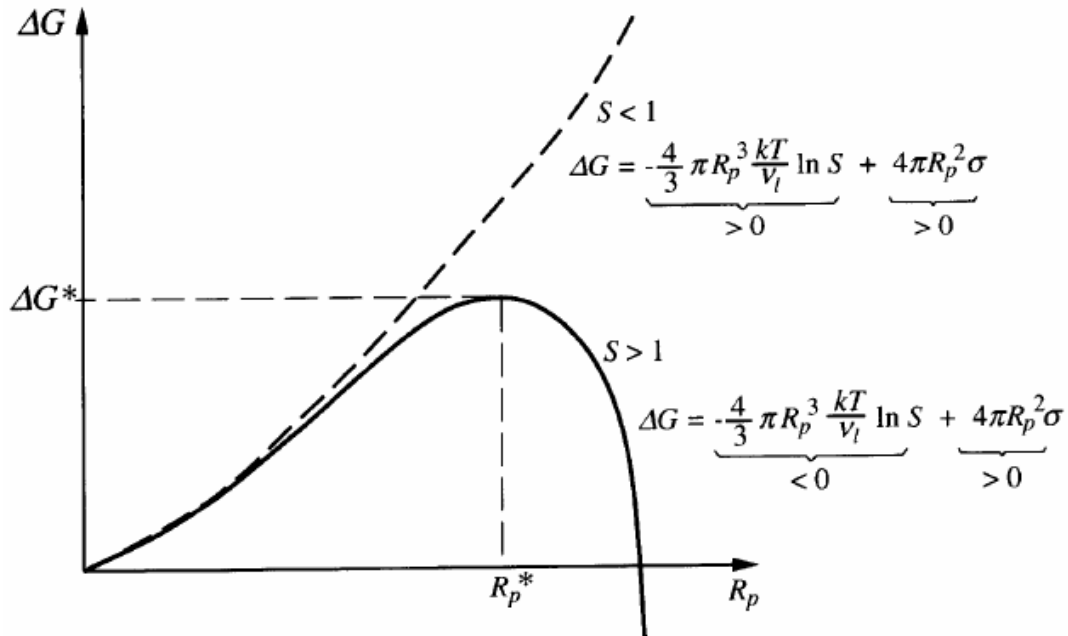
Figure 2.4. Kelvin curve represented by the Gibbs free energy change for formation of a droplet of radius R_p from a vapor with saturation S.

Figure 2.4 shows a sketch of the behavior of ΔG as a function of drop radius, R_p. At small values of R_p, the surface tension term dominates and the behavior of ΔG is similar to the $S < 1$ case. As R_p increases, the first term on the RHS becomes more important so that ΔG reaches a

20

maximum value, ΔG^*, at $R_p = R_p^*$ (Seinfeld et al. 2006).

The free energy barrier height, ΔG^* is a metastable equilibrium, which defines the equilibrium saturation vapor pressure over a drop of a pure liquid, i.e., water. Change of ΔG with radius is negative (<0) only on the right of the critical radius, R_p^*, which is determined by the first derivative of the change in Gibbs free energy, at the metastable equilibrium point ΔG^*:

$$R_p^* = \frac{2\sigma v_\ell}{kT \ln(S)}$$

with: $v_l = \dfrac{M}{\rho_l}$

If $R_p > R_p^*$, when a large enough initial seed particle exists, the drop will grow for a given S.

If $R_p < R_p^*$ for a given S the drop will shrink.

At very high S, R_p^* is small enough that droplets can form randomly. Substituting the solution for R_p^* in the Kelvin equation allows us to obtain ΔG^*:

$$\Delta G^* = \frac{4}{3}\pi R_p^2 \sigma$$
$$= \frac{16\pi}{3} \frac{v_l^2 \sigma^3}{kT \ln S}$$

Increasing the saturation ratio, S, decreases both the free energy barrier and the critical radius. The Kelvin equation is found by solving for the saturation, S:

$$S = \frac{P_{sat}(R_p)}{P_{sat}(\infty)} = e^{\frac{2\sigma M}{kT\rho_l R_p}}$$

2.2.3 Surface Tension

The surface tension, σ, is the free energy per unit surface area of the liquid that allows it to resist an external force. It can be defined as the work per unit area required to extend the surface of the liquid at constant temperature. Surface tension is dependent on temperature. For that reason, when a value is given for the surface tension of an interface, temperature must be explicitly stated. The general trend is that surface tension decreases with the increase of temperature, reaching a value of 0 at the critical temperature.

The surface tension of water is approximately 7.5×10^{-2} N/m for meteorological temperatures (Figure 2.5).
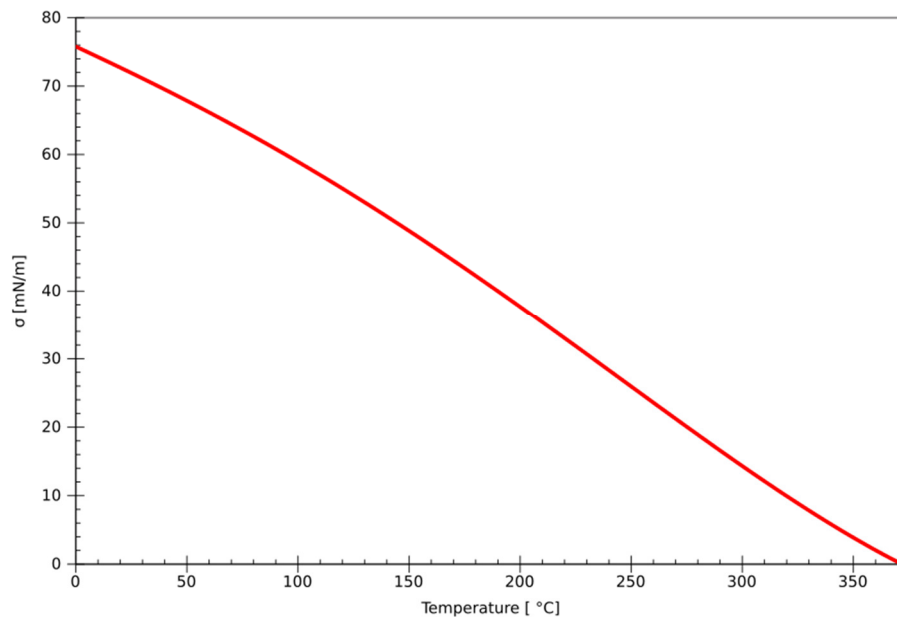
So far, we have looked at homogeneous nucleation, and only pure substances have been included (such as pure water), but since many different types of condensation nuclei are present in the atmosphere, heterogeneous nucleation is far more common, especially in the liquid phase of water. Some condensation nuclei become wetted at relative humidities less than 100% and account for the haze that impedes visibility.

2.2.4 Heterogeneous Nucleation

On Earth, the atmosphere contains significant concentrations of particles of micron and submicron size (aerosols), which have an affinity for water and serve as centers for droplet condensation (Rogers, 1989). These particles are called cloud condensation nuclei, and the process in which water droplets (or other liquid droplets) form on nuclei is what we call heterogeneous nucleation.

Three typical examples of heterogeneous nucleation are described below:

- Nucleation by insoluble sources

- Nucleation by soluble sources

- Nucleation by insoluble + soluble sources.

Although the three aforementioned examples of heterogeneous nucleation are possible on Earth, the most common is soluble source nucleation. On Titan, the atmosphere contains a large amount of tholins – a photochemical byproduct of nitrogen and methane - which are believed to serve as cloud droplet nuclei. Here we will only consider the nucleation by insoluble sources, a special case of the Kelvin effect described by Fletcher (Fletcher, 1958). This process appears to be the one that applies to methane droplets, since it is believed that tholins do not dissolve when in contact with a methane droplet.

23

2.2.4.1 Special case: Insoluble nuclei – Particle Case

The basic theory of nucleation by foreign surfaces for a spherical particle is an extension of the simpler surface case, with a more complicated geometry, shown in Figure 2.6. Consider a small droplet of liquid, with spherical liquid surface radius, r, in contact with a spherical solid surface of radius, R, and with an angle of contact of the liquid on the substrate, θ.
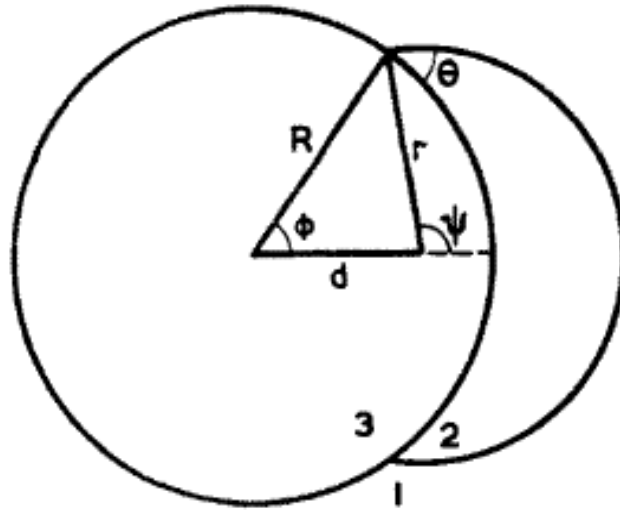
Figure 2.6. Diagram denoting the parent phase by subscript 1, the liquid embryo by 2, and the nucleus by 3 [Fletcher, 1958].

We can find the areas and volume needed to solve the change in Gibbs free energy equation, ΔG, using the contact parameter, m, which is the cosine of the contact angle, θ, between the nucleus and the substrate:

$$m = \cos\theta = \left(\frac{\sigma_{13} - \sigma_{23}}{\sigma_{12}} \right)$$

where σ is the interfacial free energy – or surface tension – between phases, σ_{12} is the surface tension per unit area between liquid and vapor, σ_{13} is the surface tension per unit area between

the substrate and vapor, and σ_{23} is the surface tension per unit area between the substrate and liquid. The free energy of the system is a generalization of the Kelvin equation:

$$\Delta G = n_L \left(g_v - g \right) V_L + \sigma_{12} A_{12} + \left(\sigma_{23} - \sigma_{12} \right) A_{23}$$

If the radius of curvature of the liquid surface is r, then we can express the areas as:

$$A_{LV} = 2\pi r^2 \left(1 - \cos\psi \right)$$

$$A_{CL} = 2\pi R^2 \left(1 - \cos\phi \right)$$

and the volume as:

$$V_L = \frac{\pi r^3}{3} \left(2 - 3\cos\psi + \cos^3\psi \right) - \frac{\pi R^3}{3} \left(2 - 3\cos\phi + \cos^3\phi \right)$$

The size of the critical embryo, r^*, can be determined by setting $\dfrac{\partial \Delta G}{\partial r} = 0$ and solving for the radius:

$$r^* = \frac{2\sigma_{12}}{n_L kT \ln(\dfrac{p}{p_\infty})} = \frac{2\sigma_{12}}{n_L kT \ln(S)}$$

This is the same result we found for the Kelvin equation (in a slightly different form) for homogeneous nucleation, but this is to be expected, since the curved surface of the critical embryo must be in equilibrium with the vapor.

Substituting the solutions for the areas, volume and critical embryo radius into the change

25

in Gibbs free energy, we obtain:

$$\Delta G^* = \frac{16\pi\sigma_{12}^3}{3(n_L kT \ln S)^2} f(m)$$

where $f(m)$ is a third degree polynomial solved in Fletcher, 1958. This result differs from the

homogeneous case by the factor $f(m)$. Since $-1 \le m \le 1$, $0 \le f(m) \le 1$, so foreign surfaces have the

general property of reducing the free energy necessary to form a critical embryo. With these

results we can set a relationship between the saturation and the radius of the embryo (Figure 2.7).

For water at T=273 K, we have:
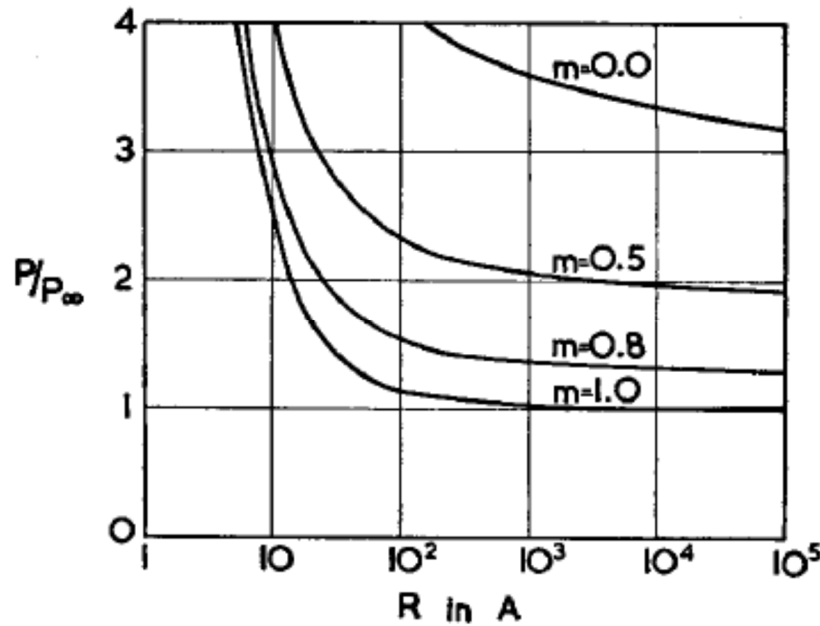
Figure 2.7. Supersaturation S=P/P$_{inf}$ at which condensation occurs on a spherical particle of radius R, at T=0°C (273 K) and m=$\cos\theta$. (Fletcher, 1958), on Earth.

2.3 Cloud Microphysics for Methane Droplets on Titan

Cloud microphysics involves the processes that lead to the formation of individual cloud and precipitation particles (droplets) (Pruppacher, 1978), and it is concerned with the liquid and solid particles that constitute clouds (Lamb et al., 2011). Atmospheric thermodynamics is crucial for the understanding of dynamic processes, cloud formation and precipitation and therefore it is a logical first consideration in the analysis of the "air" on Titan.

2.3.1 Thermodynamics of Titan's air

Air, as we know it on Earth, is a mixture of several so-called permanent gases and different solid and liquid particles of variable concentrations (Rogers, 1989). The approach in meteorology is to treat air as a mixture of two ideal gases: "dry air" and water vapor (moist air), and for the case of Titan, this ideal gas mixture is of nitrogen and methane.

- The Ideal Gas Law

Starting with the equation of state for an ideal gas:

$$pV = nRT$$

or with specific quantities:

$$p\alpha = \frac{n}{m}RT \quad or \quad p\alpha = \frac{R}{M}T \quad with \quad n = \frac{m}{M}$$

we can determine the gas constant for Titan's dry air, R^*.

The bulk of Titan's atmosphere is made up of nitrogen (~95%). So, it is possible to assume that the dry component of Titan's air is solely N_2. We use the molecular weight of nitrogen, M_{N2} to find R^*:

$$R^* = \frac{R}{M_{N2}}$$

where R is the universal gas constant:

$$R^* = \frac{8.314 \frac{J}{mol\ K}}{28 \frac{g}{mol}} = 296.9 \frac{J}{kg \cdot K}$$

this result is similar to Earth's air gas constant $R^*_{air-earth} = 287 \frac{J}{kg\ K}$

On Earth, we have a dry air component and a water vapor component, and when we are interested in the buoyancy of an air parcel we do a correction for the presence of the vapor, the virtual temperature correction. We do this to deal with a single gas constant of the dry air and we correct the temperature, T, with the virtual temperature, T_v.

Now, the equation of state can be written in terms of the dry air gas constant and the virtual temperature:

$$p = \rho R_d T_v$$

Using this solution, we calculate Titan's atmospheric density, assuming that the virtual

temperature is roughly 94 K (based on Titan's surface temperature), as follows:

$$\rho = \frac{p}{R_d T_v} = \frac{1.5 \times 10^5 \, Pa}{296.9 \dfrac{J}{kg \cdot K} \times 94K} = 5.37 \frac{kg}{m^3}$$

$$\rho_{atm} = 5.37 \frac{kg}{m^3}$$

This result is roughly 5 times higher than the density of dry air on Earth, which at standard

temperature and pressure is, $\rho_{air-earth} = 1.225 \frac{kg}{m^3}$

- Hydrostatic Balance

Solving for the whole atmospheric structure requires the assumption of an atmosphere in

hydrostatic equilibrium:

$$\frac{\partial p}{\partial z} = -\rho g = -\frac{P}{RT} g$$

$$\frac{1}{p}\frac{\partial p}{\partial z} = -\frac{g}{RT}$$

This solution gives the scale height, *H*, which is the distance over which the atmospheric pressure

of Titan decreases by a factor of e (e-folding distance),

$$\frac{g}{RT} = \frac{1}{H}$$

we solve for it by integrating:

$$\int_0^z \frac{1}{p} \partial p = -\frac{g}{R} \int_0^z \frac{1}{T} \partial z$$

$$\ln\left(\frac{p(z)}{p_s}\right) = -\frac{g}{RT^*}\int_0^z \frac{T^*}{T}\partial z$$

$$p(z) = p_s \exp\left[\frac{\int_0^z \frac{T^*}{T}\partial z}{H}\right]$$

$$with \quad T^* = 90K \quad and \quad g = 1.35\frac{m}{s^2} \quad \Rightarrow \quad H = 19.1\,km$$

On Earth, the scale height is roughly 7 km.

- First Law of Thermodynamics and Dry Adiabatic Lapse Rate

Titan's atmosphere is roughly 600 km deep, however, the troposphere is only about 40 km deep, the temperature decreases with height (as seen in figure 1.2.5), and the atmosphere tends to be optically thick. With the first law of thermodynamics, we solve and calculate the dry adiabatic lapse rate for the troposphere as follows:

$$dq = du + dw = c_v dT + pd\alpha$$

$$dq = c_v dT + d\left(\frac{p}{\rho}\right) + \alpha dp = c_v dT + RdT + \alpha dp$$

$$dq = c_p dT - \alpha dp$$

where $\alpha dp = \dfrac{d\rho}{dp}$

$$dq = c_p dT + RdT - \alpha dp = c_p dT + gdz$$

For the adiabatic case:

$$dq = 0 \quad \Rightarrow \quad -\frac{dT}{dz} = \frac{g}{c_p} = \Gamma$$

$$\Gamma = \frac{1.354 \times m/s^2}{1.9\,\dfrac{kJ}{kg\,K}} \approx 0.7\,K/km$$

$$\Gamma \approx 0.7\,K/km$$

This result can be seen in the first 40 km of the temperature vertical profile plot from Huygens descent measurements, and it is considerably smaller than the one on Earth, where the dry adiabatic lapse rate, $\Gamma_{earth\text{-}dry}$ = *9.8 K/km*.

2.3.2 Kelvin Equation for Methane Droplets

Starting with pure methane we will find, like for water, that droplets will need to be formed by heterogeneous nucleation for the liquid phase. However, we take a look at the development of the Kelvin theory and see where we can go with it.

The Kelvin equation is found by solving for the saturation:

$$S = \frac{P_{sat}(R_p)}{P_{sat}(\infty)} = e^{\frac{2\sigma M}{kT\rho_l R_p}}$$

31

$$\Delta G = -\frac{4}{3}\pi R_p^3 \frac{kT}{v_\ell}\ln(S) + 4\pi R_p^2 \sigma$$

$$R_p^* = \frac{2\sigma v_\ell}{kT\ln(S)} \quad with \quad v_l = \frac{M}{\rho_l}$$

We solve the above equation for methane droplets:

$$v_l = \frac{M}{\rho_l} = \frac{16\dfrac{g}{mol}}{6.02\times10^{23}\dfrac{molecules}{mol}} = 5.9\times10^{-29}\,m^3$$

with ρ_d = 450 kg / m^3, σ_d = 16.4 mN / m, k = 1.38x10^{-23} J / K , and T = 94 K . And assuming a

radius of a small monomer collection to be $R_p^* \approx 10^{-9}m$, we use a back of the envelope calculation,

to approximate a value for the supersaturation:

$$S = e^{\frac{2\sigma v_\ell}{R_p kT}} \approx 4.5 \quad (450\%\ \text{relative humidity!})$$

We confirm that homogeneous nucleation of methane droplets is most likely not found in Titan's atmosphere and, like for water on Earth, droplets will need to be formed by heterogeneous nucleation for the liquid phase.

2.4 Finding the Sizes of Methane Cloud Droplets and When They Precipitate Out of the Cloud

2.4.1 Terminal Velocity of a Methane Droplet

The settling behavior of a cloud particle depends on how it interacts with the air in its immediate environment. As the particle falls, it gains speed, it pushes air out of the way and it experiences air resistance, or drag force. Once the drop is big enough and reaches terminal velocity, it falls at a constant speed, v_{ter}. It is all due to a balance between gravitational forces pulling the drop down and a drag force lifting it.

The terminal velocity calculation involves the balance between gravity and the viscous (or drag) force (ignoring buoyancy forces):

$$F_g = F_D$$

The gravitational force on the cloud droplet is defined as:

$$F_g = m_d g_{Titan} = \rho_d V_d g_{Titan}$$

The drag force on the droplet is proportional to the dynamic pressure, $p_{dyn} = \frac{1}{2}\rho_{air}v_{fall}^2$, the cross-sectional area of the particle, A_p, and the drag coefficient, C_D, so we can write:

$$F_D = \frac{1}{2}\rho_{air}v_{fall}^2 A_d C_D$$

The proportionality constant, C_D (the drag coefficient), is an empirical factor that accounts for all non-geometrical components to the drag force.

Balancing the forces:

33

$$\rho_d V_d g_{Titan} = \frac{1}{2} \rho_{air} v_{fall}^2 A_d C_D$$

with, $v_{fall} = v_{ter}$. Solving for the terminal velocity:

$$v_{ter} = \left(\frac{2 g_{Titan}}{C_D} \frac{\rho_d}{\rho_{air}} \frac{V_d}{A_d} \right)^{1/2}$$

The fall speed, or terminal velocity, v_{ter}, ultimately depends on the ratio of particle mass (as $\rho_p V_p$) to the effective cross-sectional area, $A_p C_D$. The generic calculation of fall speeds can be made specific to cloud drops assuming a sphere of diameter, D_p, which gives the volume and cross sectional area of the particle as:

$$V_d = \frac{\pi}{6} D_d^3 \qquad and \qquad A_d = \frac{\pi}{4} D_d^2$$

giving a volume-to-area ratio:

$$\frac{V_d}{A_d} = \frac{2}{3} D_d$$

The air flow around the drop is described by the Navier-Stokes equation of motion, and when the different terms of it are compared with one another, the flow is characterized by the dimensionless Reynolds number, which is the ratio of the inertial to the viscous forces:

$$N_{Re} = D_d \frac{V_d}{v_{air}}$$

where v_{air} is the air kinematic viscosity, defined as:

$$v_{air} = \frac{\mu_{air}}{\rho_{air}}$$

and μ_{air} is the dynamic viscosity of air.

Plugging these results to the drag force equation, we obtain:

$$F_D = 3\pi\mu_{air}v_{ter}D_d\left(\frac{C_D N_{Re}}{24}\right)$$

Raindrops do not reach high Reynolds numbers, since they break up before that happens, and for low Reynolds numbers (N_{Re}<1), the viscous effects dominate and the expression above reduces to Stokes' Law, where:

$$C_D = \left(\frac{24}{N_{Re}}\right)$$

Therefore:

$$F_D = 3\pi\mu_{air}v_{ter}D_d$$

This works as long as we assume that the droplets are not very small - sub-micron - and that they remain spherical while falling. We can now solve for the terminal velocity from the force balance mentioned before:

$$F_g = F_D$$

$$\rho_d V_d g_{Titan} = 3\pi\mu_{air}v_{ter}D_d$$

$$\frac{4}{3}\pi R_d^3\rho_d\, g_{Titan} = 3\pi\mu_{air}v_{ter}D_d$$

$$\frac{\pi}{6}D_d^3\rho_d\, g_{Titan} = 3\pi\mu_{air}v_{ter}D_d$$

$$v_{ter} = \frac{\rho_d \, g_{Titan} D_d^2}{18\mu_{air}}$$

From this solution of the terminal velocity, it is possible to determine a range of diameters of methane cloud droplets:

$$D_p = \left(\frac{18\mu_{air} v_{ter}}{\rho_d \, g_{Titan}} \right)^{1/2}$$

To find limits on droplet sizes, we need to find vertical velocities from observations and calculations that allow us to substitute as the terminal velocity. The two cases we present here are based on the vertical component of atmospheric flow of Titan as measured by HASI, and the calculation of CAPE done by Griffith et al., 2008.

2.4.2 Case 1: The Vertical Component of the Flow from Huygens descent data

From the solution of the terminal velocity and the vertical component of the flow from the Huygens descent trajectory data (Figure 1.4), it is possible to determine a range for diameters of methane cloud droplets by setting $v_{ver-flow} = v_{ter}$

The vertical velocities in the first 40 km of altitude range from -0.05-0.1 m/s, are obtained from Figure 1.4. We show a zoomed-in version in Figure 2.8 indicating the velocity range values.
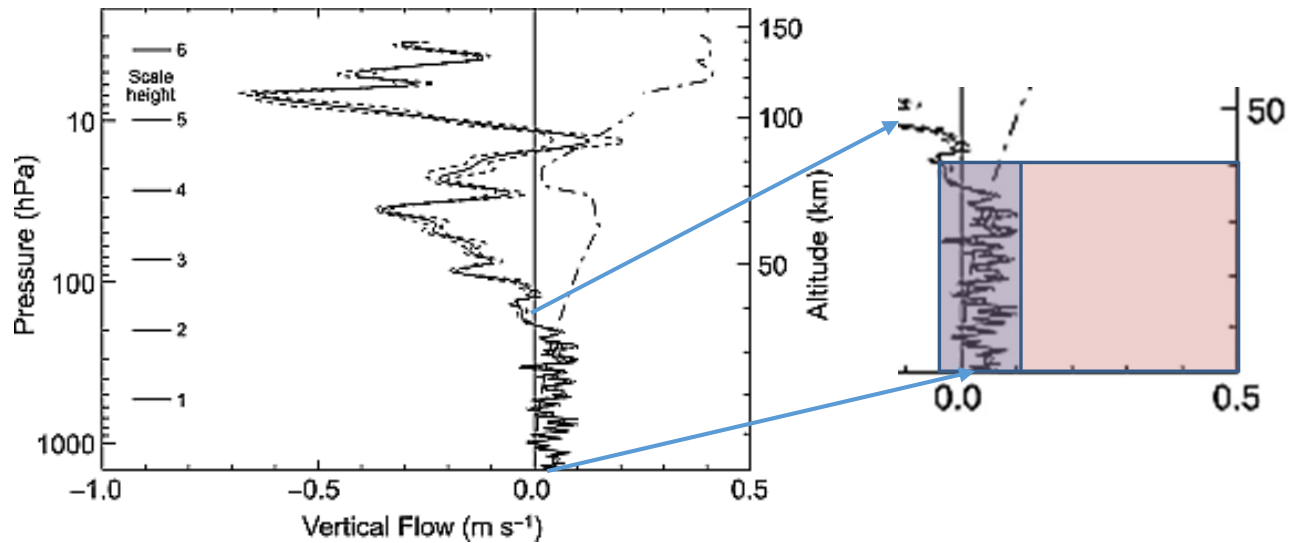
Figure 2.8. Zoom-in of Figure 1.4 showing the vertical component of the atmospheric flow on Titan along the descent trajectory of the Huygens probe derived from radio telemetry [Bird et al., 2005].

Setting the constant values for g_{Titan} = 1.352 m/s² and ρ_d = 450 kg/m³ , while the values of the viscosity of air are set dependent on height as follows:

$$\mu_{air} = 6.25\text{x}10^{-6} \text{ kg/m-s @ Z= 0 km and T =94 K,}$$

$$\mu_{air} = 5.27\text{x}10^{-6} \text{ kg/m-s @ Z= 15 km and T=80 K ,}$$

$$\mu_{air} = 4.69\text{x}10^{-6} \text{ kg/m-s @ Z= 40 km and T =72 K.}$$

We plot the vertical flow speeds at the three altitudes, Z=0, 15 and 40 km to find drop diameters at different altitudes (Figure 2.9) and obtain a range of diameters sufficiently large that suggest the droplets could hold small condensation nuclei.
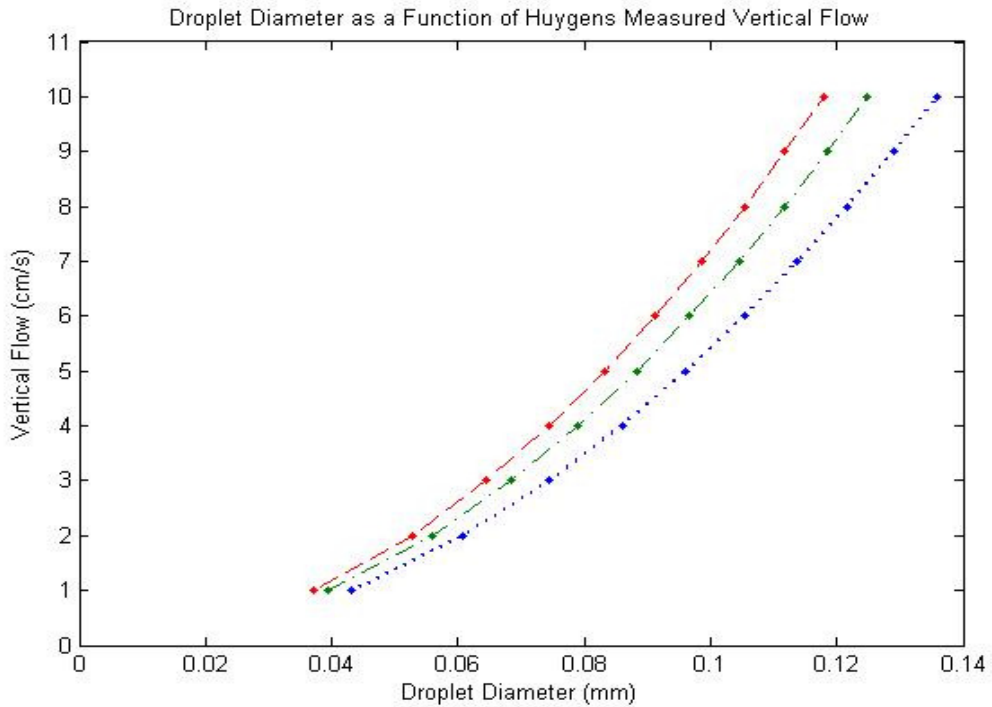
Figure 2.9. Calculated droplet diameters as a function of the vertical component of measured flow from Huygens at: Z=0 km (blue dots); Z=15 km (green dots); and Z=40 km (red dots).

2.4.3 Case 2: The Convective Available Potential Energy – CAPE

If the air parcel is saturated, the relevant lapse rate to compare the environment lapse rate to is the saturated adiabatic lapse rate, $\Gamma_s < \Gamma_d$. There exists the possibility that the environmental lapse rate, Γ, will lie between the dry and saturated values, $\Gamma_s < \Gamma < \Gamma_d$. Then, if a subsaturated parcel is lifted from its equilibrium level (EL), it will initially follow the dry adiabat to the LCL, then a saturated adiabat from there (as shown in the figure below). The parcel's temperature will exceed the environmental temperature at the level of free convection (LFC). We have had to do work on the parcel to get it to the LFC, but once there the parcel will continue to rise of its own buoyancy. This situation is referred to as *conditional instability*. If lifted above its LFC, the parcel will continue to rise until its temperature again equals the environmental temperature. At this point, all forces balance on the parcel, and we refer to this point as another EL.

Deep convection requires a conditionally unstable lapse rate ($\Gamma s < \Gamma < \Gamma d$), a substantial moisture boundary layer, and lifting near the surface. Conditional instability allows potential energy to be built up at high altitudes, as positive buoyancy. The measure of the available potential energy, or CAPE, is defined as the integral of the buoyancy force per unit mass on a parcel from the LFC to the EL:

$$CAPE \equiv \int_{LFC}^{EL} \frac{F}{m'} dz$$

Where, $\dfrac{F}{m'} = g \dfrac{\rho - \rho'}{\rho'} = g \dfrac{\alpha - \alpha'}{\alpha'}$, with α, the specific volume (primed quantities refer to the parcel, and unprimed to the environment).

Applying the ideal gas law and hydrostatic equilibrium to the CAPE equation, we obtain:

$$CAPE \equiv \int_{LFC}^{EL} (\alpha - \alpha') dp = R_d \int_{EL}^{LFC} (T' - T) d \ln p$$

We can diagnose CAPE by plotting the environmental temperature T and the temperature path a lifted parcel would take to T′ on a skew T-ln(p) diagram, and search for areas with T′ > T. Assuming all the potential energy is efficiently converted into kinetic energy, we equate CAPE, the convective potential energy per unit mass, with the mass specific total potential and kinetic energies, as follows:

$$CAPE \equiv \frac{PE}{unit\ mass} = \frac{KE}{unit\ mass} = \frac{1}{2} w^2$$

where w is the vertical velocity of the falling droplets, which we assume to be equal to the

terminal velocity. Titan's CAPE has been calculated in many studies by Tokano et al. (2006), Barth & Rafkin (2007), and Griffith et al. (2008), among others. The results vary from 60 J/kg to 960 J/kg. This wide range of values is considered in our calculations to find the droplet diameters as presented in Figure 2.9 for the same heights as in Figure 2.10.
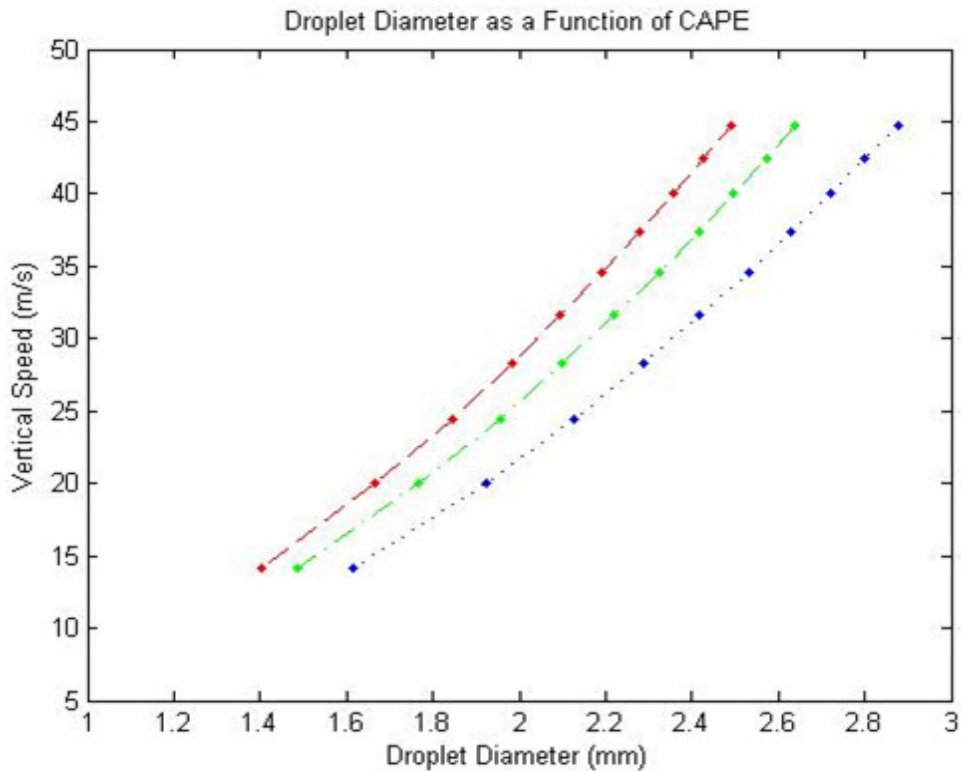
In summary, Titan's cloud droplet formation occurs under heterogeneous nucleation by insoluble particle sources serving as cloud condensation nuclei (CCN) . The droplet diameters found with the two different methods give us results that lie in the range 0.04–0.14 mm for Case 1, and from 1.40–2.9 mm for Case 2, while a typical tholin size range is ~0.04-0.1 microns, suggesting that tholins are good candidates for CCN.

CHAPTER 3

Cloud Data Survey and Image Processing

3.1 Introduction

The purpose of this chapter is to show the process of the work done to find clouds in the data and selecting the storms to study as well as detailing the steps of the image reduction and processing as well as the techniques to enhance cloud features in the resultant images that allowed us to create plots and analyze the evolution of cloud events. We take one step further and briefly introduce the general circulation model that will later be utilized to compare the observational analysis results with model simulations and confirm our findings.

3.2 Cassini Observations of Titan with ISS (2004-2017)

Cloud formation on Titan has been observed for decades but only studied in detail when the Cassini-Huygens space probe arrived at the Saturn system. For over 13 years, Cassini exposed surface and cloud features over Titan's globe, never seen before due to the moon's thick atmosphere.

To constrain Titan's cloud morphology and dynamics, we first documented cloud events by surveying images as they became available, from the 126 Cassini Titan flybys during the 2004 to 2017 mission, to search for cloud phenomena and identify various types of storms. Images were retrieved from the NASA Planetary Data System (PDS) Image Atlas site.

We surveyed thousands of images from the Imaging Science Subsystem (ISS) instrument

cameras in search of clouds. It is likely that Cassini did not catch every single cloud formed through the duration of the mission, but dozens of examples were recorded. Although only two cloud events had a large number of images to allow for the study of the evolution of each storm, or the spatial-time distribution of the clouds, a handful of examples were hand-picked for further analysis in chapter 5 of this dissertation.

3.2.1 ISS Camera Filters and Titan Clouds

The Imaging Science Subsystem (ISS) instrument onboard Cassini was the highest-resolution two-dimensional imaging device on the orbiter and was designed for investigations of the bodies and phenomena found in the Saturnian planetary system (Porco et al., 2004). It consisted of two separate cameras, as shown in Figure 3.1, that produced images 1024 x 1024 pixels in size: one wide angle camera (WAC) and one narrow angle camera (NAC) for higher resolution. Each of these cameras were equipped with a pair of optical filter wheels spanning wavelengths from the ultraviolet to the near-infrared (see Table 3.1 for the detailed list of filters).
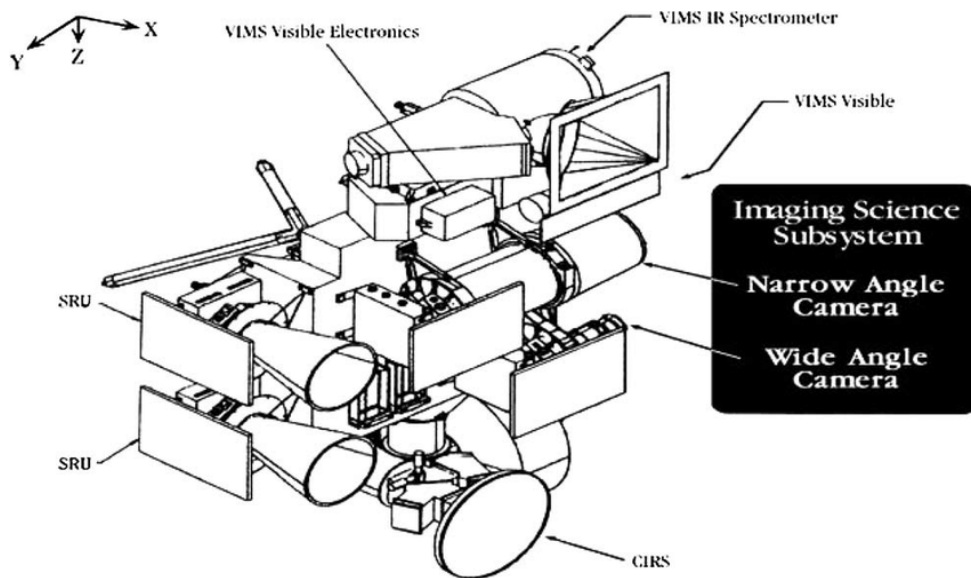
Figure 3.1. Diagram of Cassini cameras, including the ISS WAC & NAC. [Porco et al., 2004]

Color		Wavelength*	Purpose
UV1	ultraviolet	258 nm, wide	atmospheric aerosols
UV2	ultraviolet	298 nm, wide	aerosols, broadband color
UV3	ultraviolet	338 nm, wide	aerosols, broadband color, polarization
BL2	blue	440 nm, medium	medium-band color, polarization
BL1	blue	451 nm, wide	broadband color
GRN	green	568 nm, wide	broadband color
MT1	visible	619 nm, narrow	weak methane band, vertical sounding
CB1b	near infrared	603 nm, narrow	continuum band for MT1
CB1a		635 nm, narrow	
RED	red	650 nm, wide	broadband color
HAL	hydrogen alpha	656 nm, narrow	hydrogen alpha / lightning
MT2	near infrared	727 nm, narrow	medium methane band, vertical sounding
CB2	near infrared	750 nm, narrow	continuum band for MT2
IR1	near infrared	752 nm, wide	broadband color
IR2	near infrared	862 nm, wide	broadband color; ring absorption band
MT3	near infrared	889 nm, narrow	strong methane band, vertical sounding
CB3	near infrared	938 nm, narrow	continuum band for MT3; see through Titan haze
IR3	near infrared	930 nm, wide	broadband color
IR4	near infrared	1002 nm, long-pass	broadband color
CL1	all colors, ultraviolet to near infrared	611 nm, wide open	filter wheel 1 clear (combine with wheel 2 filters)
CL2	all colors, ultraviolet to near infrared	611 nm, wide open	filter wheel 2 clear (combine with wheel 1 filters)
P0	visible polarization, 0°	617 nm	visible polarization, 0°
P60	visible polarization, 60°	617 nm	visible polarization, 60°
P120	visible polarization, 120°	617 nm	visible polarization, 120°
IRP0	IR polarization, 0°	746 nm	IR polarization, 0°; see through Titan haze

Table 3.1. ISS instrument filter list. Both cameras had two filter wheels, 23 different filters for the NAC and 17 for the WAC. The two filter wheels could be moved independently, allowing filters on different wheels to be stacked. The main filters used for this study are highlighted in blue.

Materials with different compositions preferentially absorb different wavelengths of light, therefore observations made at different wavelengths can produce vertical maps of Titan's

atmosphere at different heights. For example, a filter combination that blocks all but certain infrared wavelengths produces images that peer through Titan's thick haze and yield a view of the moon's surface and low-altitude clouds. The main filters used for this research study are highlighted in blue in table 3.1.

3.2.2 CB3 / MT1 Filter Combination

A particular set of ISS camera filter combinations were used to investigate specific aspects of Titan's atmosphere associated with clouds. As seen in Figure 1.9 (in Chapter 1) and Figure 3.2 (below), each image was taken with a pair of optical filter wheels that highlighted features seen at different altitudes. Titan's clouds are best seen with the 938-nm near infrared images because they are located low in the atmosphere, while the 619-nm visible images are best for viewing the haze layer above the clouds.
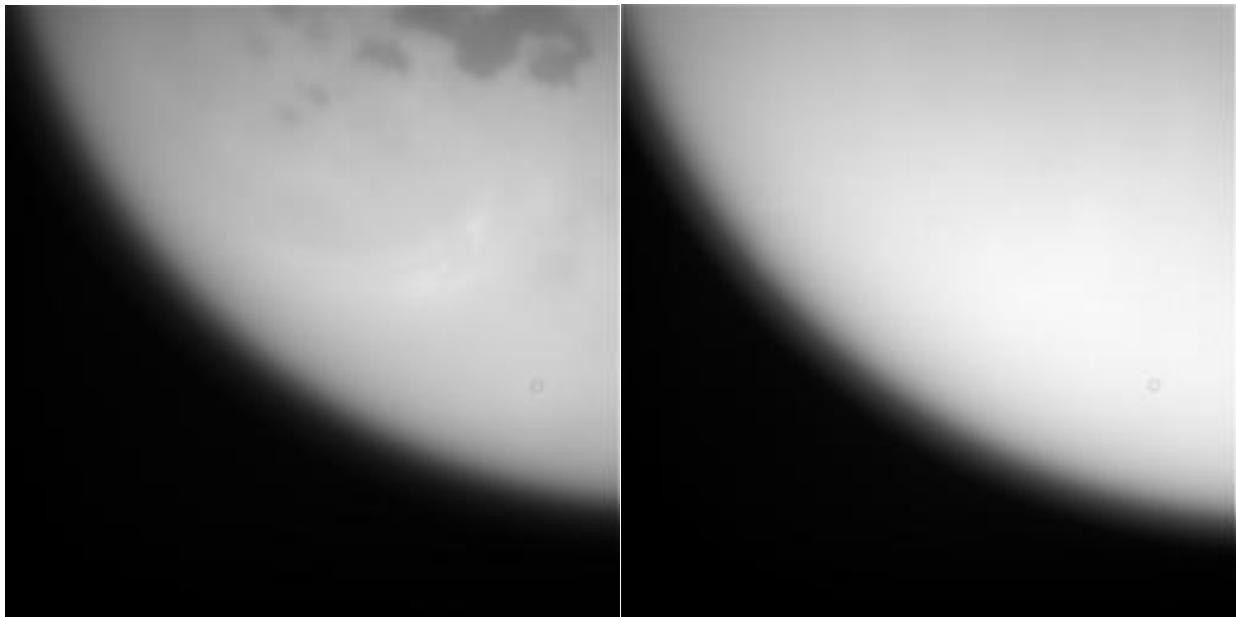
Figure 3.2. Titan seen from the Cassini spacecraft on August 12, 2017 – Left Image: CL1/CB3 filter combination. Right Image: CL1/MT1 filter combination. Images were taken 1 minute apart.

The main two-filter combinations we selected to process and analyze cloud images are:

1) CL1/CB3 - visible 611 nm, wide open filter wheel clear /near-infrared 938 nm, narrow continuum band to see through Titan haze and,

2) CL1/MT1 - visible 611 nm, wide open filter wheel clear /visible 619 nm, narrow weak methane band, vertical sounding. This second set is the one used for haze removal after the images are processed.

3.2.3 Other Filter Combinations

Some wavelengths of light penetrate farther into the atmosphere than others, and we found that some of the prominent cloud images seen in the CL1/CB3 filter combination also had image
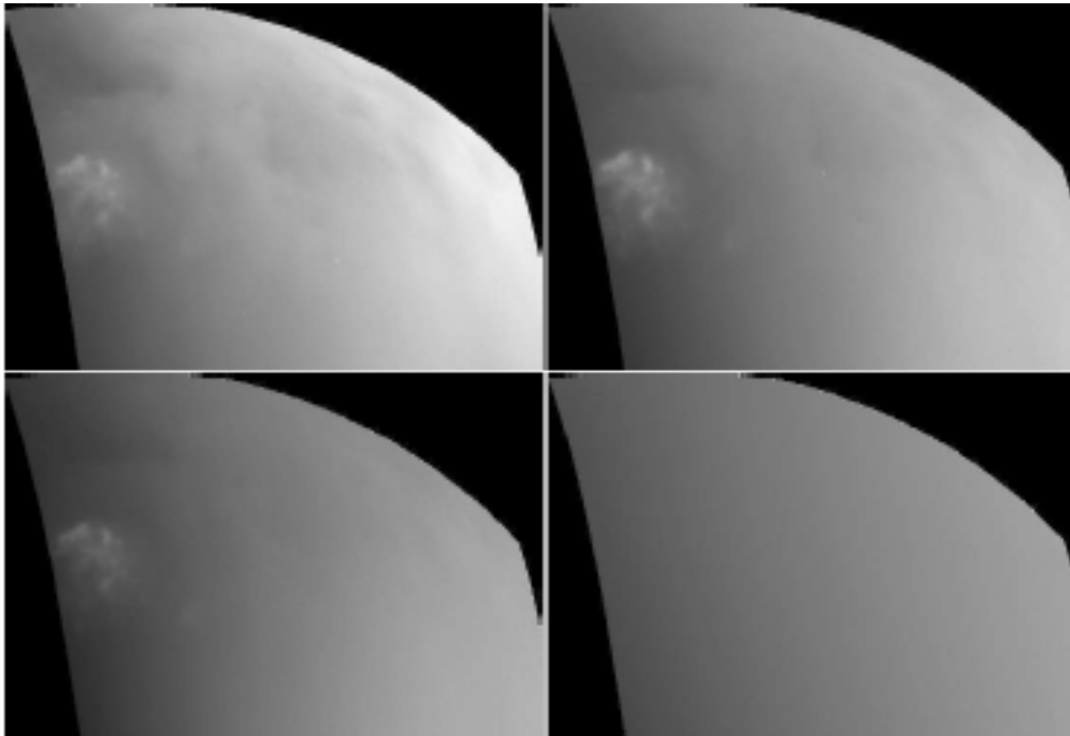
Figure 3.3. Titan seen from the Cassini–Huygens spacecraft on July 07, 2004 – Left Top Image: CL1/CB3 filter combination. Right Top Image: IRP0/IR3 filter combination. Left bottom Image: CL1/IR3 filter combination. Right Bottom Image: CL1/UV3 filter combination. Images taken a few minutes apart.

counterparts in other filter combinations. In some instances, the clouds appear faintly, but in others can be as bright as or brighter than the ones found with the main 611 nm/938 nm wavelength set. Figure 3.3 is an example of images taken only a few minutes apart on 2004-07-02, with the following filter combinations: CL1/CB3, IRP0/IR3, CL1/IR3 and CL1/UV3, where the clouds can be seen in three out of the 4 images.

Some of the clouds found with these "other filter" combinations helped us record the length of time the clouds were seen during a particular storm and were used to estimate the duration of it.

3.3 ISS Cloud Survey

Sifting through thousands of ISS images allowed us to build a catalogue of cloud events that were found mainly with the CL1/CB3 filter combination. Table 3.1.2 shows a sample of the clouds found in the data during our survey. Only one image is shown per cloud event. A much larger set, containing all found cloud events and their respective subset of images, will be available to view once uploaded to our research group website: https://dept.atmos.ucla.edu/jonmitch
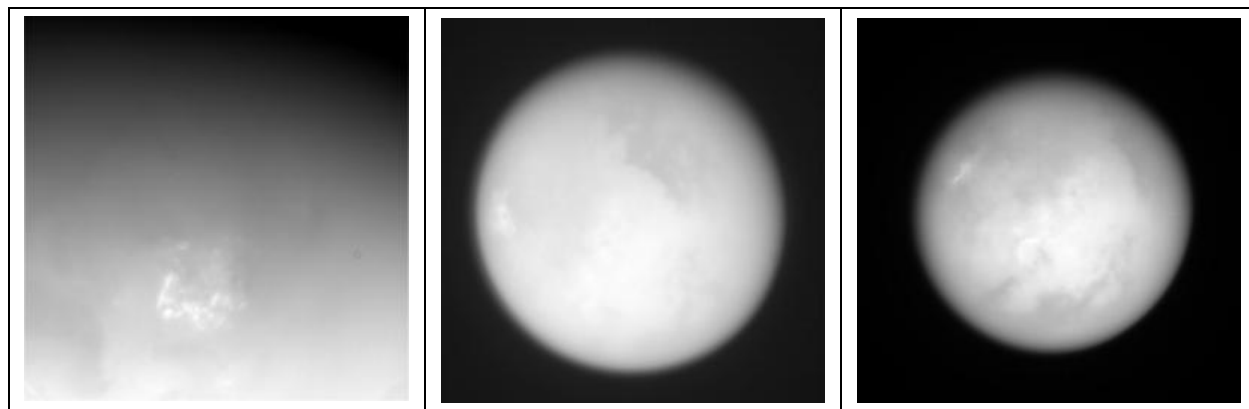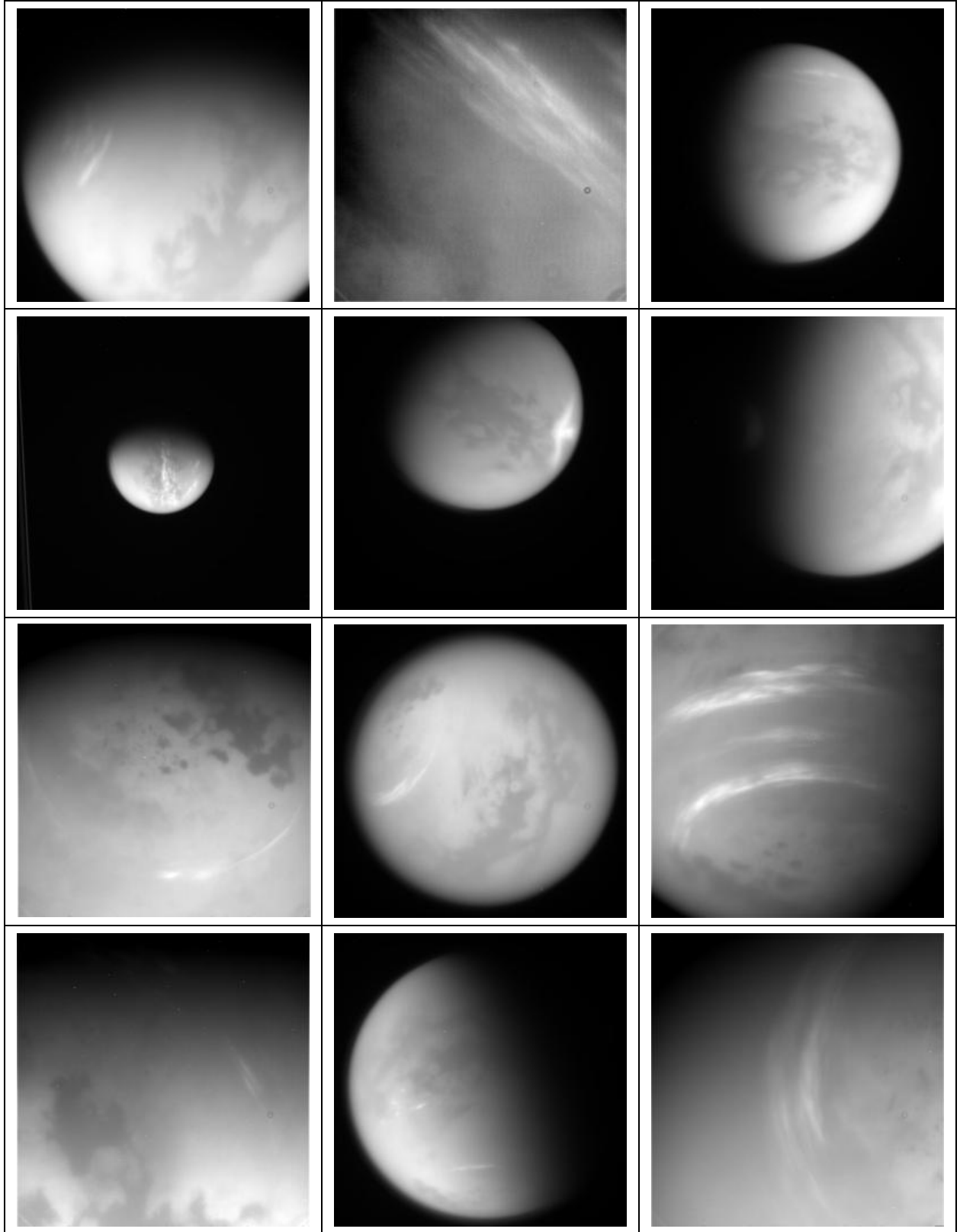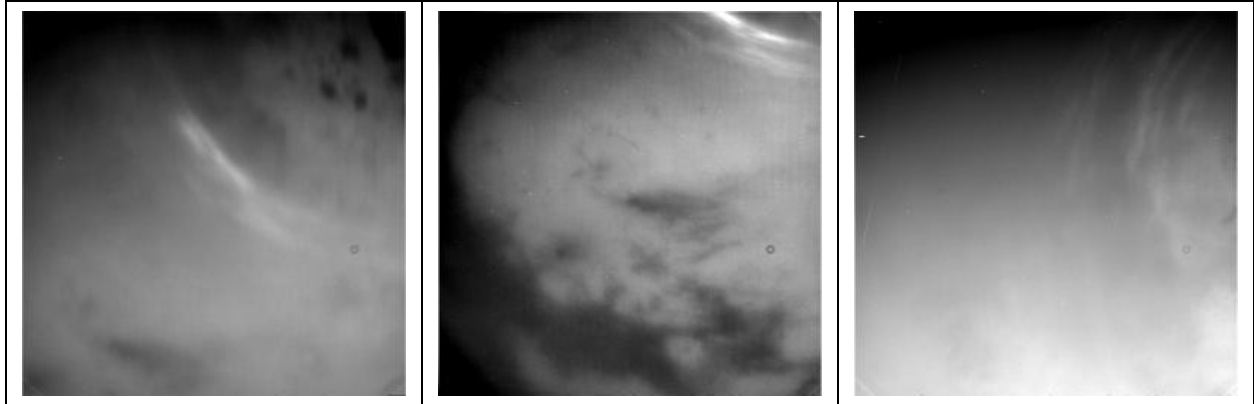
Table 3.2. Titan seen with the Cassini ISS cameras: A sample of clouds (one image per event) found in the data from 2004-2017, as observed with the CL1/CB3 filter combination. Table starts in page 46 and continues through pages 47 and 48.

3.4 Cloud Image Processing

This process includes photometry and mapping, using the ISIS 3 Integrated Software for Imagers & Spectrometers package developed by the U.S. Geological Survey/Astrogeology Research Program site for NASA. ISIS 3 combines basic capabilities of image processing and display of 2 – and 3-dimentional data with the specialized planetary cartographic functionality for planetary science applications (https://isis.astrogeology.usgs.gov/).

3.4.1 Image Reduction

The ISIS 3 digital processing software package combines elements of classical image processing with new techniques developed specifically for the analysis of image cubes.

To start the process, ISIS 3 expects PDS raw Experiment Data Record (EDR) images that have not been radiometrically calibrated and contain the mission-specific label keyword information required for cartographic processing. The PDS ISS EDR data is obtained in two files, a detached PDS label file (img_number.LBL) and the image data file (img_number.IMG).

Three out of four ISIS 3 steps to process ISS images are listed in detail in this section while the last step will be described in section 3.3.2.

STEP 1: This first step of image reduction requires the data to be converted to ISIS with the appropriate application that correctly imports the required mission specific keywords. The application is called "ciss2isis", a program that imports the PDS ISS image file into an ISIS image cube.

STEP 2: During the second step, the application "spiceinit" adds the appropriate Spacecraft and Planetary ephemeredes, Instrument C-matrix and Event kernels (SPICE) information to the ISIS image cube. Once spiceinit has been successfully applied to a raw ISIS image cube an abundance of information can be computed and retrieved for geometry and photometry and further processing.

STEP 3: The third step, before mapping, is to run the "cisscal" ISIS 3 application. cisscal applies the Cassini ISS radiometric calibration correction.

Occasionally a pixel noise removal substep is added to this third step when an amount of random noise remains in the ISS image after the calibration correction is done. This substep is done using the "noisefilter" ISIS 3 application.

The last step of the image reduction is the image mapping. The details of this step and its results are given in the next section.

3.4.2 Cloud Mapping (last reduction step)

After all selected images from one event are fully processed through the ISIS3 steps, detailed in section 3.3.1, one last step converts the reduced images into maps that will be used for data

analysis.

STEP 4: The main application for this last step is "cam2map", which converts a raw cube to a map projected image. The default transformation is based on the original viewing geometry of the observation, relative position of the target body and the definition of the output map projection. ISIS 3 supports a long list of possible map projections, and its current default is "Sinusoidal". Although cam2map will automatically compute defaults for most of the mapping parameters a template file is generally needed to adjust or define a subset of the parameters, including a different map projection.

Typically, a list of parameters that include central latitude and longitude as well as a specific map projection is added to the map template file, selected to best fit the work that will be done with the resultant mapped image(s) and for continuity when a set of several images are processed together to analyze one cloud event. The images in Figure 3.4 show both the raw image as obtained by ISS on the left and the resultant map projected image after the four ISIS 3 steps have been applied, on the right.
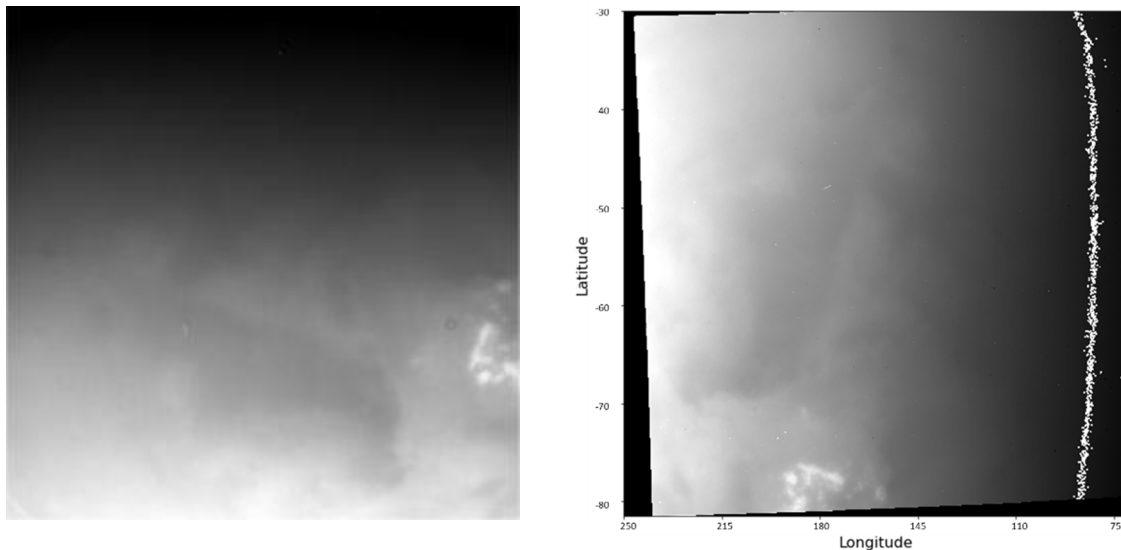
Figure 3.4. Titan clouds seen July 7, 2004. Left: ISS CL1/CB3 raw image (unprocessed). Right: Same image after ISIS 3 process, shows latitude, longitude, in a simple cylindrical map projection.

3.5 Data Processing & Cookbook

3.5.1 Haze Removal

Haze Removal allows for an enhanced view of the clouds against the background. We use primarily a combination of CL1, CB3 and CL1, MT1 filters (as in Turtle et al., 2011) to enhance the cloud features. For any given footprint a set of images that includes at least two or three CB3 images and one MT1 are acquired around the same time. The CB3 mapped images are stacked and corrected for shifts, using iPython – a web-based environment for coding and plotting - and the MT1 filter image is used for the photometric correction to eliminate the haze (results shown in Figure 3.5). The resultant enhanced images are stacked and aligned again to make plots as described in the next section. Additionally, when a sequence of images is found, we can produce movies to show the propagation of the clouds, which was done for the event presented in Chapter 4.
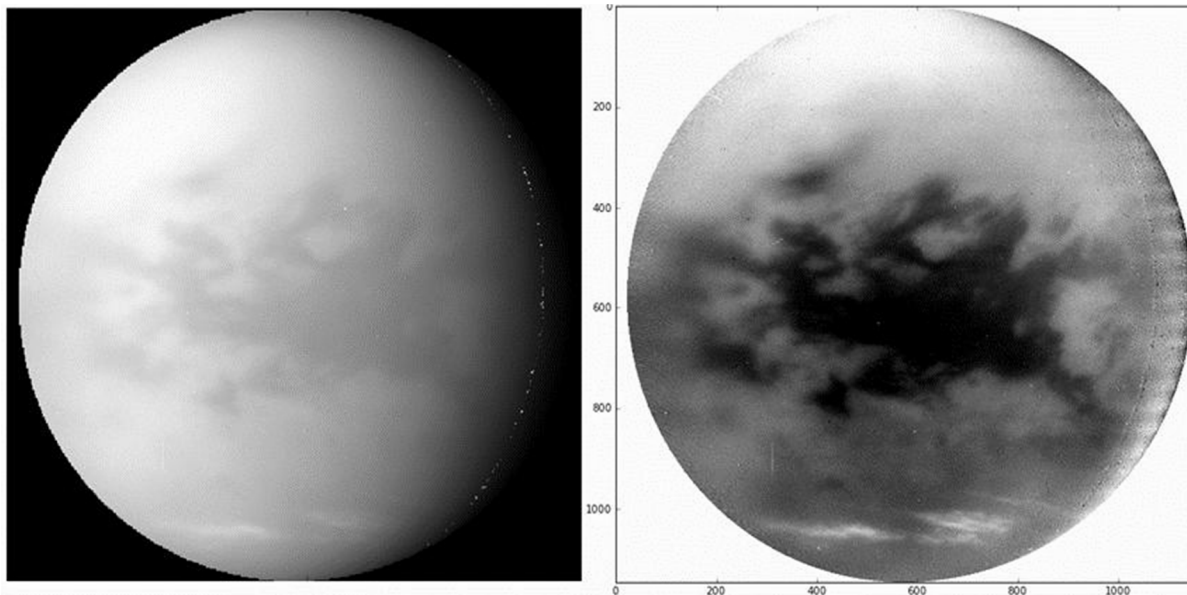
Figure 3.5. Left: Cassini-ISS CL1/CB3 image, calibrated and mapped with ISIS 3 Right: Resultant image of more defined clouds and surface features after left image is enhanced using the CL1/MT1 filter combination image counterpart to remove the haze.

3.5.2 Brightness and Hovmöller Plots

Next we focus on the latitude region where cloud images are mapped to pixel brightness plots as a function of pixel number, such as that shown in Figure 3.6. When the images are mapped, we convert pixels to degrees, which give us a conversion to longitudinal location. When zooming into the cloud region of the image, the pixel brightness peaks are the indicators of cloud location, and when we have a set of consecutive cloud images from the same event, we can determine how the cloud is propagating along the longitudinal axis.
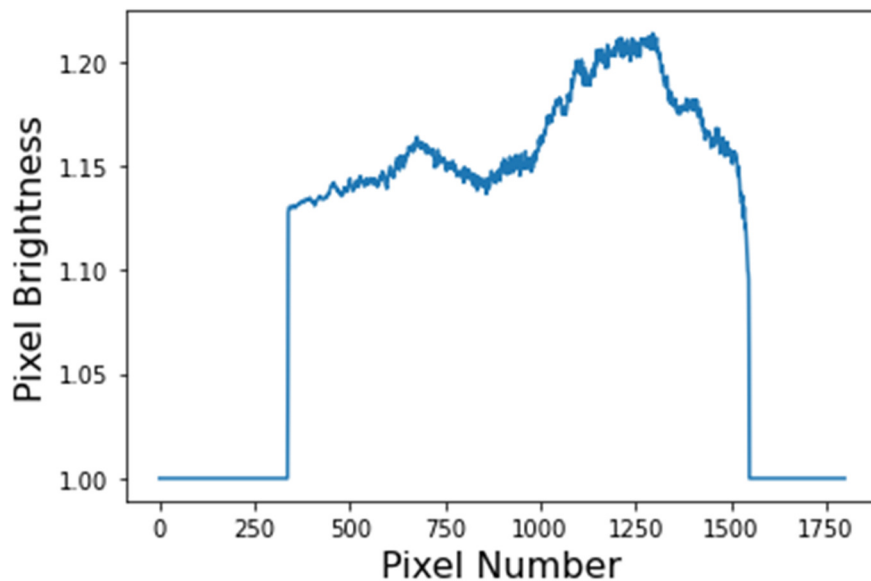
Figure 3.6. Pixel brightness plot produced from the region of enhanced clouds in figure 3.5.

A spatio-temporal plot is produced from the brightness plots by stacking them into a Hovmöller diagram that follows the cloud longitudinal location as a function of time and allows us to better understand the motion of the clouds as they propagate over time (Figure 3.7).
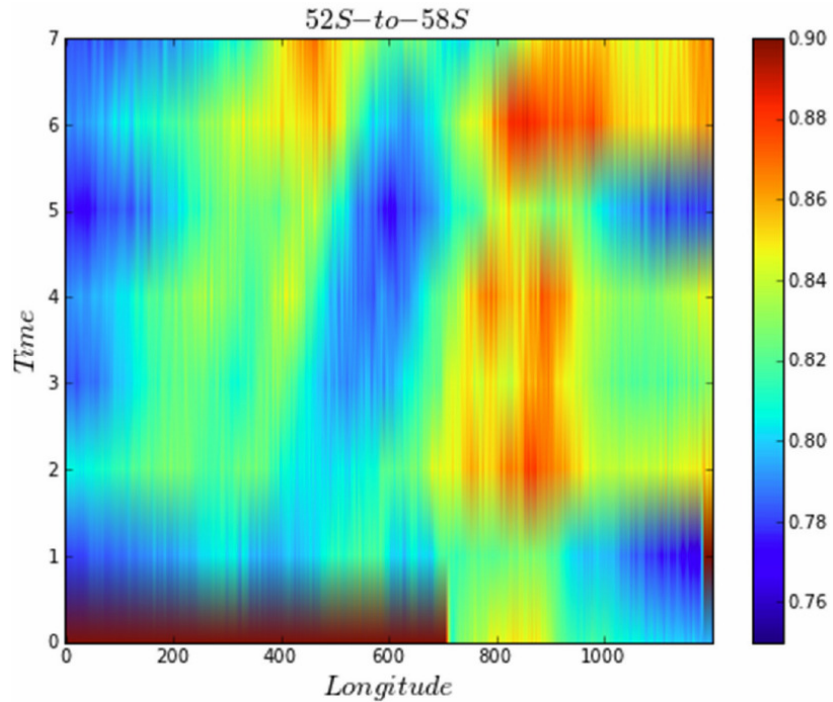
Figure 3.7. Hovmöller diagram highlighting cloud propagation from seven brightness plots produced from consecutive enhanced cloud images.

3.5.3 The Cookbook Files

Every step of the image reduction and data process has been recorded in a manuscript that allows for the continuation of this work applied to all cloud events found in the Cassini ISS observations. A brief example of all the image reduction steps, applied to the image and label files (IMG and LBL) of one raw ISS image is posted in Appendix A of this dissertation. A complete cookbook for this work will be uploaded to the Terrestrial Planetary Atmosphere and Climate Extremes (TPACE) research group website: https://dept.atmos.ucla.edu/jonmitch.

3.6 Methods: The General Circulation Model

The final step of our analysis and interpretation of the cloud phenomena found in the observational data is to compare them against storm simulations based on a well-tested model of Titan's atmosphere. We use an idealized general circulation model (GCM), developed by Faulk, et. al. 2020, which successfully incorporates surface hydrology into an existing Titan atmospheric model (TAM) from Lora et. al 2015. This fully coupled three-dimensional atmosphere and land climate model allows methane to distribute itself within the climate system self-consistently (Faulk et al., 2019), and it is the basis of the work in Chapter 5.

If in doing this comparison we validate the model by identifying robust storm phenomena with particular cloud types, then the model can be used to uncover the underlying dynamics that we cannot see through cloud observations, such as winds or the atmospheric instabilities seen in previous cloud simulations (Mitchell et al., 2011). These tasks, taken together, represent the most thorough characterization and interpretation of Titan's clouds ever performed.

CHAPTER 4

Phenomenology of Titan's Clouds – "Streamers"

4.1 Introduction

Examining the morphologies of Titan's clouds provides a general physical perspective of observed storms and their relation to atmospheric dynamics of the moon. Through analysis of observations of images collected by the Cassini ISS cameras, during Titan flybys, we searched for cloud phenomena to identify various types of storms. Examples of a variety of storm patterns formed at different locations around the moon's globe were found, which indicated a shift in cloud location associated with a change of seasons. Only a limited subset of the cloud image sequences contained sufficient data to identify significant temporal evolution of cloud features. Where possible, we studied this cloud activity to describe storm characteristics and search for time evolution patterns to identify the dynamics behind them, for instance, Rossby and gravity waves, including Kelvin waves.

The goal of this chapter is to show our first complete analysis of ISS observed clouds, which are an archetype of cloud formation we call "Streamers", based on our resultant processed image work. The remainder of this chapter provides a physical interpretation of the observed storm through a combined analysis of the observation of the Streamers, and Chapter 5 will lay out the resultant simulations obtained with the surface hydrology model from Faulk et. al. 2019 for this and other cloud events.

4.2 Streamers Image Set

Observations of a predominant example, shown in Figure 4.1, of a mid-latitude cloud system was captured by the ISS cameras over a period of about 24 hours from December 13 to 14, 2009, after the onset of a new season (NSE) of the Saturn system. The images show methane clouds in the
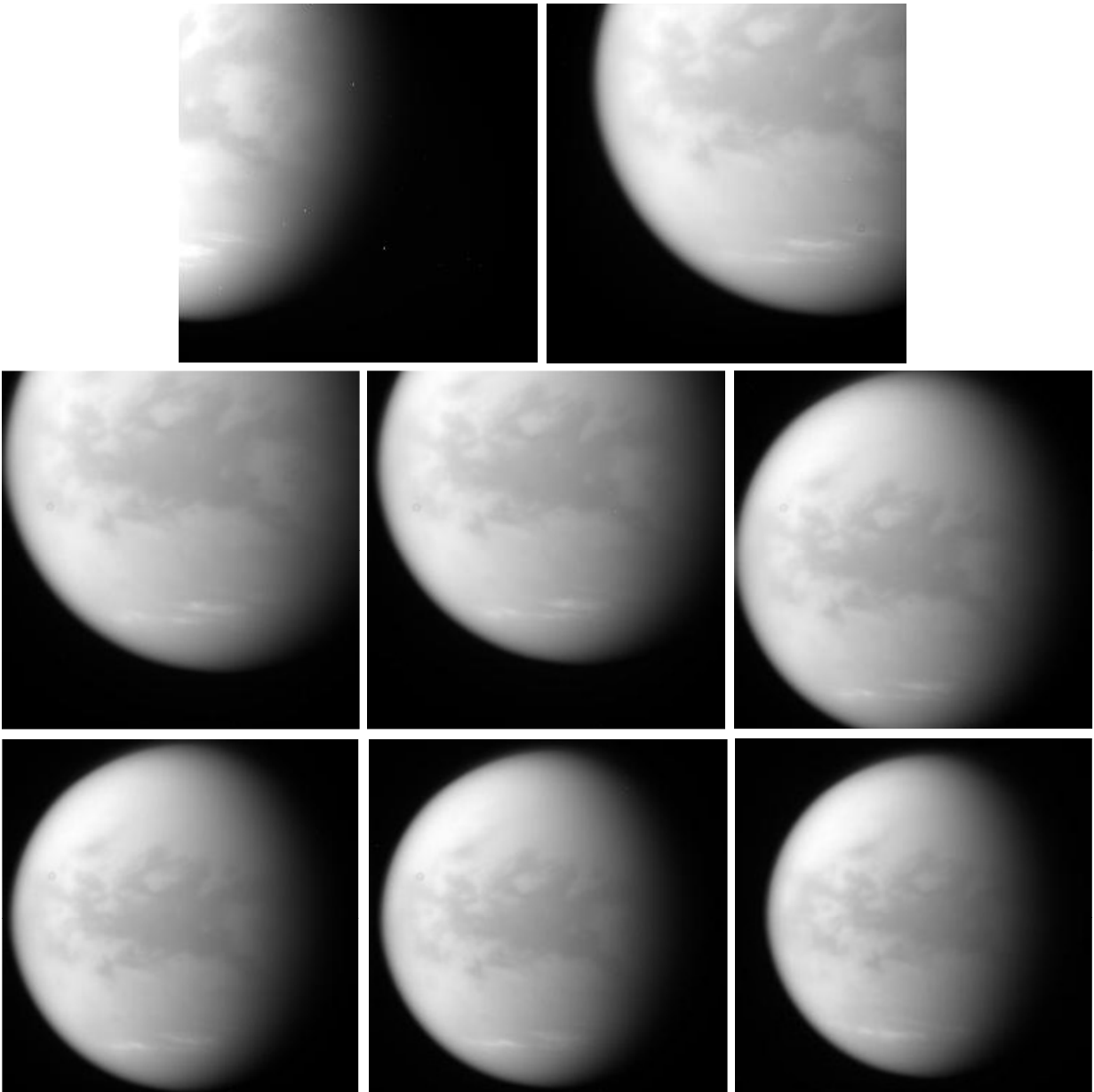
Figure 4.1. ISS image sample of a cloud storm, referred to as "Streamers", taken in the span of 24 hours between 2009-12-13 and 2009-12-14. With the filter combinations: CL1/CB3 (images shown) & MT1/CL1 (for haze removal – images not shown).

troposphere concentrated in a band between 45° and 60° south latitude, a streak-shaped cloud system extending across half the globe, traveling several hundred kilometers during the observation period.

These observations taken by the ISS cameras encompass a large region of Titan. Therefore, in order to identify that region of the moon, a mosaic map figure produced by NASA and Caltech
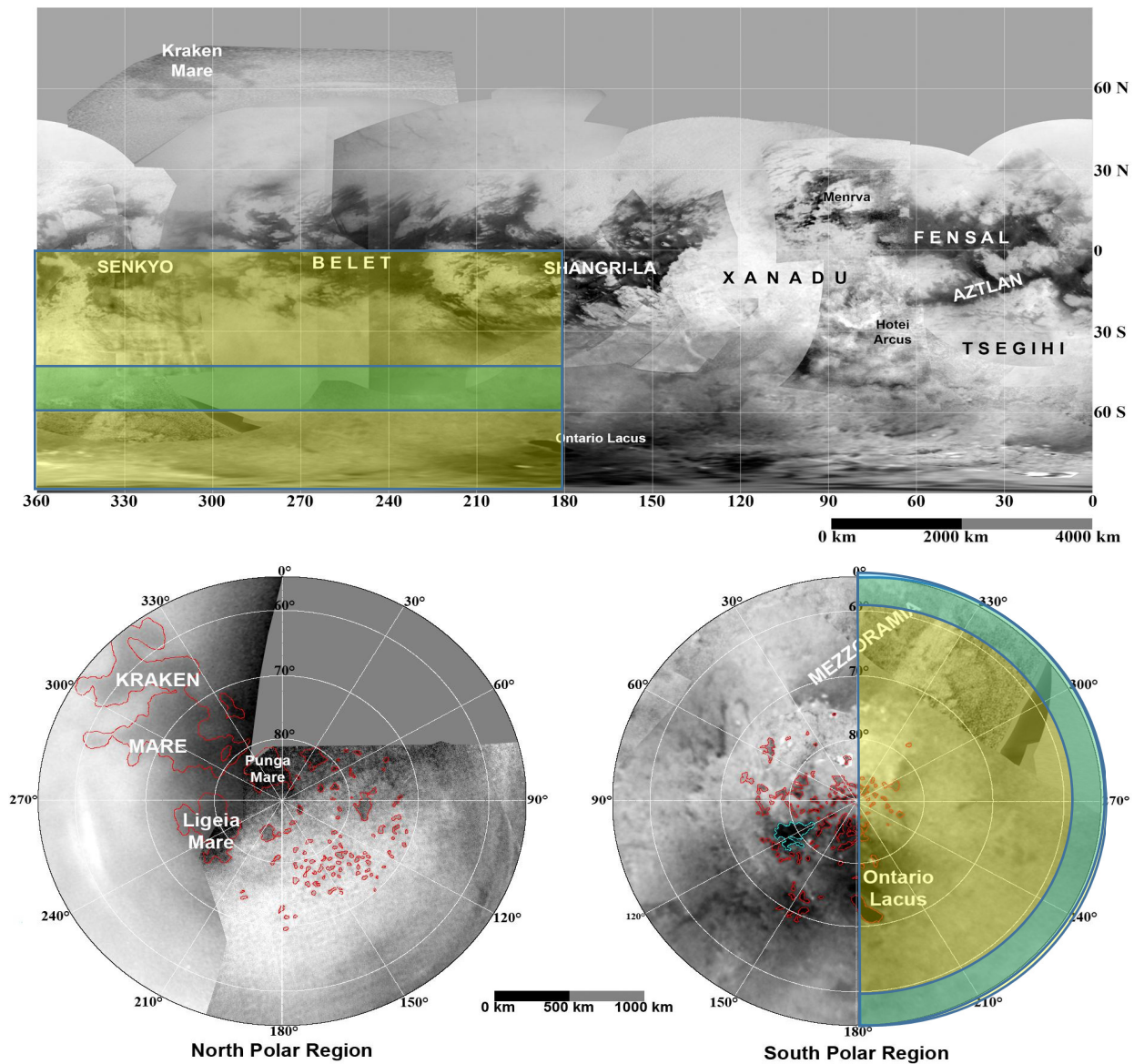
Figure 4.2. Mosaic Map of Titan's features, produced from Cassini radar imaging data. Image Credit: NASA/JPL-Caltech/ASI. Highlights: YELLOW, surface area encompassing the 8 image set. GREEN, region within larger area representing the location of the clouds during this event.

is borrowed. This mosaic is made from Cassini RADAR instrument images which offer a view of the entire surface of the moon (Figure 4.2), with both a rectangular and south and polar views. The yellow highlighted areas represent the region covered by the image sets of the Streamers event, as seen by Cassini.

A green highlighted region is also added to represent a narrower area where the clouds are found within the larger area. The latitudinal location of the clouds roughly expands from 45° to 60° degrees south and the longitudinal location varies as a function of time and can only be seen within 180° to 360° (or 0°-180° West) of longitude. Figure 4.2 also has a polar component with the same highlighted regions indicating the position of the clouds as in the rectangular map. All the clouds from this event are found in the Southern hemisphere.

4.2.1 Streamers Image reduction and Haze Removal

The study of this event starts with the image reduction and haze removal work done to eight sets of ISS images that span 24 hours during the December 13 to 14, 2009 Cassini flyby T- 63. The eight sets include a total of 32 images of clouds, each set containing four images, with the following filter combinations: three CL1/CB3 (near-infrared 938 nm) and one CL1/MT1 (visible 611/619 nm, used for haze removal), each taken a few minutes apart within the set. The first seven sets were taken inside of roughly 12 hours - each set of four shots acquired 2.5 to 3 hours apart from 11:27:05 on December 13 to 00:06:50 on December 14, 2009. Four more images, that make the eighth set, were taken between 11:12:38 and 11:18:02 on December 14, 2009, roughly 11 hours after the seventh set.

The details of a handful of observational parameters for the 32 images, such as image name, mid-time, filter combination and central latitude and longitude, are listed in Table 4.1. The

table highlights an important pattern seen in each set, one CL1/MT1 filter combination image that follows the set of three previous CL1/CB3 images. All images in the set are taken within a timeframe of 4 to 6 minutes and with similar central latitude and longitude pointing.

FILE_NAME	IMAGE_MID_TIME	FILTER_NAME	CENTER_LATITUDE	CENTER_LONGITUDE
N1639397458_1.IMG	2009-12-13T11:27:05Z	CL1,CB3	-30.0323	178.934
N1639397600_1.IMG	2009-12-13T11:29:27Z	CL1,CB3	-29.7831	179.095
N1639397670_1.IMG	2009-12-13T11:31:00Z	CL1,CB3	-30.132	178.736
N1639397726_1.IMG	2009-12-13T11:31:50Z	CL1,MT1	-29.9276	179.182
N1639397878_1.IMG	2009-12-13T11:34:05Z	CL1,CB3	-29.282	89.354
N1639398020_1.IMG	2009-12-13T11:36:27Z	CL1,CB3	-29.6559	89.46
N1639398090_1.IMG	2009-12-13T11:38:00Z	CL1,CB3	-29.6211	89.235
N1639398146_1.IMG	2009-12-13T11:38:50Z	CL1,MT1	-28.2275	91.641
N1639409936_1.IMG	2009-12-13T14:55:12Z	CL1,CB3	-29.3899	110.26
N1639410046_1.IMG	2009-12-13T14:57:02Z	CL1,CB3	-29.8167	109.031
N1639410156_1.IMG	2009-12-13T14:58:52Z	CL1,CB3	-29.8402	109.23
N1639410250_1.IMG	2009-12-13T15:00:34Z	CL1,MT1	-30.0491	108.814
N1639417826_1.IMG	2009-12-13T17:06:42Z	CL1,CB3	-29.8641	109.594
N1639417936_1.IMG	2009-12-13T17:08:32Z	CL1,CB3	-28.6613	110.345
N1639418046_1.IMG	2009-12-13T17:10:22Z	CL1,CB3	-28.7957	110.256
N1639418140_1.IMG	2009-12-13T17:12:04Z	CL1,MT1	-30.2388	109.247
N1639427666_1.IMG	2009-12-13T19:50:42Z	CL1,CB3	-1.0163	115.99
N1639427776_1.IMG	2009-12-13T19:52:32Z	CL1,CB3	-0.743425	116.02
N1639427886_1.IMG	2009-12-13T19:54:22Z	CL1,CB3	-0.667957	116.403
N1639427980_1.IMG	2009-12-13T19:56:04Z	CL1,MT1	-0.747888	116.024
N1639436186_1.IMG	2009-12-13T22:12:42Z	CL1,CB3	-2.51888	115.84
N1639436296_1.IMG	2009-12-13T22:14:32Z	CL1,CB3	-2.86724	116.059
N1639436406_1.IMG	2009-12-13T22:16:22Z	CL1,CB3	-2.52113	116.182
N1639436500_1.IMG	2009-12-13T22:18:04Z	CL1,MT1	-3.2413	115.698
N1639442547_1.IMG	2009-12-13T23:58:43Z	CL1,CB3	-2.83762	116.531
N1639442712_1.IMG	2009-12-14T00:01:28Z	CL1,CB3	-2.81594	115.877
N1639442877_1.IMG	2009-12-14T00:04:13Z	CL1,CB3	-3.09638	116.119
N1639443026_1.IMG	2009-12-14T00:06:50Z	CL1,MT1	-3.09652	116.336
N1639482986_1.IMG	2009-12-14T11:12:38Z	CL1,CB3	-0.943548	102.403
N1639483096_1.IMG	2009-12-14T11:14:28Z	CL1,CB3	-0.981634	103.35
N1639483206_1.IMG	2009-12-14T11:16:18Z	CL1,CB3	-0.800673	106.206
N1639483300_1.IMG	2009-12-14T11:18:02Z	CL1,MT1	-0.82049	106.727

Table 4.1. List of parameters of 32 images (8 sets) of the "Streamers" cloud event from December 13 to 14, 2009.

The sequence of 32 images from the eight sets had photometry and mapping applied to them with the ISIS3 software package, as explained in the previous chapter.
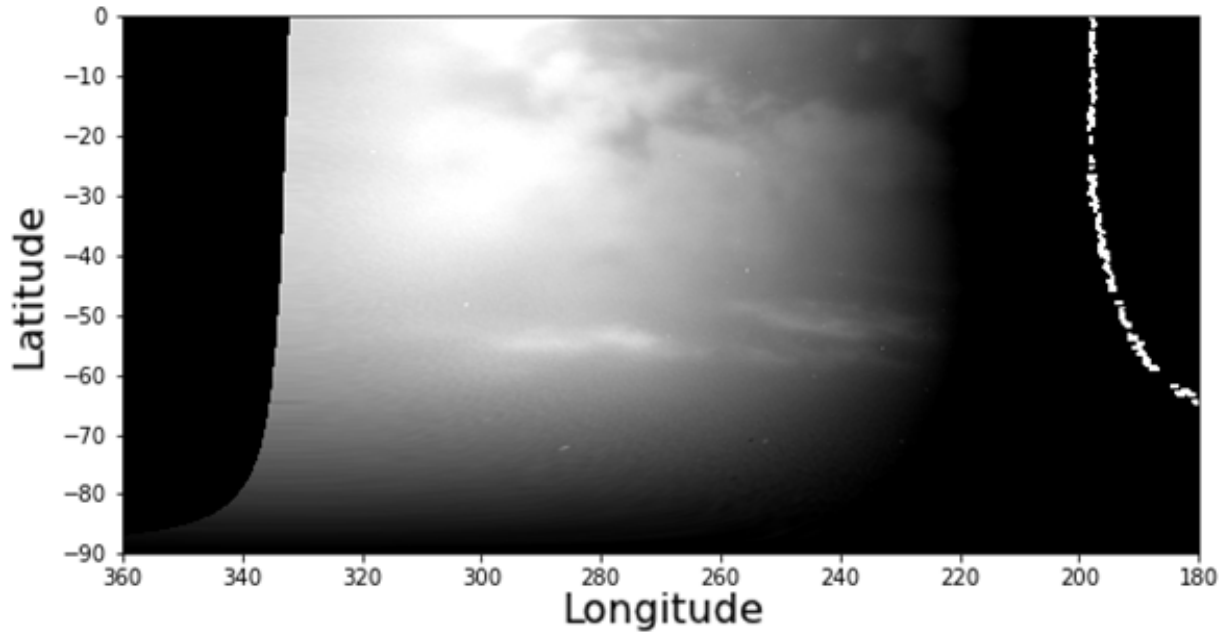
Figure 4.3. Sample ISS, CB3/CL1, resultant mapped image from the 2009-12-13 cloud event.
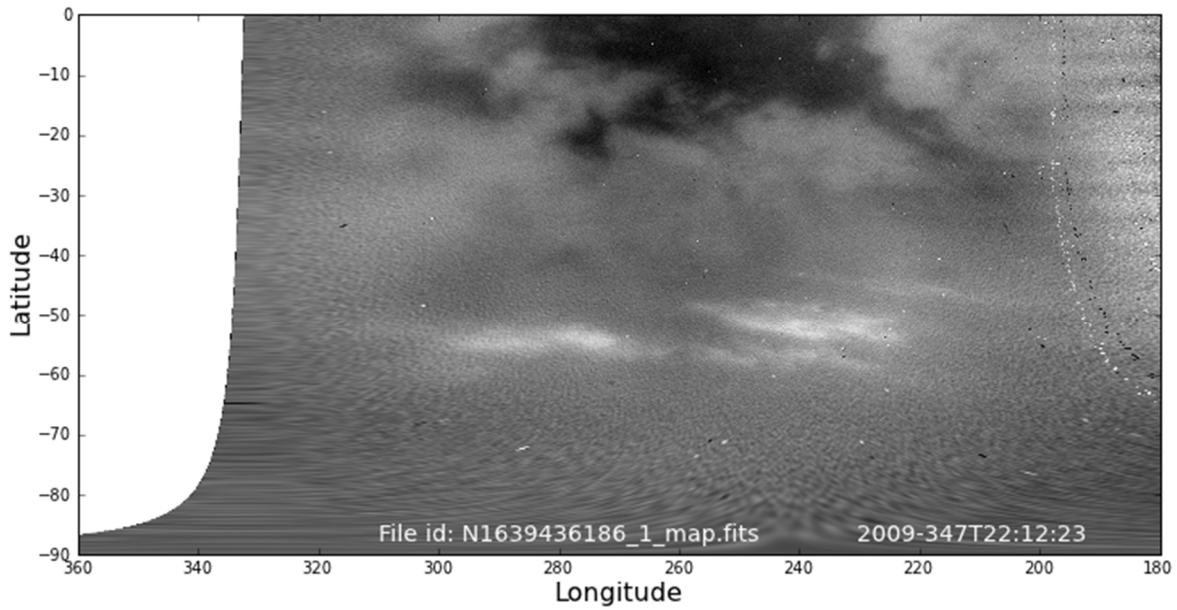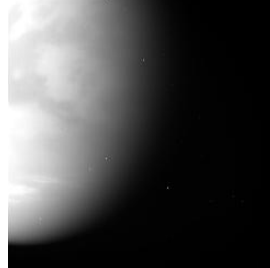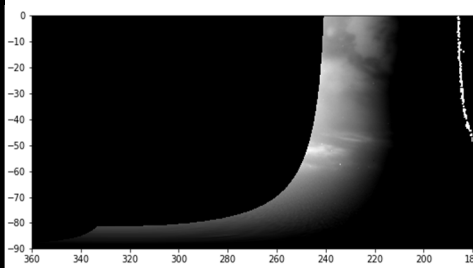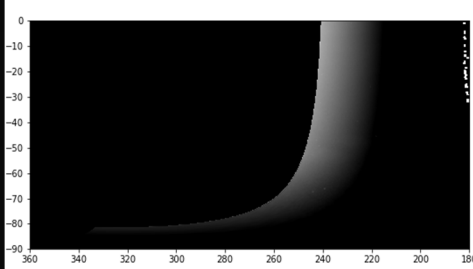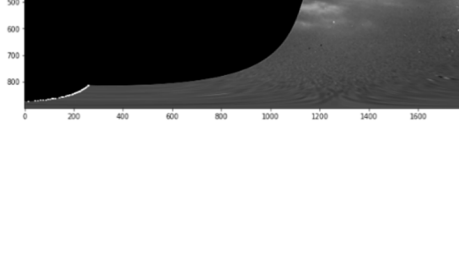
Figure 4.4. Sample resultant cloud enhancement image after haze removal using MT1/CL1 filter applied to image counterpart on Figure 4.3.

We collected the raw (pre-processed), processed and mapped, and cloud enhanced images to show them on a table 4.2. First, a column showing one (of three) CL1/CB3 and the one CL1/MT1 raw images from each of the 8 sets (a total of 16 images) as retrieved from the NASA PDS site. Second, an adjacent column with the 16 CL1/CB3 and CL1/MT1 images (8 of each filter combination) as seen after the photometry and simple cylindrical projection mapping is done, for a total of 16 mapped images. Simple Cylindrical projection is an Equidistant Cylindrical projection with the standard parallel at the equator of the target planet (isis.astrogeology.usgs.gov). Poles, latitudes and longitudes are represented as straight lines. The longitudes and latitudes are equally spaced and intersect at right angles. Last, using primarily a combination of the near-infrared (CL1/CB3) and the visible (CL1/MT1) filters, we add one last column to show how the haze removal step allows for an enhanced view of the clouds against the background. Figures 4.3 and 4.4 show samples of a resultant CB3/CL1 mapped image, and of a resultant cloud enhanced image (haze removed using the MT1/CL1 counterpart image onto the mapped one), respectively.
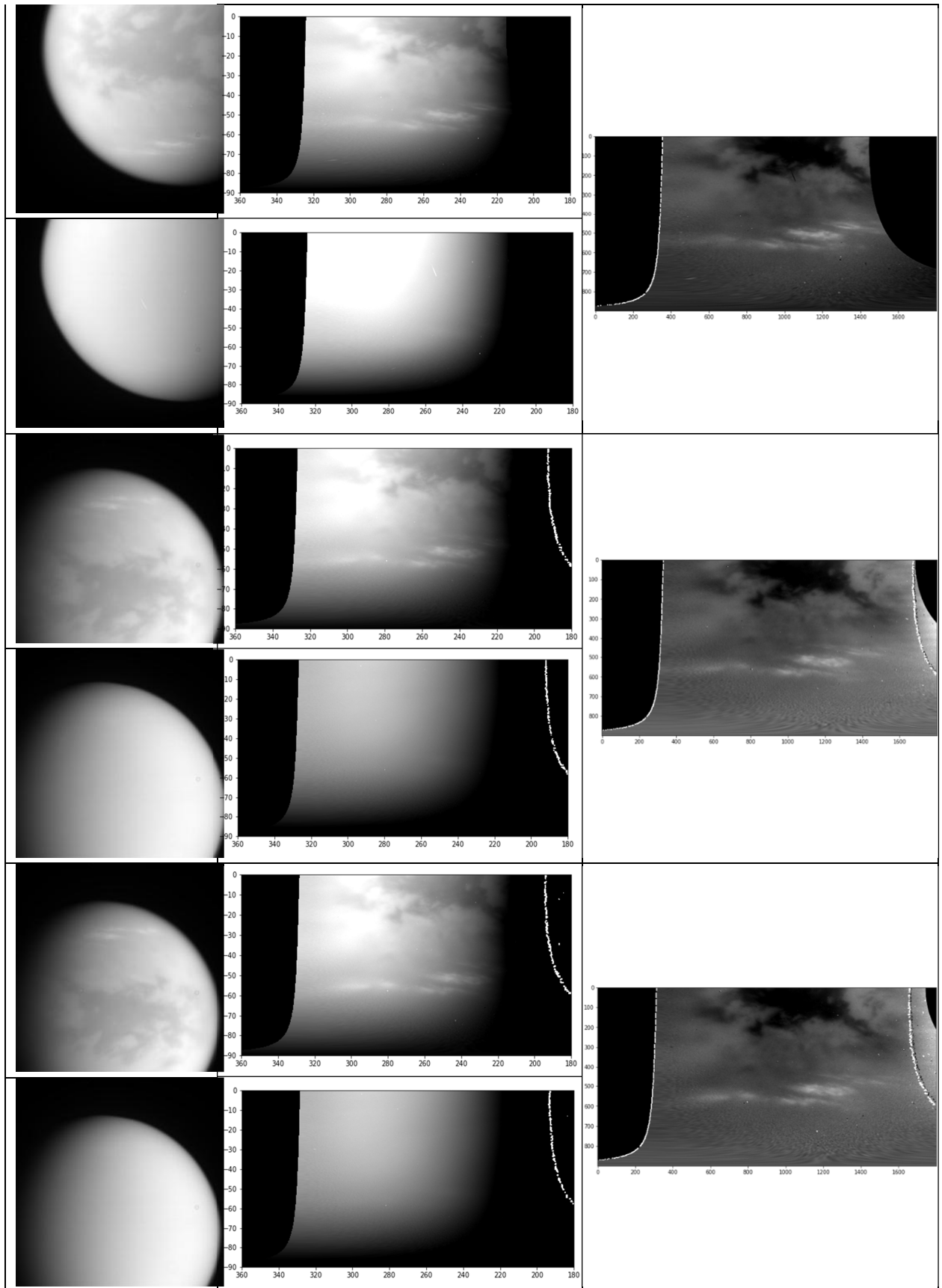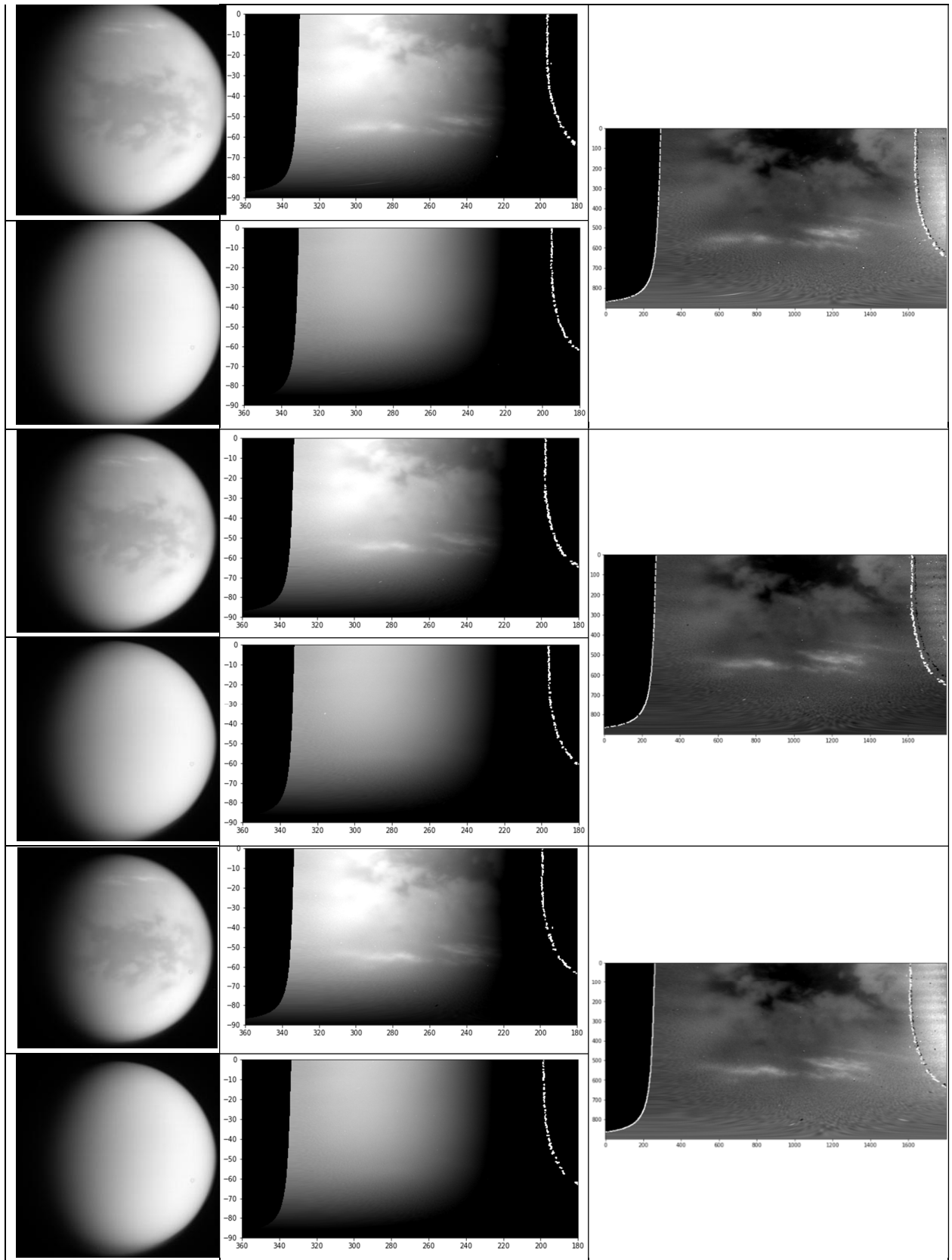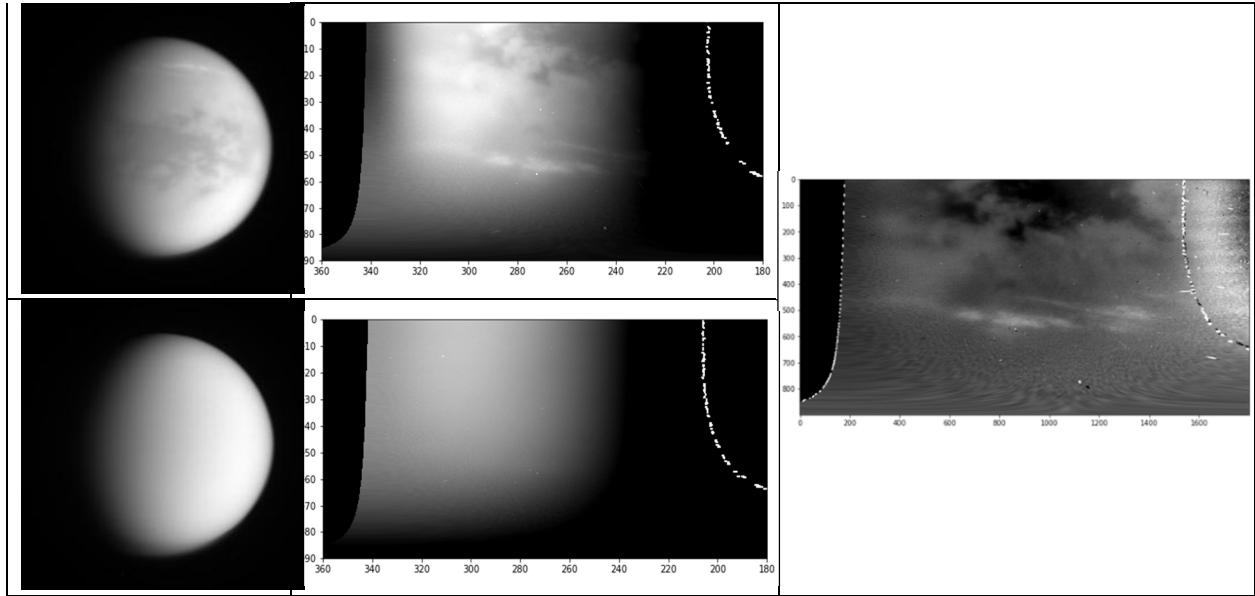
Table 4.2. Streamer cloud image reduction process applied to 16 images from the set (8 CL1/CB3 and 8 CL1/MT1). Steps shown: raw images (left), simple-cylindrical mapped images (center), and enhanced cloud images after haze removal (right). Table starts on page 61 and continues through pages 62, 63 and 64.

4.2.2 Streamers Brightness and Hovmöller Plots

Next, using the first seven resultant enhanced images from Table 4.2, we focus on the 48° to 58° S latitude region to produce pixel brightness plots as a function of longitudinal location. See figure 4.5 below.

Figure 4.5. Top: First 7 resultant images after mapping and haze removal. A clear rectangle with a blue border delineates the 48°-58° S latitude region across the 320°-210° longitudes. Bottom: pixel brightness plots vs. longitude of the highlighted region on the top images.

64

To underline the roles of cloud propagating features, a first spatio-temporal plot is produced from the brightness plots by stacking them into a Hovmöller diagram (Figure 4.6) that will help define the cloud longitudinal location as a function of time to better understand the motion of the clouds as they propagate around Titan's globe.
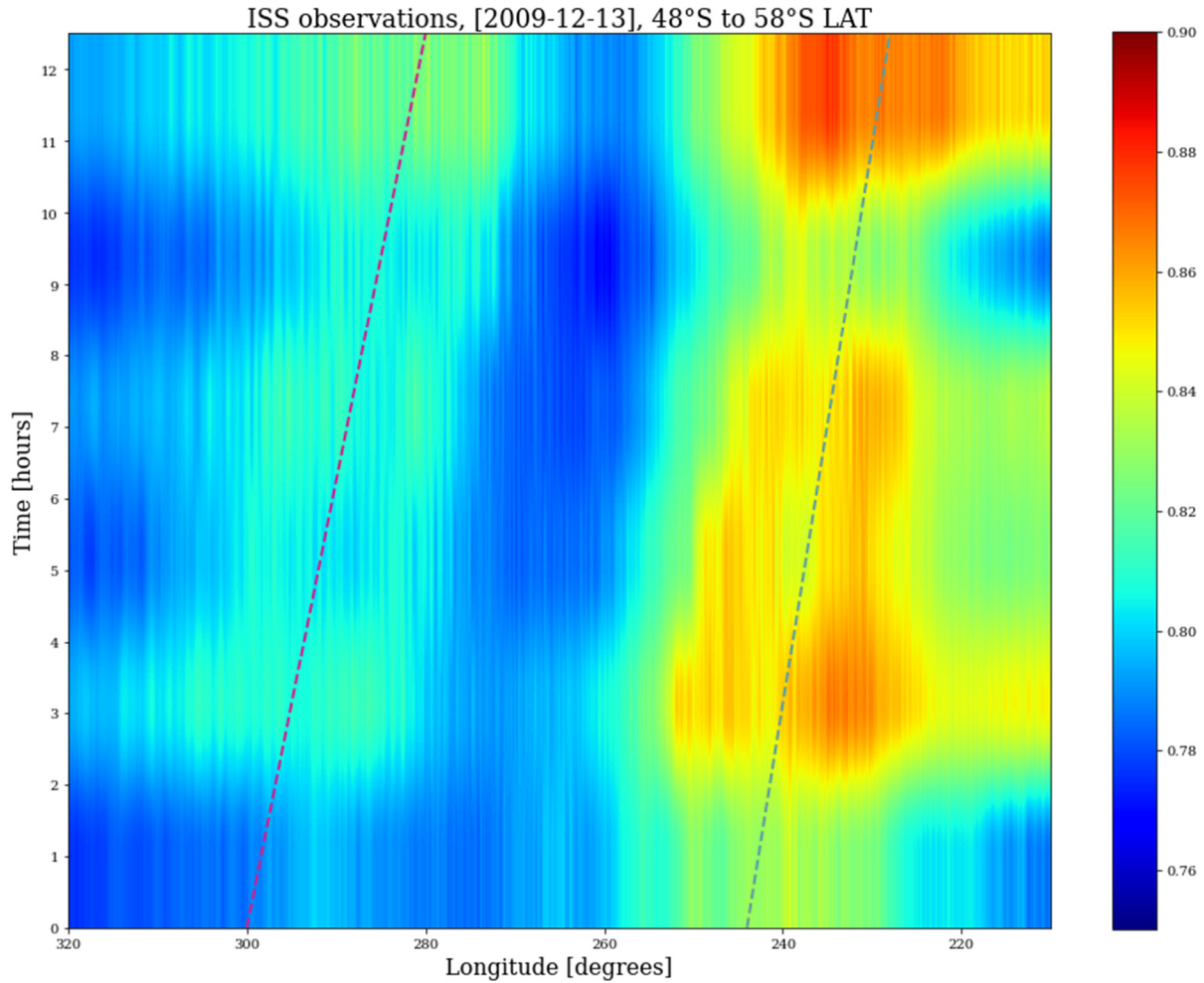
Figure 4.6. Hovmöller diagram of 6 consecutive cloud image brightness plots (~12.5 hour interval), highlighting the role of the waves and how the clouds propagate across the moon between 48° and 58° of latitude, south. Brightness increases from blue to red. Dashed lines are plotted to aid in the calculations of the average speeds at which the clouds move longitudinally against the surface background (Left: Speed 1 - magenta line ~ 1.6°/hr; Right: Speed 2 - blue line ~1.28°/hr).

Although the cloud propagation speed was calculated directly from this first Hovmöller diagram, as it is presented in the next section, it does not include the last set of images (the eighth set) taken ~11 hours later. One more brightness plot is produced to add the information from the last set into a new Hovmöller diagram to show the new location of the clouds (Figure 4.7). This
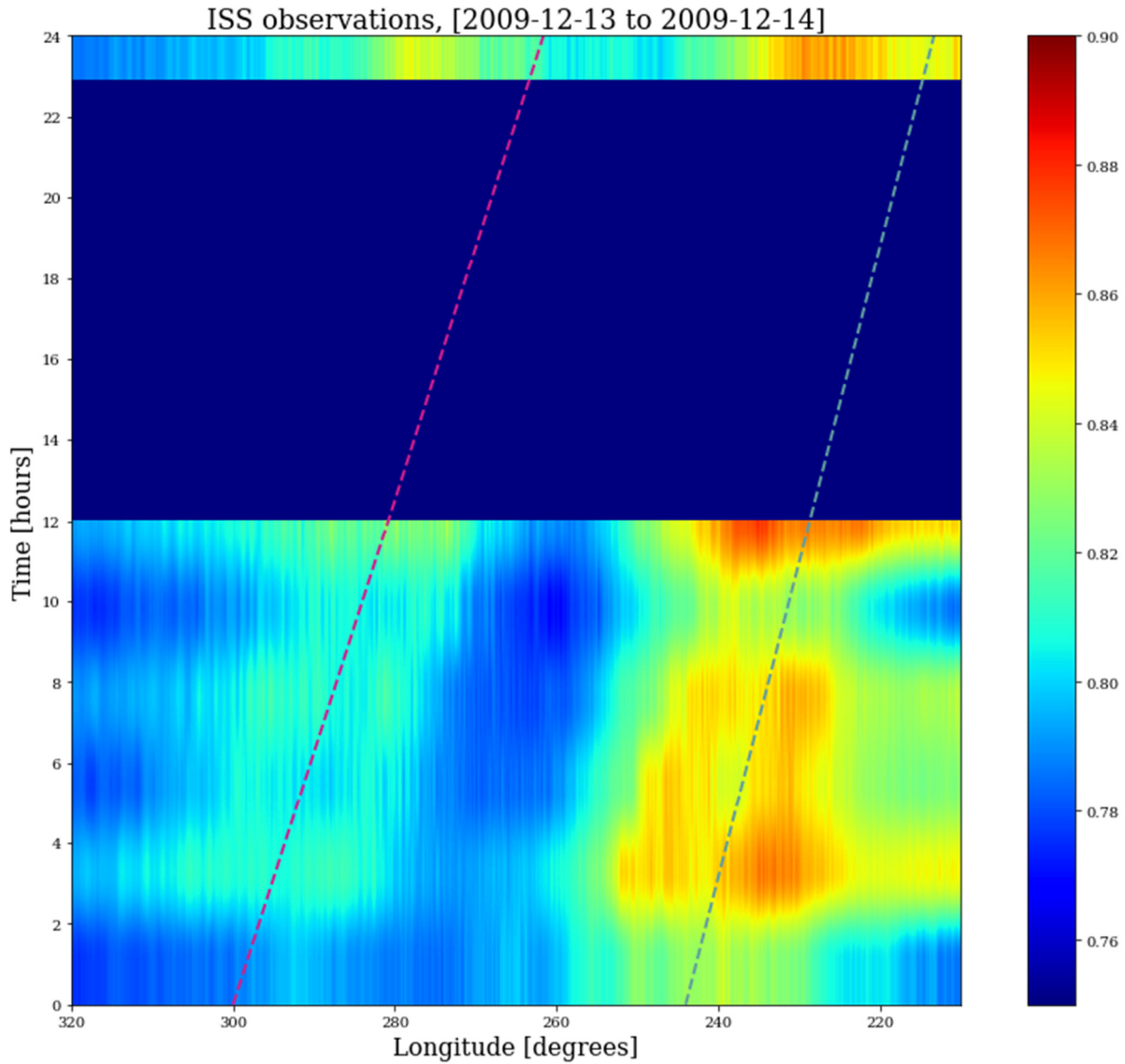
Figure 4.7. Hovmöller diagram produced from the ~24 hour interval adding the 8th image set. A last brightness plot of one image from the 8th set is added to Figure 4.6 to search for the location of the clouds after the 11-hour gap (time gap plotted in blue). The speeds plotted are the same as the ones from Figure 4.6. (Left: Speed 1 - magenta line ~ 1.6°/hr; Right: Speed 2 - blue line ~1.28°/hr).

added slice to the new Hovmöller plot does not yield visual evidence of continuation of the initial cloud mass; nonetheless, it possibly indicates that the storm continues to form cloud masses in the same latitudinal range along similar longitude regions that follow the batch seen in the seven previous images.

4.3 Streamers Cloud Analysis

To further understand the morphology, propagation and evolution of this cloud complex, we divide our analysis into three sections. In the first one, we calculate the speed at which the clouds are moving against the surface background. Then, we search for the type of waves associated with this motion, and last, we look to determine the length of time the cloud event can potentially remain in the atmosphere by using two more sets of images found in the data from two and half weeks after the Streamers event.

4.3.1   Cloud Propagation Speed

The cloud activity seen in the enhanced mapped images on table 4.2, shows the likely presence of two dominant modes of atmospheric variability that govern cloud properties. One faster eastward propagating mode (possibly at the phase velocity of the cloud) and the other a slow westward propagating mode (possibly the group velocity of the wave "packet").

Really slow streaks (the wave packets) are observed at high latitudes going westward but at a much slower speed, moving through the phase velocity. To calculate the speeds at which these waves are propagating, we examine their location in the Hovmöller diagram in Figure 4.6. The calculation of the two speeds are performed by pinpointing both the median longitudinal

locations, confirmed with the displacement of the peaks in the brightness plots from Figure 4.5, and the times at which those images were taken, and calculating the slope of the line connecting these points on the Hovmöller plot. Each of the two propagation speeds (inverse of the slopes of the magenta and blue lines on Figure 4.6) are plotted in Figure 4.8.
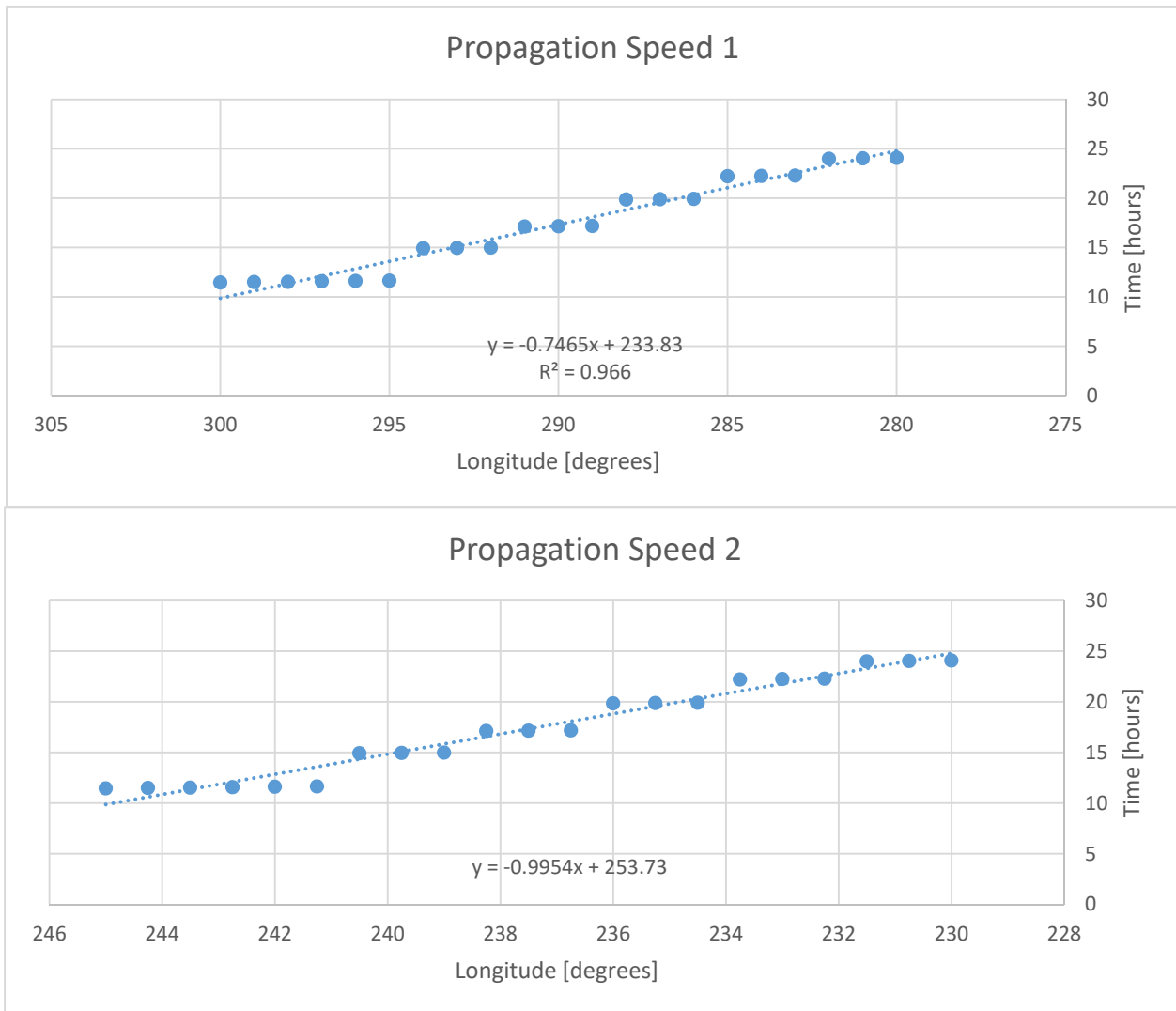
Figure 4.8. Excel plot representing the longitudinal location of the cloud brightness peak - in degrees, and time difference - in hours, between 21 images. The blue lines represent speeds found from the change of location (in degrees) per unit time (in hours). The time of all near-infrared filter images (CL1/CB3) have been included in this calculation.

After obtaining a change in longitudinal position as a function of time (in degrees per hour), the values are translated to find the speed in m/s, using the known radius of Titan, R_{Titan}=2572 km at the latitudinal location of the Streamers, ~50°S, to determine the distance in meters per degree on the moon's circumference at that location. With a simple time unit conversion, the two values are found to be 5.1±1 m/s and 6.8±1 m/s.

In an attempt to confirm the cloud motion directly from eight resultant enhanced mapped images, they are stacked and aligned to be converted into movies of clouds moving across the moon's surface background. The movies provide an opportunity to visually verify what the plots suggest about the presence of two speeds within the propagating cloud. This second speed is much more challenging to spot from the Hovmöller diagrams and consequently only measurable from the observations themselves by stacking and aligning the image set as seen in Figure 4.9.

From these observations, we calculate the speed of the faster eastward propagating wave, by selecting different cloud "packets" within the storm and measuring each of their phase speeds directly from the enhanced mapped images. Seven resultant enhanced mapped images, six from the first seven sets of 11-hour expanse and one from the eighth set from 11 hours later are used for this measurement. At the given latitudes, we consistently find that the speeds for each of the packets is roughly 25 m/s.

A sample of the movies produced with the images in Figure 4.9 are available on the Terrestrial Planetary Atmosphere and Climate Extremes (TPACE) research group website: https://dept.atmos.ucla.edu/jonmitch.

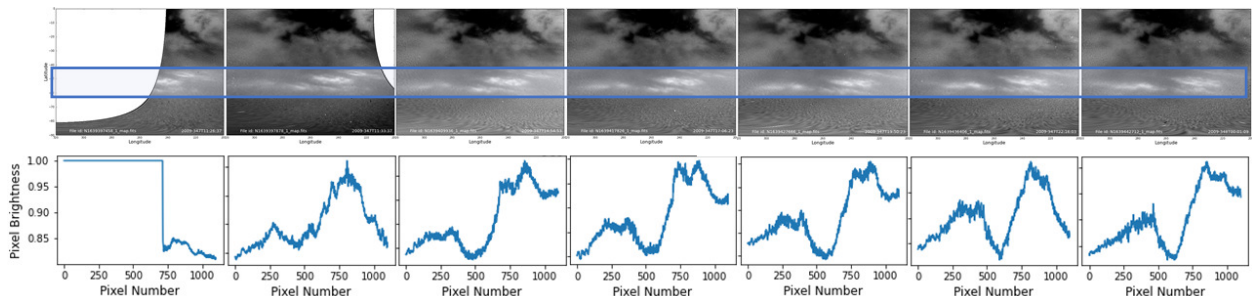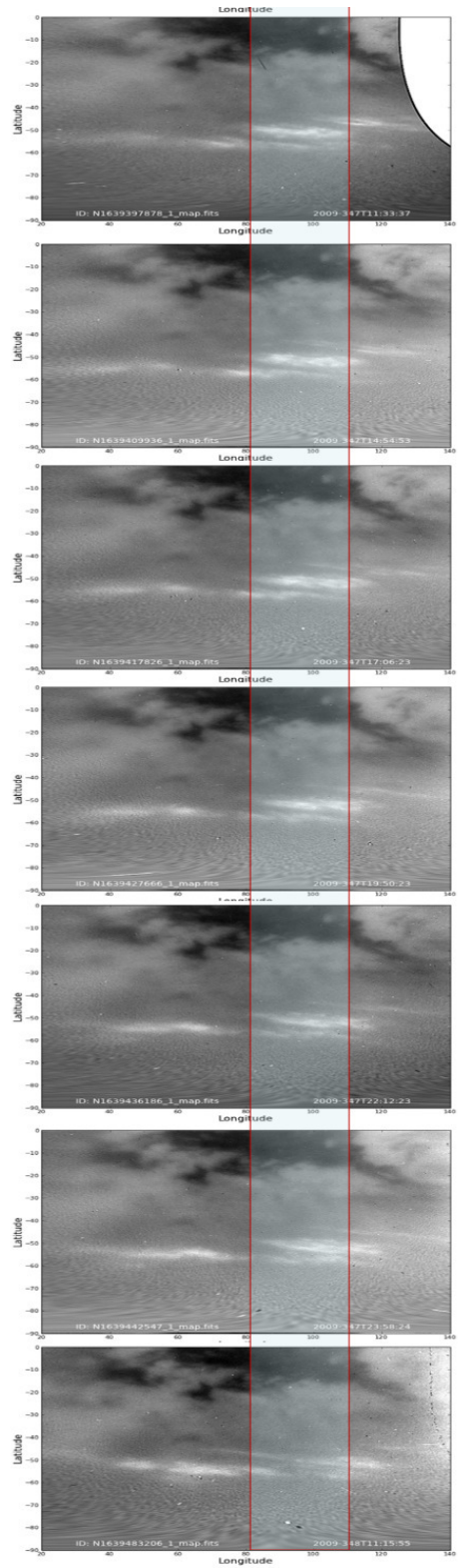Figure 4.9. First 7 resultant images after mapping and haze removal. A clear rectangle with a red border delineates the same longitudinal region to highlight the propagation of the clouds as time goes by in the 12 hour time frame.

4.4 Persistence of the Streamer Cloud Event

Determining the exact time when this storm formed is out of our reach because of the lack of data to pinpoint that initial date. Nonetheless, the span of the Streamers cloud event as detailed in the previous sections appears to persist much longer than the original observed 24 hours.

4.4.1 17 Days Later

Two and a half weeks later, on December 30 to 31, 2009, a cloud system similar to the one in this initial study is seen at the 45° to 60° latitude location, westward of where the streamer clouds were found on December 13-14, 2009. The details of a handful of observational parameters for the eight images, such as image name, mid-time, filter combination and central latitude and longitude, are listed in Table 4.3.

FILE_NAME	IMAGE_MID_TIME	FILTER_NAME	CENTER_LATITUDE	CENTER_LONGITUDE
N1640861926_1.IMG	2009-12-30T10:14:48Z	CL1,CB3	-13.6367	105.847
N1640862036_1.IMG	2009-12-30T10:16:38Z	CL1,CB3	-13.6079	106.4
N1640862146_1.IMG	2009-12-30T10:18:28Z	CL1,CB3	-13.4011	106.724
N1640862240_1.IMG	2009-12-30T10:20:12Z	CL1,MT1	-13.3063	109.184
N1640947416_1.IMG	2009-12-31T09:59:37Z	CL1,CB3	-14.4865	90
N1640947526_1.IMG	2009-12-31T10:01:27Z	CL1,CB3	-14.4425	87.045
N1640947636_1.IMG	2009-12-31T10:03:17Z	CL1,CB3	-14.0011	90.968
N1640947730_1.IMG	2009-12-31T10:05:01Z	CL1,MT1	-14.8985	90.948

Table 4.3. List of parameters of 8 images (2 sets) of a cloud event following the Streamers, from December 30 to 31, 2009.

This event is found in 2 sets of images, each containing 3 CL1/CB3 and 1 CL1/MT1 filter combination images. Figures 4.10 and 4.11 are samples of the resultant enhanced mapped images,

from both the December 30 and December 31, 2009 sets - respectively, after they were reduced in
the same way as were the first 8 sets.
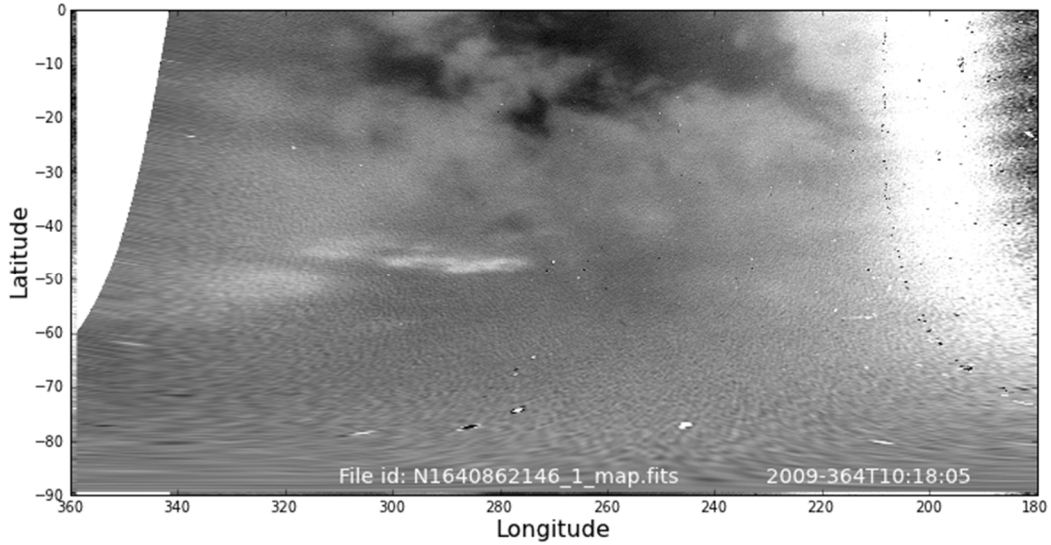
Figure 4.10. Enhanced image, after mapping and haze removal, of a cloud event found on
December 30, 2009. Clouds are seen in the same latitudinal location as the December 13 to 14 set.
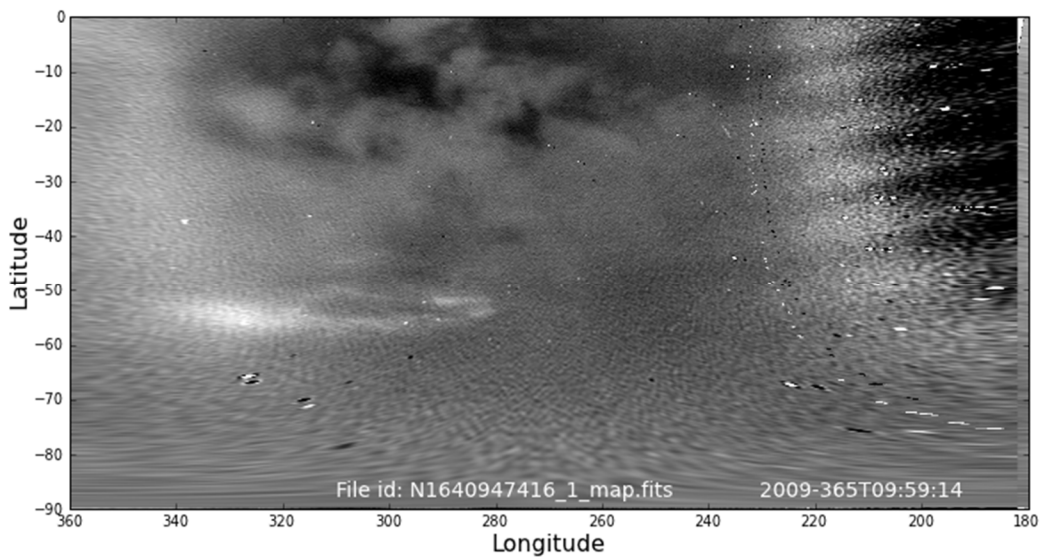
Figure 4.11. Enhanced image, after mapping and haze removal, of a cloud event found on
December 31, 2009. Clouds are seen in the same latitudinal location as the December 13 to 14 set.

After all the images in both sets were processed and brightness plots were obtained, two Hovmöller diagrams were produced with the short time span of ~4.5 mins showing each individual set of three images (Figure 4.12). The clouds, as seen in Figures 4.10 and 4.11, are located in the 310° to 360° longitudinal region. A complete Hovmöller diagram stacking all 10 sets is presented in the next section (Figure 4.11).
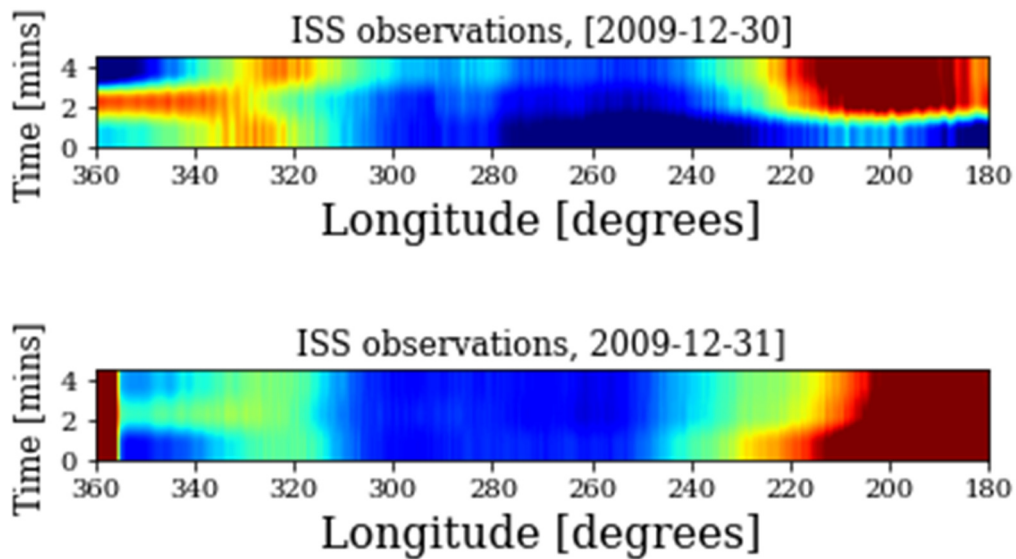
Figure 4.12. Hovmöller diagram result from 2 image sets of clouds found in the December 30-31, 2009 observations. The latitudinal location of the clouds is similar to the "Streamer" clouds, in the 310°- 360° Longitude range.

4.4.2   Analysis to Determine Event Persistence

The last step to estimate the time it would take the Streamers event to move around the globe of Titan and return to a similar longitudinal location to that of the original cloud data is to determine whether or not the clouds seen 17 days later can be a continuation of the same storm from December 13 to 14.

A Hovmöller diagram (Figure 4.13) that spans the entire longitude range of 360° is

produced in which all events found in the data from 2009-12-13 until 2009- 12- 31 are included. The image slices are separated by blue regions to indicate the time gaps between them, and it is important to note that cloud and surface background features only appear within the 180°-360° longitudinal range of the entire 360° span.

The latitudinal location of the new clouds shown in Figures 4.12 and 4.13 is similar to that of the earlier Streamers clouds, and the plots distinctly indicate that the new cloud features are wrapping from the west from the 360^0 longitudinal position reaching east to around 310°. The magenta and blue lines are extrapolations based on the propagation speeds that were calculated in Section 4.3. The magenta dashed line, which represents a displacement of ~1.6°/hr or 5.1±1 m/s, clearly shows that the new clouds are in a location predicted by this propagation speed, and the blue line (propagation speed ~1.28°/hr or 6.8±1 m/s) traces a path that closely follows the new cloud location (and perhaps it could be seen if that part of Titan was visible in the images).

Since the exact time when the new cloud storm is found in the data from 16 to 17 days $(1.3824 \times 10^6 - 1.4688 \times 10^6$ sec) is known, there is an opportunity to calculate whether or not this time interval matches numerically, and an approximate speed needed to travel around the globe and be roughly back in the longitudinal location of 310^0 to 360^0 degrees can be calculated. The two propagation speeds previously calculated from the earlier data and Titan's radius, $R_T = 2.6 \times 10^6$m, combined with the average latitudinal location of the clouds, LAT ~50^0 (0.87 radians), the calculation yields timespans between 17-19 days for a storm such as the Streamers to move back around the globe almost to the same point where they were first seen, which is approximately the time in which the clouds are seen again in the observations.
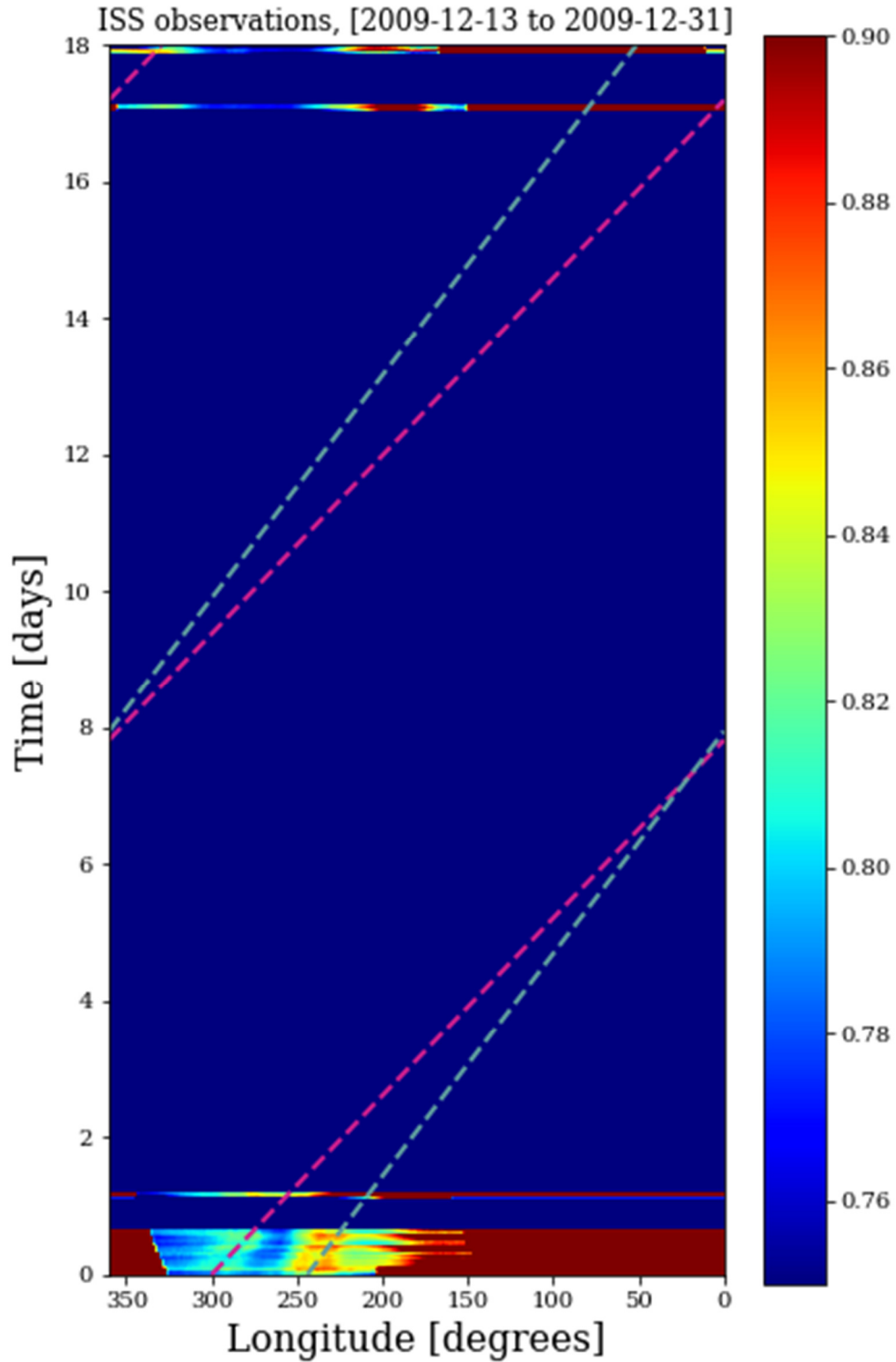
Figure 4.13. Hovmöller diagram from 10 image sets found in the December 13-14 and the December 30-31, 2009 observations. The later images are stacked on top of the earlier ones, with a gap (blue space) that indicate the time between the events. Both propagation speeds are plotted throughout. Speed 1 - magenta line ~ 1.6°/hr; Speed 2 - blue line ~1.28°/hr.

4.5 Atmospheric Waves: Gravity and Rossby

The mechanism behind the motion of the clouds is associated with atmospheric waves, such as Rossby or gravity waves. We search for time evolution patterns to identify the dynamics of the waves. Based on the results of the cloud speeds in the previous section we can now investigate the nature of the waves involving that motion.

Rossby waves, a type of inertial planetary scale wave naturally occurring in rotating fluids, are large-scale atmospheric waves that can propagate in the zonal and meridional directions. On Earth they are found in high altitude winds and are associated with pressure systems and the jet stream and are known to have a great influence on weather.

Gravity waves are typically generated when the force of gravity or buoyancy tries to restore equilibrium in a fluid medium or at the interface of two media. Kelvin waves, a type of gravity waves, balance Coriolis forces against a topographic boundary or waveguide (such as the equator), and it is a non-dispersive wave that can be found close to the equator (Equatorial Kelvin waves) or in higher latitudes.

Free gravity waves:

We start by analyzing the gravity wave phase speed, C_g, with the vertical wave number, m, where m is non-dimensional, and we assume it can only have integer values of π.

$$Cg = NH/m$$

The gravity waves are estimated to be in the first baroclinic mode (the gravest mode), when m=π. The value for the buoyancy oscillation frequency, N, is taken from the Huygens probe data ($N=5\times10^{-3}$ s^{-1}) and the scale height, H, is the height roughly up to the cold trap with $H = 40\times10^3$ m.

With the assumption that the calculated speeds between 5.1±1 m/s and 6.8±1 m/s are correct, the only way to slow this wave down would be to give it a finer vertical structure with a higher wave number that would have to be on the order of ~20.0. This would mean that between 0 km and 40 km of altitude there would be 20 cycles in the wave structure. Therefore, the basic conclusion is that there is no reasonable wave number that yields a slow enough gravity wave to match the slow speeds found from the observational data. This leads to the conclusion that the waves associated with the slow mode of these clouds are not gravity waves. However, gravity waves, in particular equatorial Kelvin-like waves, could be associated with the fast mode speed found to be ~25 m/s, and that will be investigated through model simulations in the next chapter.

Free Rossby waves on a beta plane and zero zonal flow:

In zero background flow, Rossby waves have phase speeds of $C_R = -\beta/k^2$, where $\beta = df/dy$ is the gradient of the Coriolis parameter and zonal wave number:

$$k = \frac{n}{a \cos \phi}$$

With a non-dimensional zonal wave number of $n=1$, $a=2575 \times 10^3$ m, $\phi=55\pi/180$ rad, $\Omega=2\pi/86400/16$ rad, and with $\beta=2\Omega/a \cos \phi$, then:

$$C_R = \frac{\beta}{k^2} = -4m/s$$

A zonal-wavenumber-1 Rossby wave has a phase speed of approximately –4 m/s. The magnitude of this estimate is much more in line with what is observed for the Streamers, but it is westward, while the observations show eastward propagation. There must be an eastward wind of ~10 m/s to account for the ~5-m/s eastward Streamers velocity.

At this point it is difficult to pinpoint the wave nature of the fast mode found in the

observational data. Therefore, the cloud propagation associated with this fast mode and overall influence of waves on the observed storms will be explored further in the next chapter.

4.6 Summary

To summarize thus far, Cassini observations of the southern-hemisphere mid latitudes around 2600 days following southern summer solstice (SSS) revealed the presence of "Streamer" clouds with the following characteristics: (1) a large-scale, roughly zonal-wavenumber-1 assemblage of clouds propagating to the east at around 5 m/s; (2) smaller clouds embedded in the larger one propagating about 5 times faster; and (3) the cloud complex persists for an almost complete circumnavigation over ~2 weeks. We hypothesized that the larger mode could be a slow-moving Rossby wave (or wave packet), in which case its propagation speed is a measure of the advection due to the background zonal winds. We also hypothesized that smaller, fast clouds traveling ~25 m/s are some kind of gravity waves. The Huygens measurement of the background static stability indicates that the gravity waves either occupy a small fraction of the total depth of the troposphere or have a large vertical wavenumber (or some combination thereof).

CHAPTER 5

Observations to GCM Connection

5.1 Introduction

The spatio-temporal distribution of Titan's clouds provides fundamental insight into Titan's methane weather; however, they do not tell us about storm dynamics – how they form, evolve, propagate, etc. Therefore, a final task involving the analysis is required, namely to connect it with a model of Titan's storms to gain physical insight into cloud phenomena. If in doing this comparison we validate the model by identifying robust storm phenomena with particular cloud types, then the model can be used to reveal the underlying dynamics that cannot be seen through cloud observations, such as winds or the atmospheric instabilities seen in previous cloud simulations (Mitchell et al., 2011). This is the task of the final chapter, which represents the most thorough characterization and interpretation of Titan's clouds ever performed.

5.2 The Titan Atmosphere Model

Titan's large-scale topography, consisting of low- and mid-latitude highlands and high-latitude lowlands, drives the moon's hydroclimate. Simulations of Titan's climate are performed using the Titan Atmosphere Model (TAM; Lora et al., 2015) with full surface hydrology (Faulk et al., 2020). TAM is an updated version of the model used for the study of the "arrow" and "streak" cloud events in Mitchell et. al., 2011. It employs a simplified model of moist convection and realistic representations of radiative transfer and surface methane hydrology. This model

configuration produces simulated storms that compare favorably with the seasonal evolution of observed clouds. Figure 5.1 is a zonal-cutaway schematic, borrowed from Faulk et al., 2019, that conveys several key features of Titan's climate:

1- Weather is both seasonal and spotty.

2- Titan has global topography, with high-elevation low latitudes and low-elevation high latitudes (it is an oblate spheroid).

3- Surface liquids only appear persistently at high-latitude low elevations, and a global methane "aquifer" likely connects them.
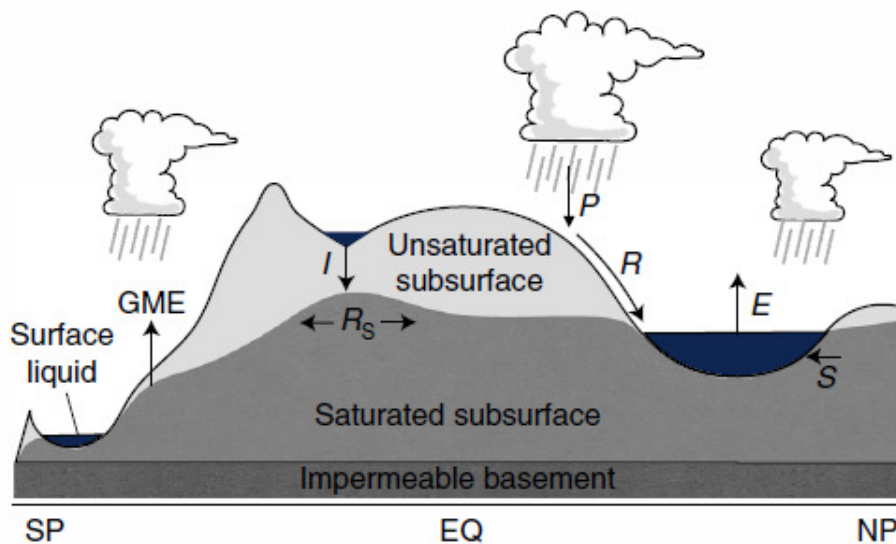
Figure 5.1. Schematic of the Titan Atmosphere Model (TAM; Lora et. al. 2015) with full surface hydrology [Faulk et al. 2020]. Surface liquids precipitate (P) on the surface, infiltrate (I) into the surface, runoff (R) and evaporate (E and GME). The saturated subsurface diffuses laterally (Rs) and seeps (S) into surface reservoirs.

5.2.1 Simulation Results for a Titan Year

The model is run at T21 horizontal resolution (32 latitudes x 64 longitudes) with 30 vertical levels

for 51 Titan years. All results shown here are for the 52nd year of the simulation starting at the fall equinox. A space-time (Hovmöller) diagram of the logarithm of zonal-mean precipitation over an entire Titan year of simulation (Figure 5.2) highlights large events that are further enhanced as the simulation goes to shorter intervals.

Figure 5.2 compares a 10-daily output simulation (left) with 6-hourly data (right). Distinct precipitation features are present in the Southern and Northern Hemispheres. Features that occur at the latitude of the Streamers (25°S-60°S) starting around day 3000 and lasting until day 5500 are revealed. There is also a larger precipitation event at day ~9000 that spreads across the equator and is followed by weakening precipitation at all latitudes. Although southern-hemisphere precipitation is located in low-to-mid latitudes from day 1500-5500, there is obvious variability in time. A clear box is placed in a "region of interest" between days 4000 – 6000 to highlight a significant precipitation time span that we are interested in exploring further.
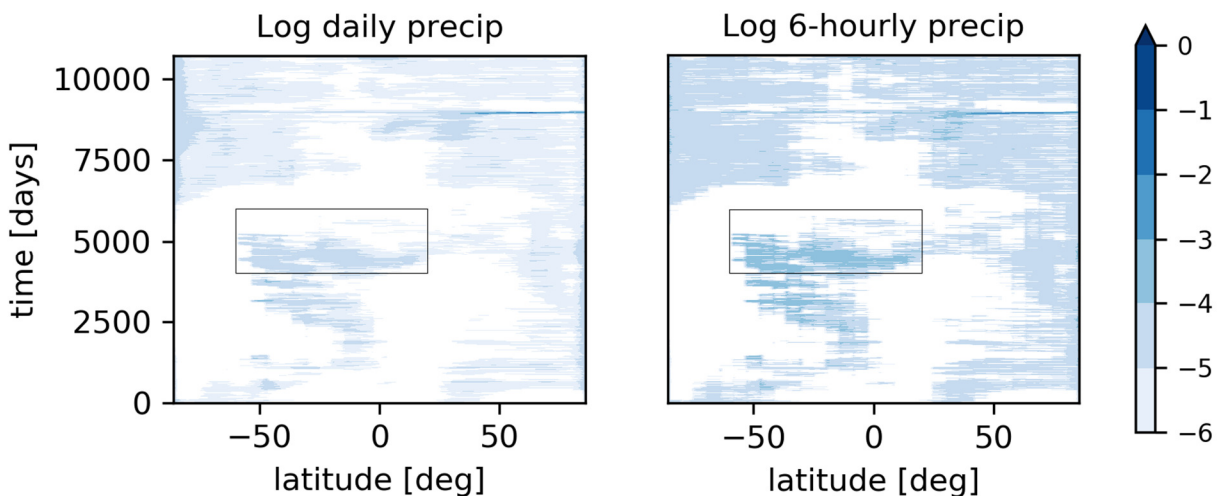
Figure 5.2 (Left) Zonal-mean precipitation (mm/day) of the 52nd year of a Titan GCM simulation with data averaged over 10-day intervals. (Right) Same as the left panel for 6-hourly intervals. A rectangle delineates a "region of interest" with significant precipitation events between days 4000-6000.

Later in this chapter, we focus on the region of interest (clear box in Figure 5.2) matching a temporal range of events we see in the observational data, which indicates that observed events can be replicated in the simulations.

5.3 Analysis of Streamers Event from Simulations

SSS occurs in the model 2545 Earth days following fall equinox, and the Streamer clouds occur on December 13, 2009, ~5100 days after fall equinox; therefore, the analysis is focused between days 4800-5200.

Closer inspection of a Hovmöller diagram of the logarithm of 6-hourly precipitation averaged in latitude from 25°S-60°S during days 4800-5200 reveals the presence of two eastward-propagating signals (Fig. 5.3). There is a slow-eastward zonal-wavenumber-1 mode and a fast-eastward mode with a zonal wavenumber of ~1- 2. These and other modes are present throughout this range of times in dynamical fields (winds, divergences, pressures; not shown), but the precipitation is spottier. The slow mode is traveling at around 5 m/s and the fast mode travels at about 25-45 m/s.

These speeds have an uncanny similarity to those of the Streamers, and because of this, the working assumption from this point on is that they are the same phenomena, unless shown otherwise. This allows the use of the simulation to diagnose the likely patterns and mechanisms underlying the streamer clouds, which is a proven method for understanding Titan's storms at a different season (Mitchell et al. 2011; see also Section 5.5.2).
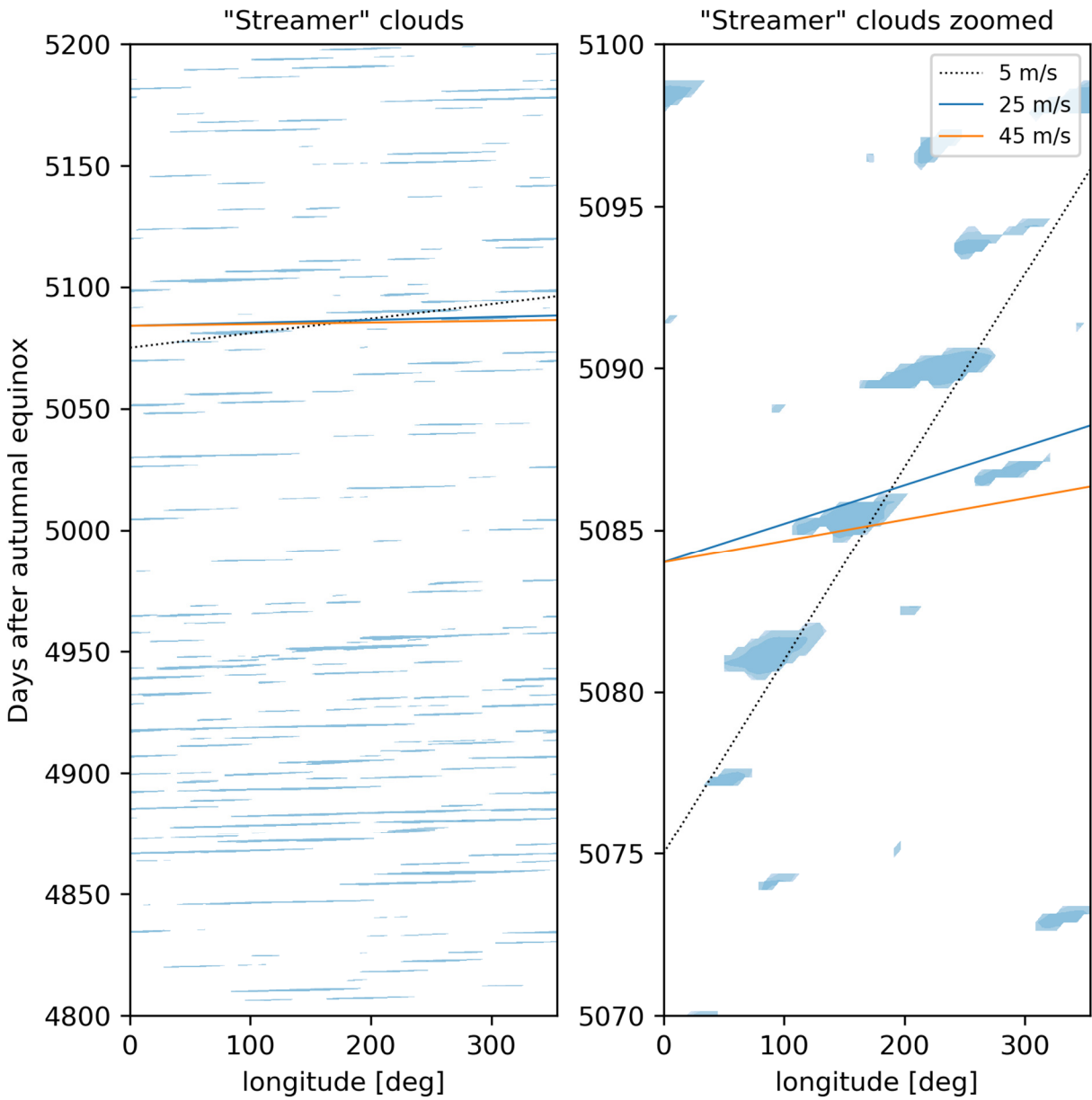
Figure 5.3. Hovmöller diagram of the logarithm of simulated precipitation averaged between 25°S-60°S latitude. Days 4800-5200 (left) and Days 5070-5100 (right) after the fall equinox.

The next task is to isolate the modes that contribute the most power to the variability in the simulated precipitation and wind field, and then use this information to isolate features in other fields that are associated with the dominant modes. Power spectra (dispersion relation) of surface-level zonal winds (Figure 5.4, left) and precipitation (Figure 5.4, right) over days 4800-

5200 and averaged from 25°S-60°S latitudes (i.e., the same as displayed in the left panel of Figure 5.3) reveal modes of variability with zonal wavenumbers 1-2 and travelling eastward between 25-45 m/s (blue and orange lines, respectively). Around these modes, there is an envelope of modes gathered along lower and higher wavenumbers and travelling with a fixed group speed of around 5 m/s (gray lines).
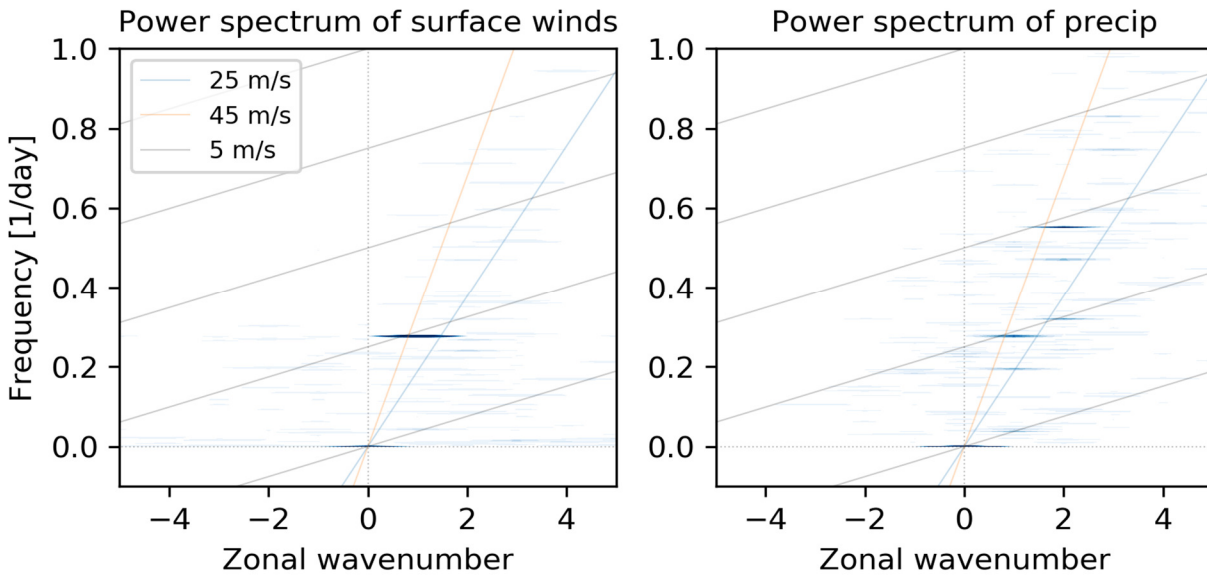
Figure 5.4. Power spectra of surface-level zonal winds (left) and precipitation (right) over days 4800-5200 and averaged from 25°S-60°S latitudes.

To further explore the structure of these modes, the data are filtered to isolate the surface pressure and winds in the regions of slow and fast modes, focusing on zonal-wavenumber 1. A "fast mode" is defined as the power peak in zonal surface winds at a frequency of ~0.3 per day. All power outside the range 0.2-0.4 per day and wavenumber 1 are zeroed out, and then the fields are inverse-Fourier transformed back to real space. This results in a full time-series of days 4800-5200 with only the fast mode; day 5085 is the focus of our analysis, i.e., where the lines are drawn

in Figure 5.3. Figure 5.5 shows the surface winds and pressure of the fast mode.
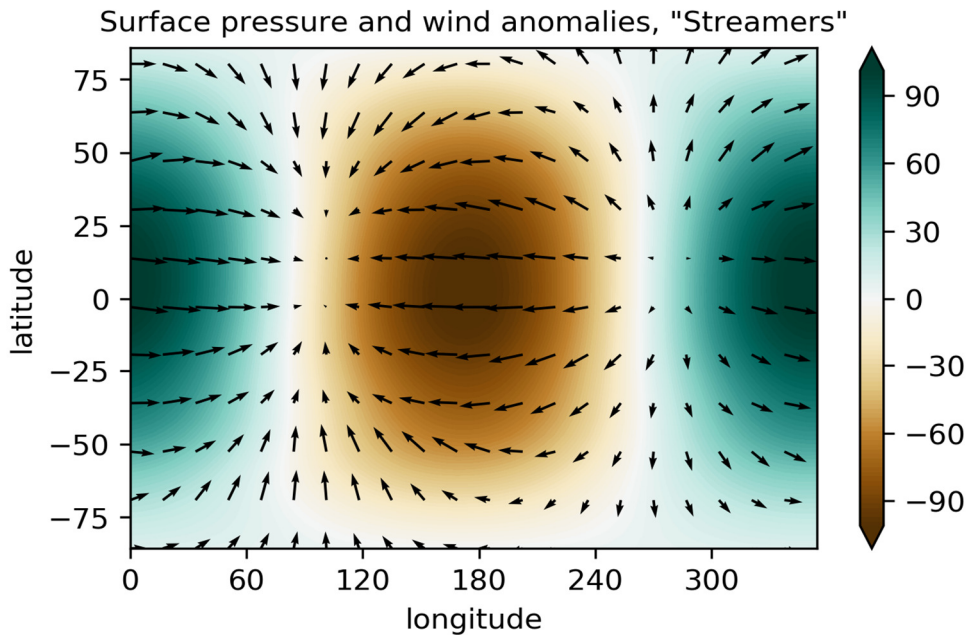
Figure 5.5. Fast mode - surface pressure (colors; blues positive, browns negative) and surface wind anomalies (arrows).

The patterns of surface pressure and winds reveal an equatorial-Kelvin-wave-like mode, which is global in extent because of Titan's weak rotation. Equatorial Kelvin wave dispersion curves trace out straight lines of constant phase speed, all of which pass through zero wavenumber and frequency. The precipitation power spectrum (Figure 5.4) also shows wave modes spread across wavenumbers 0-2 at constant phase speeds of 25-45 m/s. This lends confidence to the interpretation of the fast mode as a Kelvin wave.

The equatorial Kelvin wave propagates eastward (positive wavenumber) at the gravity wave phase speed, as is clearly shown in the power spectrum. The eastward propagation is also evident in the filtered wave mode (Figure 5.5), which shows surface winds converging eastward of the surface high pressure. The wind convergence draws mass into the atmospheric column ahead of the high pressure, thus drawing it to the east. Furthermore, the presence of surface

convergence gives this mode a direct connection to the model precipitation through the associated uplift and subsequent moist convection. This mode is present essentially at all times of the simulation (not shown) and thus plays a dominant role in shaping Titan's weather cycle.
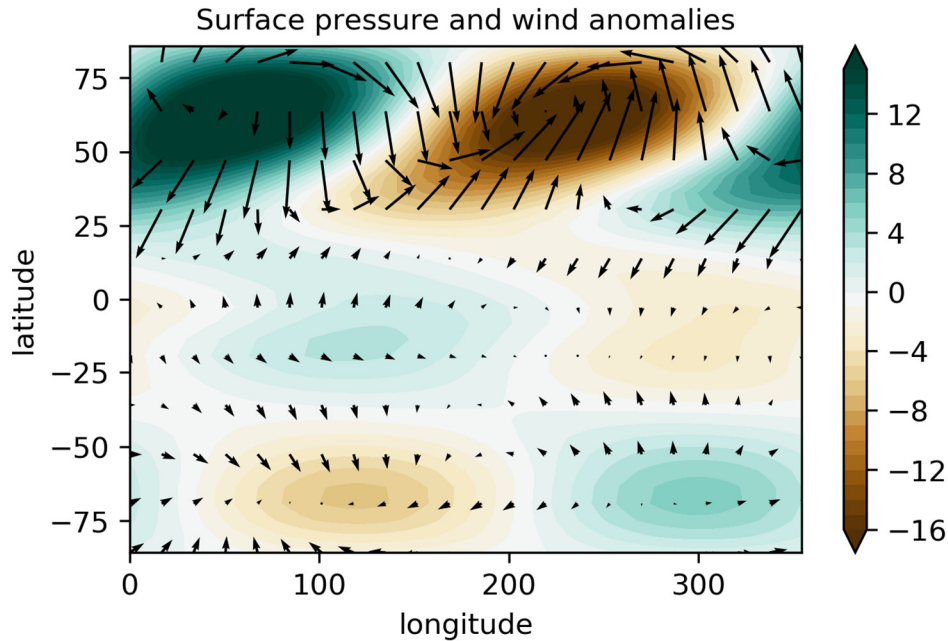
Figure 5.6. Slow mode - surface pressure (colors; blues positive, browns negative) and surface wind anomalies (arrows).

The slow mode has a frequency of ~0.05 per day at wavenumber 1 (Figure 5.4). Filtering the surface pressure and winds at wavenumber 1 and frequencies between 0.01-0.2 per day reveals a more complicated structure than that of the fast mode (Figure 5.6). Remarkably, the high *northern* latitudes have the strongest signal despite our focus on *southern* mid latitudes. There appears to be a global, coordinated response between Rossby waves at both poles and an unidentified equatorial mode. For this coordination to occur, all modes must of course have the same frequency, and at least for the high-latitude Rossby waves, which travel slowly relative to the mean flow. This would require significant eastward advection by the mean flow. Then

assuming their propagation is dominated by the zonal mean advection, $\bar{u}$, the frequency locking would be possible at any point where modes of the same wavenumber, k, have equal frequency given by the local zonal advection, $\omega \sim \bar{u} \times k$. For the slow mode and at wavenumber-1, this frequency is ~0.05 cycles per day. This frequency can be used as a guide to estimate the local steering levels of different latitude sections of the global, slow mode (Figure 5.6). In the left panel of Figure 5.7, the latitudinal cross-section of the 0.05 cycles per day steering level (magenta) is overplotted on the zonal variance of the zonal winds (contours). The northern-high-latitude Rossby wave appears to be steered by the 1300-mbar, zonal-mean zonal winds (Figure 5.7, right). The steering level bulges upward at the equator to ~600 mbar, then descends to ~800 mbar in southern mid latitudes, where the Streamers occur. An arc of moderate variance bridges between high variance at 450 mbar and at the surface, and this may indicate a vertical coupling, although more analysis would be required to confirm this. Other areas of high variance appear to be connected to the global mode as well, for instance 0°N-50°N latitudes and 700-1000 mbar.
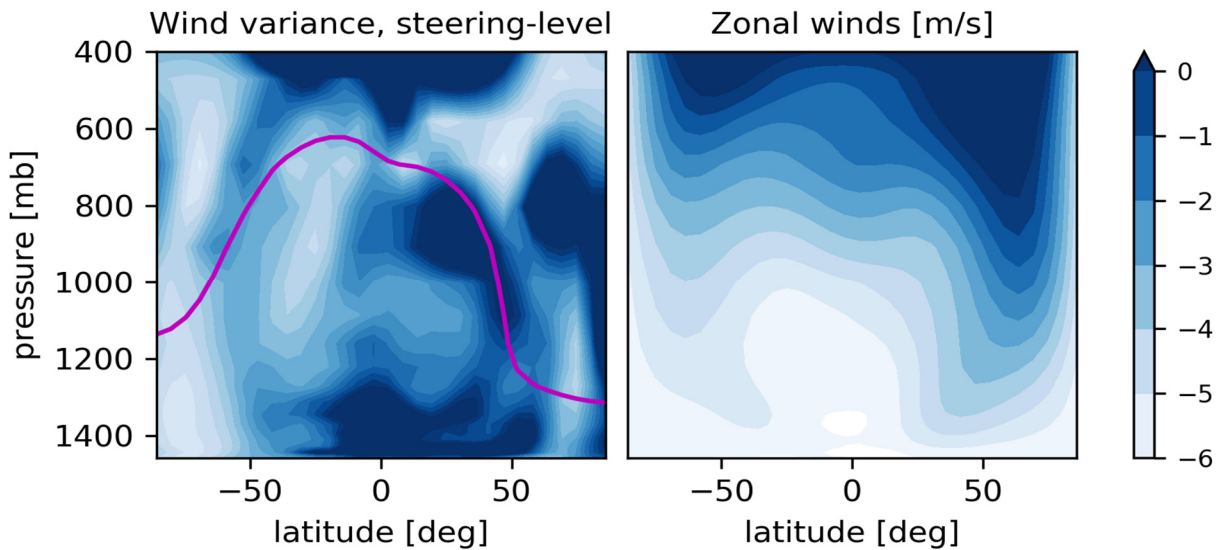
Figure 5.7. (Left) Zonal variance of zonal winds for the streamer event, day 5084 (colors), and the 0.05 cycles/day zonal-mean angular frequency for wavenumber-1 disturbances (magenta line). (Right) Zonal-mean zonal winds for the same day.

A consistent interpretation of Figure 5.7 is that multiple modes are coordinating over the entire globe of Titan and allowing inter-hemispheric influence of waves and storms. Further exploration of this coordination is beyond the scope of this study.

In summary, there are two dominant modes of precipitation variability in the TAM simulation between days 4800-5200, which roughly corresponds to the Streamer event observed by Cassini. The fast mode is equatorial-Kelvin-wave-like with a phase speed of ~25-45 m/s, and the slow mode is a global coordination of wavenumber-1 extratropical Rossby waves and an unidentified equatorial wave with frequencies of 0.05 cycles per day. Both the fast and slow modes are global in extent. Our interpretation is that these two modes interact constructively and destructively such that the fast mode travels at the free gravity wave phase speed while propagating through the wave packet envelope of the slow mode moving at a slow-eastward group speed.

Finally, the so-called "persistence" of the Streamers – that they fully circumnavigate Titan without dissipating – is readily produced in the simulation. Figure 5.3 clearly shows the slow mode circumnavigates ~15 times over 400 days. It may be that if storms last this long, they could be observed on many different Cassini flybys, and if so, it would be useful to perform a global spatio-temporal search for repeating cloud features.

5.4 The Role of Waves in the Results

In this part of the study, it is important to briefly lay out the role of waves in the GCM simulation results, to then revert back and focus on how to interpret the spatio-temporal observations of Titan's clouds.

As described in the previous section, two types of waves are found to be associated with the slow and fast modes of propagation for the Streamer event, Rossby and Equatorial-Kelvin-wave-like, respectively. The working hypothesis from both the observations and simulations is that the slow mode is a Rossby wave advected by the background zonal winds. On Earth, Rossby waves can propagate in the zonal and meridional directions and can instigate cloud activity by modifying the temperature structure of the atmosphere by inducing convergent flow near the surface. Rossby waves have been previously shown to match zonal and meridional group velocities consistent with velocities of Titan clouds from ground-based observations (Schaller et al., 2009). The presence of Rossby waves is certainly not unexpected since they seem to naturally arise and tend to drive weather in planets with atmospheres.

Planetary-scale Kelvin waves have also been found to arise naturally in previous simulations matching two large Titan cloud storm events observed by Cassini, during the same equinoctial season as the Streamers (Mitchell et al., 2011). The influence of an equatorially trapped mode on the mid- and high-latitude meteorology on Titan may seem odd, but it is not inconsistent with the dynamics. The resemblance of the fast mode surface pressure and surface winds from the simulations in Figure 5.5 to the historical equatorial wave theory depicting equatorial Kelvin waves on Earth, produced by Matsuno in 1966, is remarkable. Figure 5.8 is an adaptation of Figure 8 in Matsuno's 1966 paper - a plan view of pressure and velocity distributions for a wave that behaves like a Kelvin wave – where the waves are eastward propagating and have zonal velocities and geopotential perturbations that vary in latitude as Gaussian functions centered on the equator (Holton, 2004).

On an equatorial beta plane, where the latitude angle $\phi = 0$, the meridional velocity perturbation for equatorial Kelvin wave modes vanishes and the wave dispersion equation is
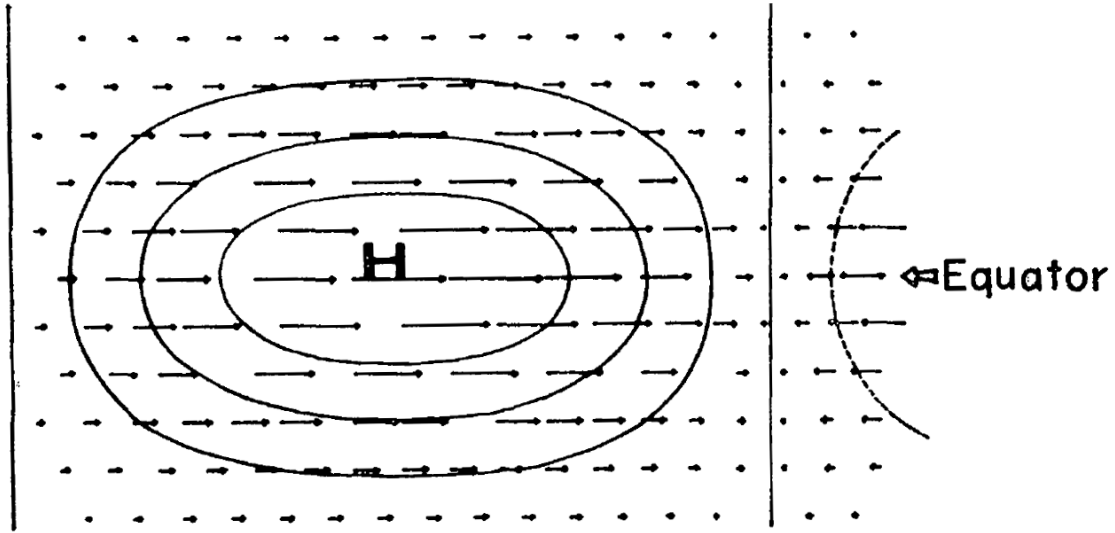
Figure 5.8: Pressure and velocity distributions, with height perturbations associated with a wave that behaves like an equatorial Kelvin wave. [Image credit: Matsuno et. al., 1966]

identical to that for ordinary shallow water gravity waves. Even in the absence of background

basic flow, non-planar effects cannot be neglected on slowly rotating and or small-sized planets

(Yamamoto, 2019), such as Titan.

Equatorial trapping is quite weak on Titan due to its slow rotation rate and small radius

(Mitchell & Vallis, 2010) and therefore the equatorial modes extend their influence over a much
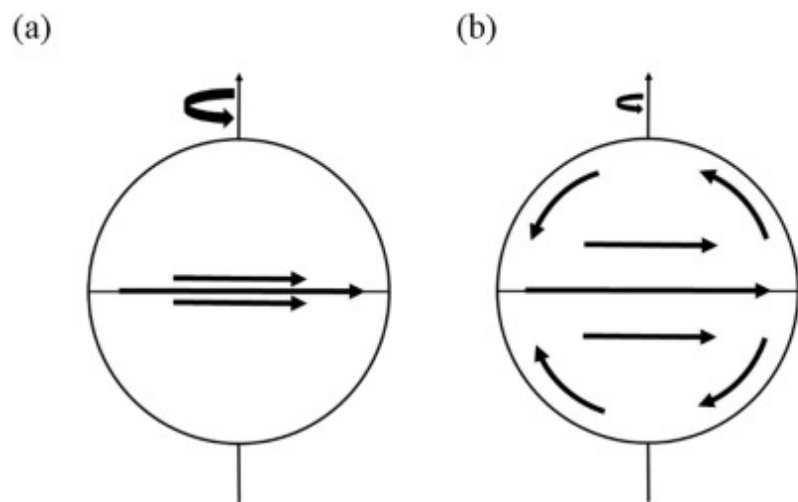
Figure 5.9: Flow patterns of equatorial Kelvin-like waves in the absence of background flows on fast rotating (a) and slowly rotating spheres [Image credit: Yamamoto, 2019].

broader expanse in latitude. Theory predicts that meridional circulation on Titan extends to the poles (Mitchell et al., 2006), and the energy of the equatorial Kelvin waves is not confined around the equator and reaches to middle latitudes (Yamamoto, 2019). In this case the Kelvin wave develops non-zero meridional velocity depicted schematically in Figure 5.9b and seen in the fast mode in Figure 5.5.

Furthermore, to stress the point of connection between equatorial Kelvin waves and the Streamers fast mode of propagation found in the simulations (Figure 5.5), a dispersion diagram for free equatorial waves adapted from Matsuno, 1966, by Holton, 2004 (Figure 5.10), is compared to the power spectrum from simulations in Figure 5.4. Both figures clearly show the Kelvin wave dependence of frequency on zonal wavenumber for eastward gravity modes in the same location.
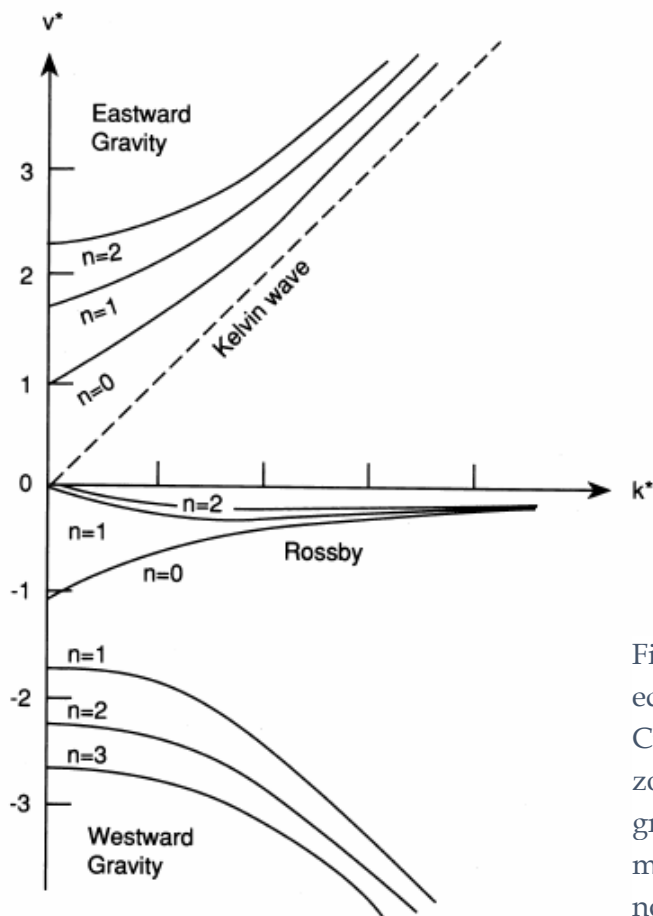
Figure 5.10: Dispersion diagram for free equatorial waves; borrowed from Holton, 2004. Curves show the dependence of frequency on zonal wavenumber for eastward and westward gravity modes well as for Rossby and Kelvin modes. Frequency and zonal wavenumbers are nondimensionalized.

The most interesting finding is the fact that equatorial Kelvin waves seem to drive the fast modes in subsequent simulation results, uncovered in Section 5.3, that match observations found in Figure 5.2 in the "region of interest".

5.5 Analysis of Other Cloud Events from the Region of Interest

In this section, the study refers back to the "region of interest", as delineated in Figure 5.2, and explores the connection with storms seen in the observational data after simulations provide pronounced events that match seasonally. Figure 5.11 shows superposed lines onto the shorter 6-day interval Hovmöller plot (Figure 5.2, right), with the timeline of seasonal changes in gray – with labels under the line for: southern summer solstice (SSS) ~2500 day; northern spring equinox
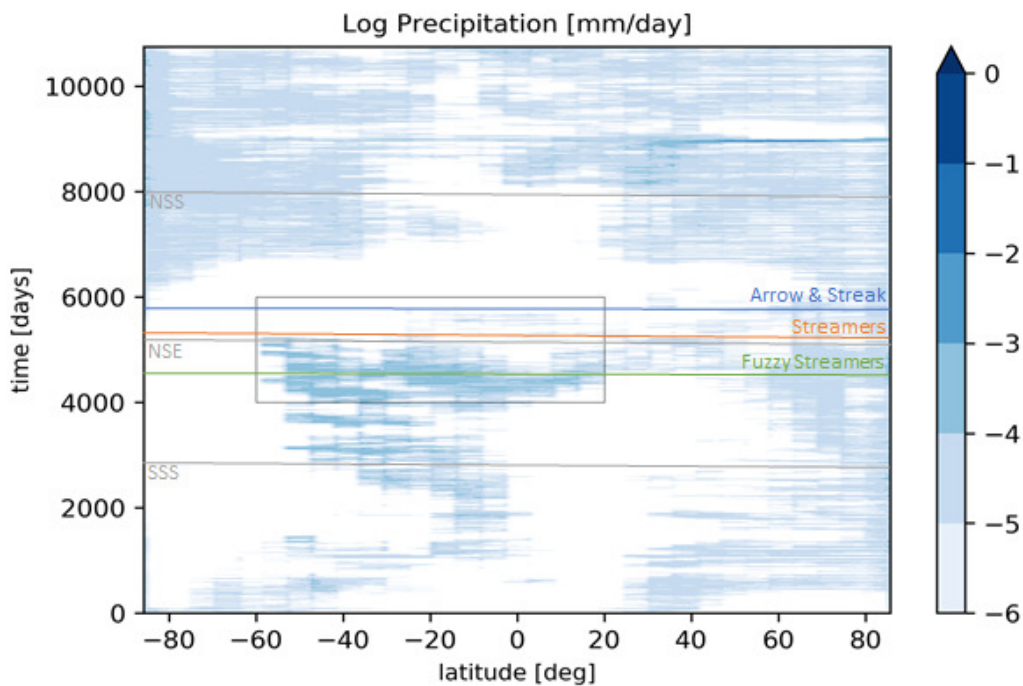
Figure 5.11. Same as the right panel for 6-hourly intervals in figure 5.2. Lines with timeline of four observed storm events (green – Fuzzy Streamers; orange – Streamers; and blue – Arrow and Streak) as well as season changes from SSS to NSS (in gray).

(NSE) at day ~5000 and northern summer solstice (NSS) at ~8000 days – as well as color coded lines depicting the times for four cloud storms found in the observational data, including the Streamers (in orange).

The three other cloud events will be analyzed in this section as follows. First, in Section 5.5.1, the event labeled "Fuzzy Streamers" in Figure 5.11 (in green) is presented. This event is a prominent storm from which temporally resolved observations allow for the production of spatio-temporal plots, similarly to that of the Streamers from Chapter 4. Next, Section 5.5.2 consists of two events labeled "Arrow and Streak" in Figure 5.11 (in blue), and they are presented together because of their closeness in time (September and October, 2010). The Arrow and Streak are the same events from the Mitchell et al., 2011, study and although the observations of these two events do not produce spatio-temporal plots, the simulations indicate that the events are influenced by the same dynamics as the first two events presented in this study, which is in agreement with the analysis in Mitchell et al., 2011.

5.5.1 Fuzzy Streamers Event: Observation and Simulation Analysis

Another predominant example of a mid-latitude clouds system, nick-named "Fuzzy Streamers" because of its resemblance in shape and location to the Streamers, was captured by the ISS cameras on May 13, 2007, for a span of ~8 hours. Although visible in the images for the aforementioned time span, the observational data to produce cloud enhanced images only encompass half that time (~4 hours). Figure 5.12 shows a sample from images used for this analysis to get "before" (raw image) and "after" (mapped image) views pinpointing the location of the clouds in a simple cylindrical map of latitude and longitude. Next, we see a sample view of the steps from the resultant calibrated and mapped image (left) to enhanced the cloud map

view (right), after the haze removal step has been done using the middle image, in Figure 5.13. This sample view also offers a zoomed-in display of the latitude and longitude areas surrounding the clouds, which will lead to the production of brightness plots and spatio-temporal plots as clouds propagate in the sequence of chosen images.
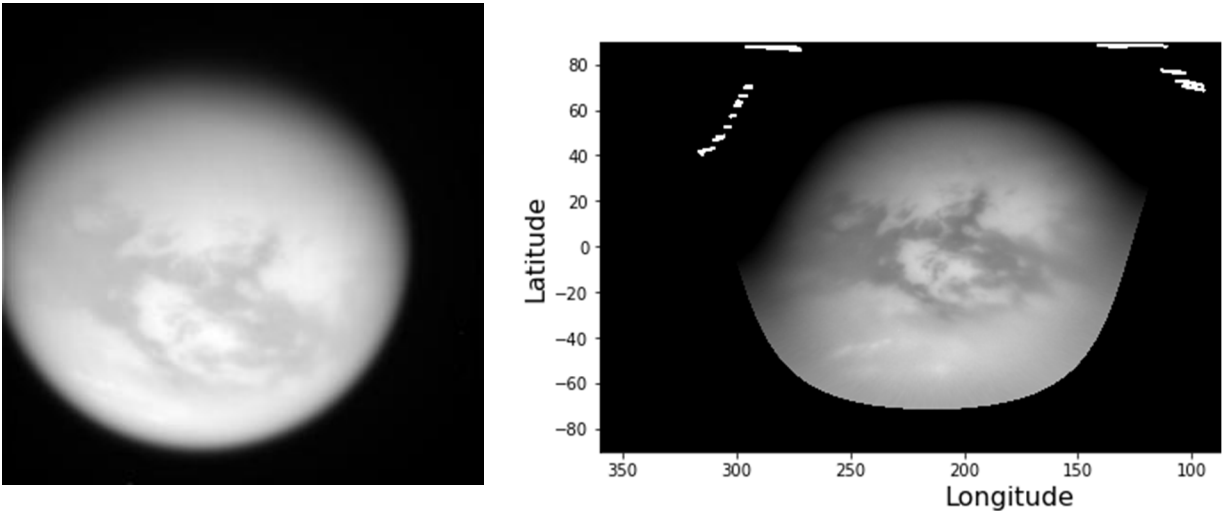
Figure 5.12. (Left) CB3/CL2 Raw image of a cloud event found on May 13, 2007; (Right) same as left image after calibration and mapping. Clouds are seen in the similar latitudinal location as the Streamers set.

For the analysis of this event, 89 processed maps from 27 image sets are selected. Each image time is separated by a few minutes within the set, and the total time span of all the sets (from beginning to end) is ~4 hours. The sets contain 3-4 images – each of the first 2 or 3 have views of the clouds while the last one is an image of the haze, which will be used for the cloud enhancement. The filter combinations, respectively, are: CL2/CB3 (visible 611 nm/near-infrared 938 nm) and either CL1/MT2 (visible 611/727 nm) or CL1/IR1 (visible 611 nm/near infrared 752 nm) chosen for haze removal – similar to, although not as effective for haze removal as, the CL1/MT1 (visible 611 nm/visible 619 nm) filter combination provided for the Streamers.
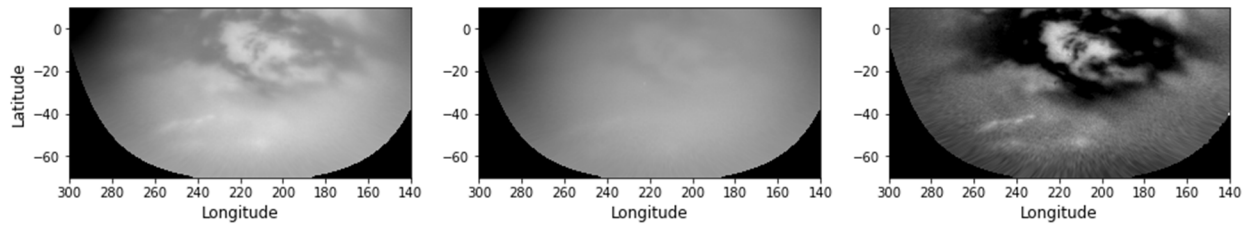
Figure 5.13. (Left) CB3 / CL2 mapped image; (Middle) CL2 / MT2 image of haze; (Right) resultant image of enhanced clouds.

The next step of the analysis involves the selection of enhanced cloud image maps with enough resolution to highlight the cloud propagation features and make brightness plots from which a Hovmöller diagram will be produced. Figure 5.14 displays a sample of seven enhanced cloud maps placed in time sequence to produce seven plots of brightness as functions of longitudinal location. This is a smaller set from the 35 images that are used to build the Hovmöller diagram seen in Figure 5.15.
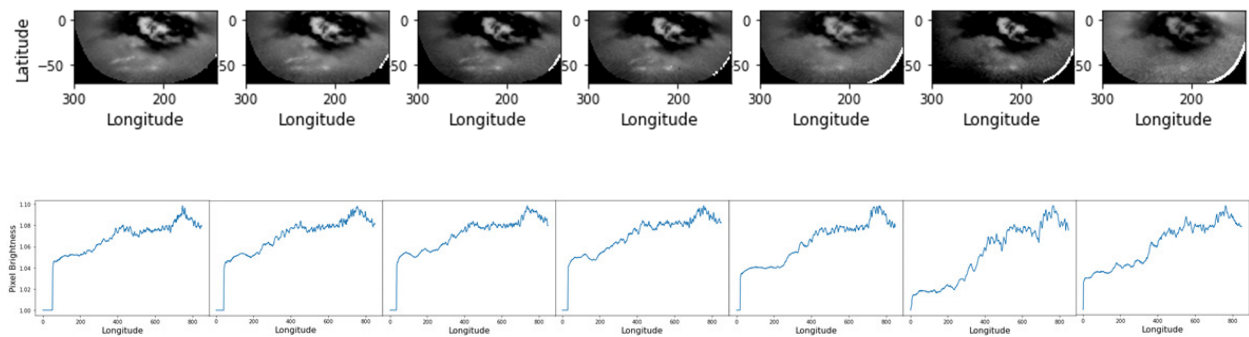
Figure 5.14. TOP: 7 resultant images of enhanced clouds after mapping and haze removal. BOTTOM: pixel brightness plots vs. longitude of the highlighted region on the top images. This is a smaller set shown as an example from the 35 images that make up the Hovmöller diagram shown in Figure 5.15.

After obtaining a change in longitudinal position as a function of time (in degrees per hour), just as it was done for the Streamers event, the values are translated to find the speed of

propagation of the clouds using the known radius of Titan, R_{Titan} = 2572 km, to determine the distance in meters per degree on the moon, and with a simple time unit conversion, the values obtained are between 2.5±1 m/s to 6.2±1 m/s, which is strikingly close to the slow eastward propagating speeds found for the Streamers. Due to the limited image timeframe for this event, the second fast speed is not measurable.
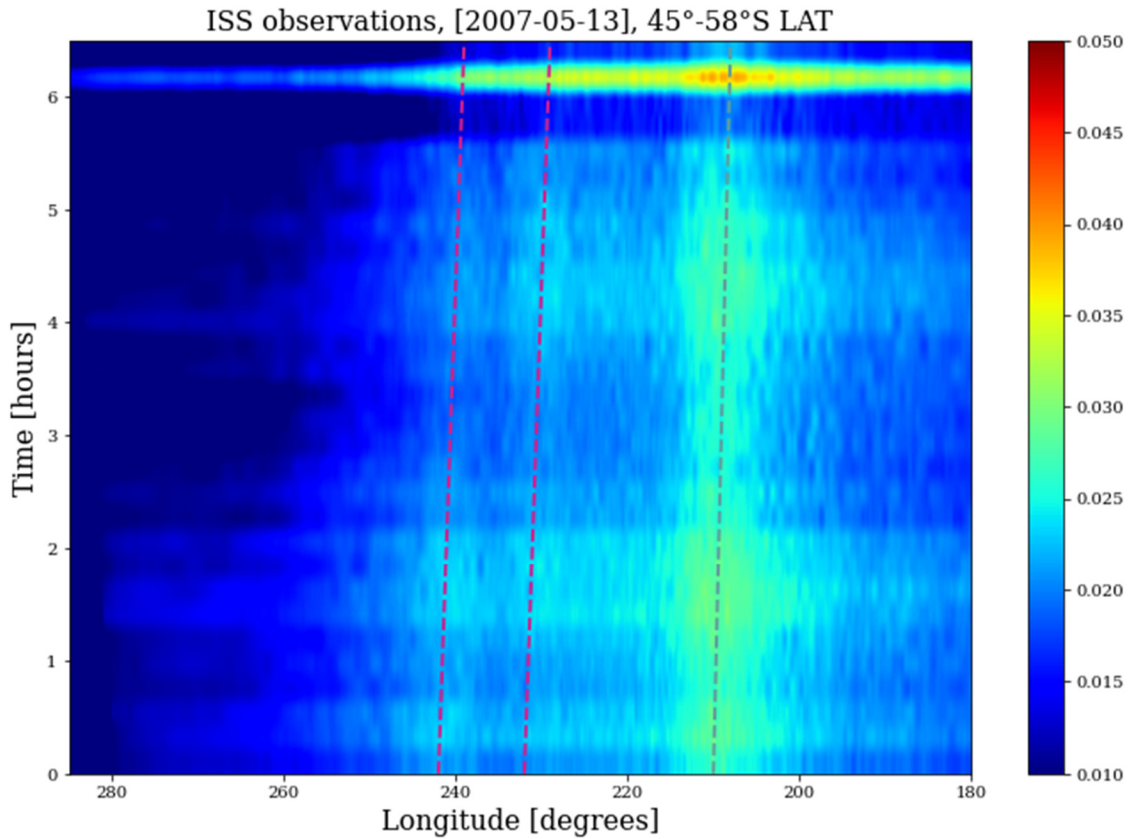
Figure 5.15. Hovmöller diagram of 35 consecutive cloud image brightness plots (~6.5-hour interval), highlighting the role of the waves and how the clouds propagate across the moon between 45° and 60° of latitude, south. Brightness increases from blue to red. Dotted lines are slopes plotted to aid in the calculations of the average speed at which the clouds move longitudinally against the surface background.

The observational results are now compared to simulations in the same way as was done for our main cloud event, the Streamers, starting with Figure 5.16, a 10-daily simulation output (left) with 6-hourly data (right) that shows the distinct precipitation features in the Southern Hemispheres around the latitude of the Fuzzy Streamers (25°S-60°S).
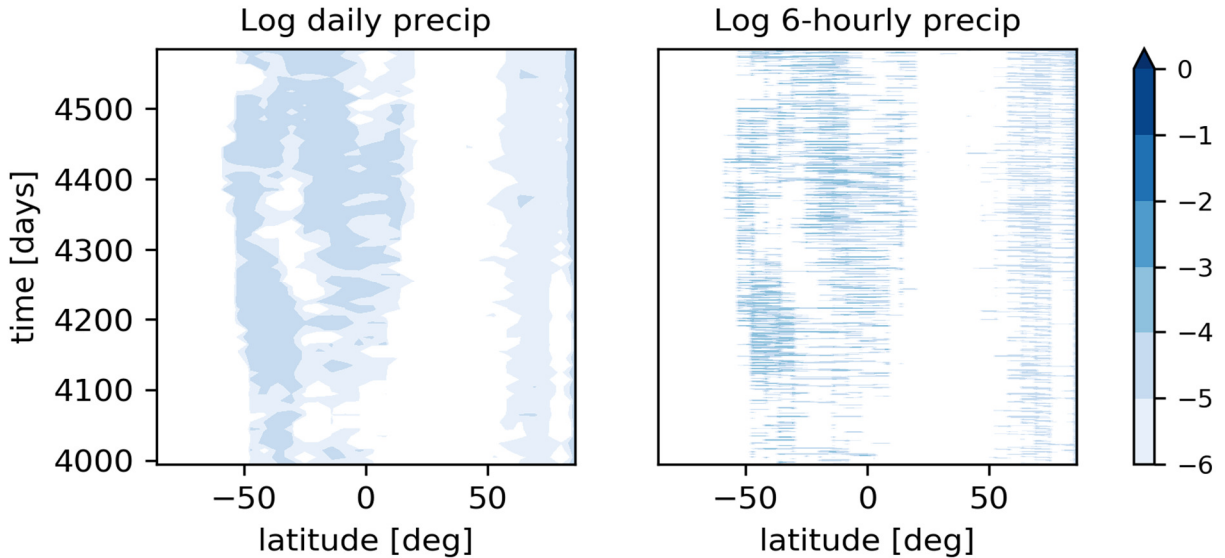
Figure 5.16. (Left) Zonal-mean precipitation (mm/day) simulation with data averaged over 10-day intervals. (Right) Same as the left panel for 6-hourly intervals.

The Fuzzy Streamers clouds occur on May 13, 2007, ~4200 days after fall equinox; therefore, we now focus our analysis between days 4000 and 4600. The Hovmöller diagram of the logarithm of 6-hourly precipitation averaged in latitude from 25°S-60°S during days 4000-4600 shows two eastward-propagating signals (Fig. 5.17). A slow-eastward mode with zonal-wavenumber 1 and a fast-eastward mode with a zonal wavenumber of ~1- 2. The slow mode is traveling at around 5 m/s and the fast mode is about 25-45 m/s.

Once again it is found that the eastward speed of the simulated slow mode closely

matches that of the cloud observations. From this correspondence between observed and simulated slow modes, it is reasonable to infer that the fast mode would have also been observed if the Cassini images had allowed.
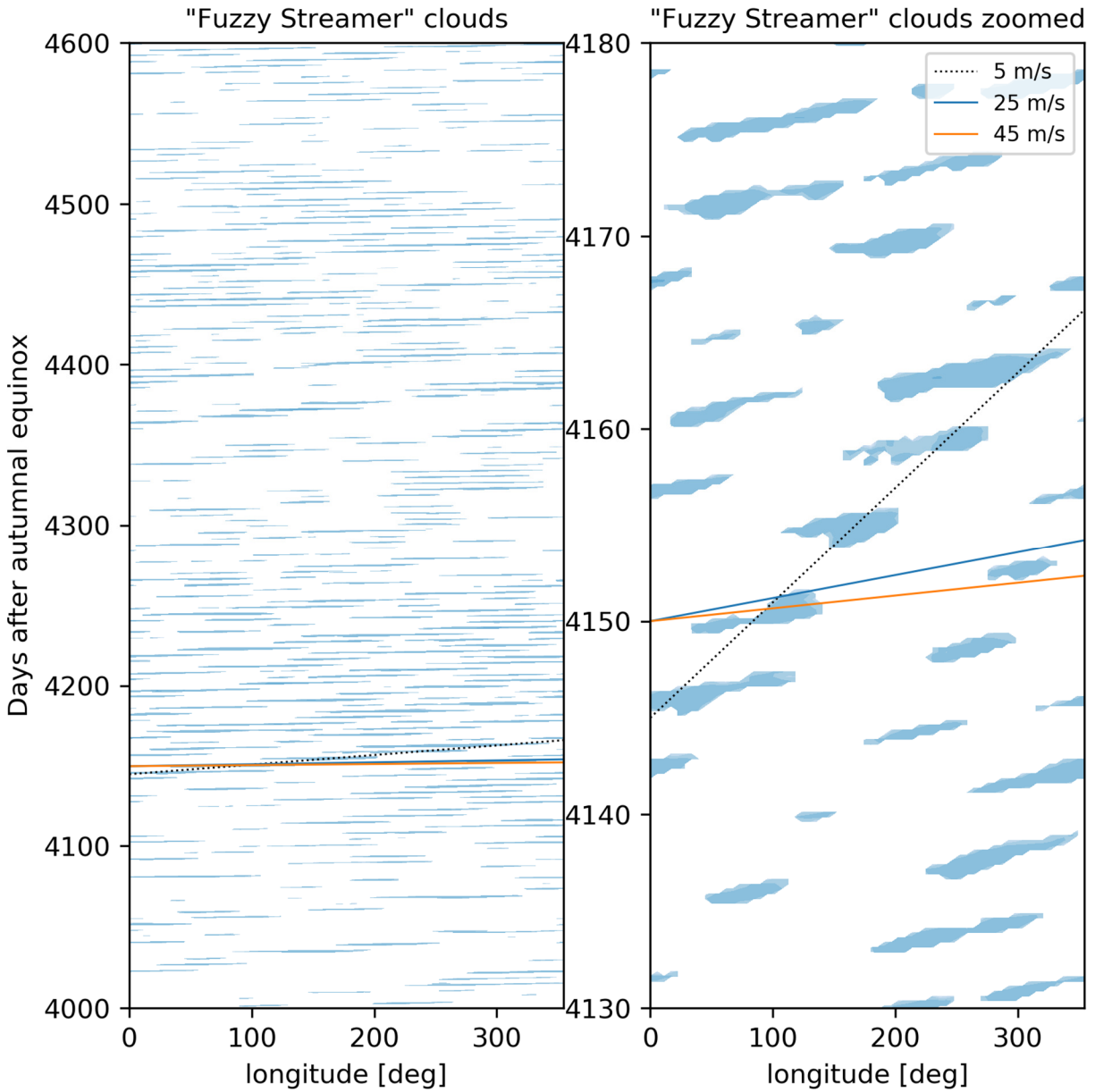
Figure 5.17. Hovmöller diagram of the logarithm of simulated precipitation averaged between 25°S-60°S latitudes. Days 4000-4600 (left) and Days 4130-4180 (right) after the fall equinox.

Power spectra of surface-level zonal winds (Figure 5.18, left) and precipitation (Figure 5.18, right) over days 4000-4600 and averaged from 25°S-60°S latitudes reveal modes of variability with zonal wavenumbers 1-2 and travelling eastward between 25-45 m/s (blue and orange lines, respectively). Around these modes, there is an envelope of modes gathered along lower and higher wavenumbers and travelling around 5 m/s (gray lines). This spectral structure closely resembles that of the simulated Streamers (Figure 5.4).
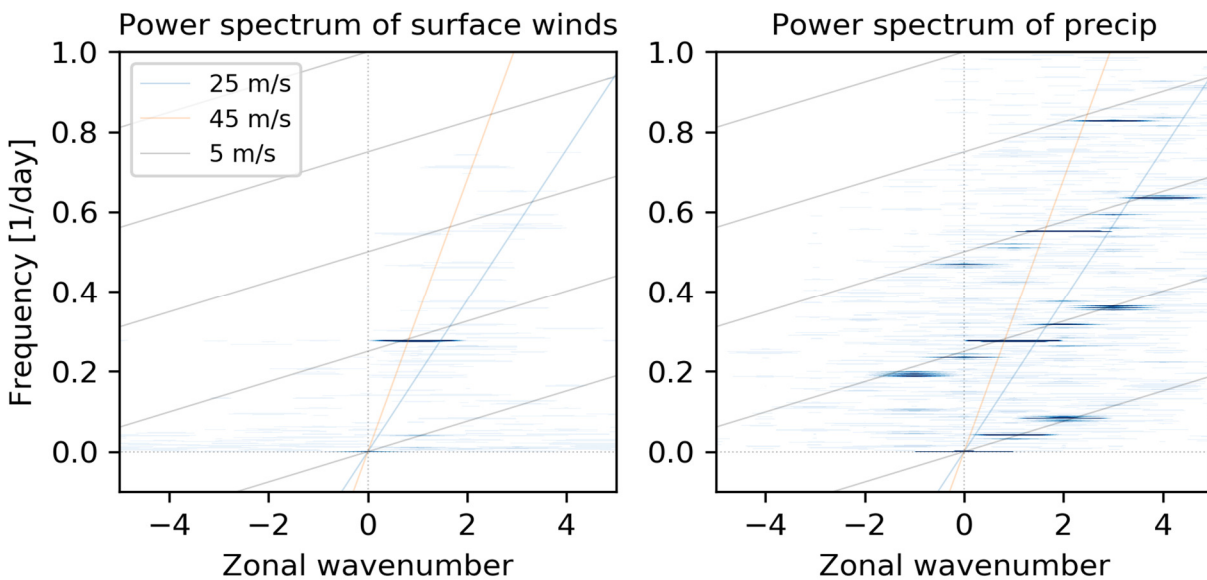
Figure 5.18. Power spectra of surface-level zonal winds (left) and precipitation (right) over days 4000-4600 and averaged from 25°S-60°S latitudes.

A full time-series of days 4000-4600 with only the fast mode, focusing on day 4150, shows the surface winds and pressure of this mode in Figure 5.19. Just as it was found to be true for the Streamers, the patterns of surface pressure and winds reveal an equatorial-Kelvin-wave-like mode, which is global in extent because of Titan's weak rotation. The equatorial Kelvin wave propagates eastward (positive wavenumber) at the gravity wave phase speed, as is clearly shown in the power spectrum. It is noteworthy that the Kelvin-like mode is present in the simulation

during both the Streamers and Fuzzy Streamers, which are separated by hundreds of days. This mode is essentially always present in the simulation (not shown) and provides a "heartbeat" that is predicted to be present in all cloud/storm systems on Titan.
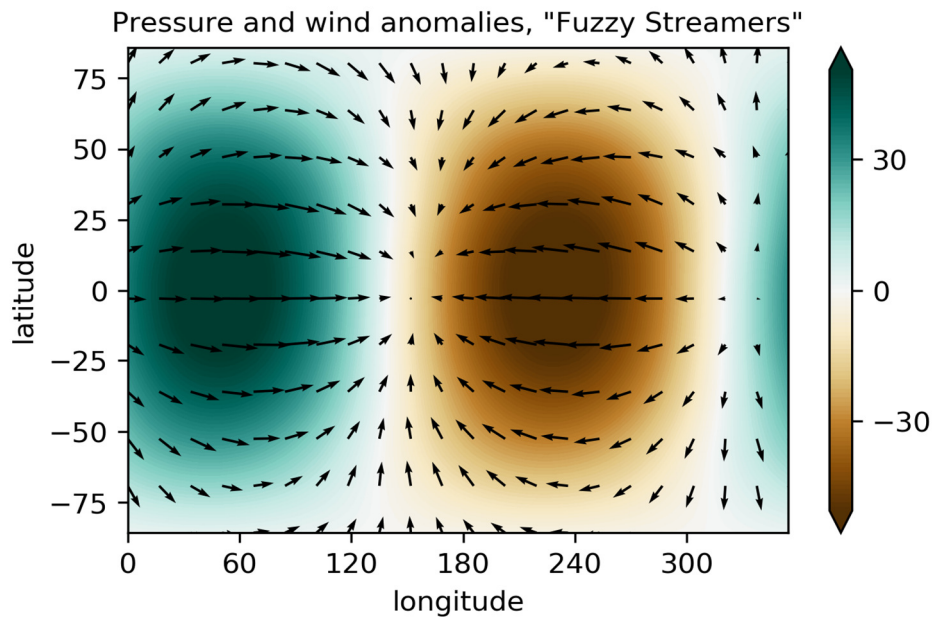
Figure 5.19. Fast mode - surface pressure (colors; blues positive, browns negative) and surface wind anomalies (arrows).

The slow mode of the Fuzzy Streamers has a frequency of ~0.05 per day at wavenumber 1 (Figure 5.18). Filtering the surface pressure and winds at wavenumber 1 and frequencies between 0.01-0.2 per day reveals a more complicated structure than that of the fast mode (Figure 5.19). There is a resemblance between the slow modes of the Streamers (Figure 5.6) and the Fuzzy Streamers (Figure 5.20), particularly in the high-amplitude Rossby wave pattern at high northern latitudes, a distinct equatorial mode, and a weak mode in southern latitudes. The slow mode involves a globally coordinated response by zonal-mean advection (not shown), just as it did for the Streamers (Figure 5.7).
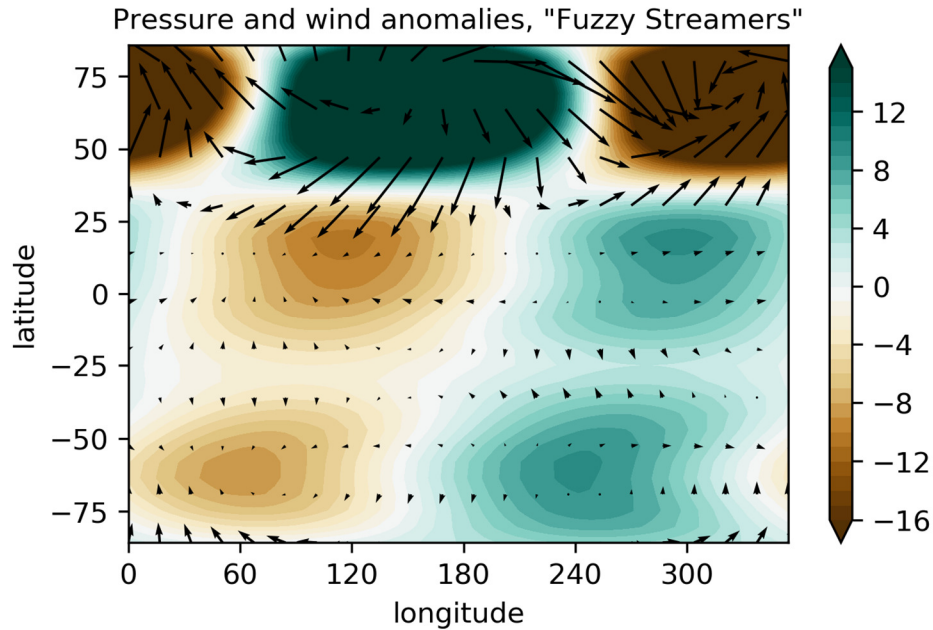
Figure 5.20. Slow mode - surface pressure (colors; blues positive, browns negative) and surface wind anomalies (arrows).

5.5.2 Arrow and Streak

Finally, to make contact with the motivating works of Mitchell et al. (2011) and Turtle et al. (2011), we return to the "Arrow" and "Streak" events that occurred just after spring equinox on Titan. Processed and enhanced images of a sequence of three Arrow images (Figure 5.21), though revealing a remarkable geometric structure, are nonetheless too closely spaced in time to allow determination of their speed of propagation. Given the spatial resolution and temporal spacing, we can infer an upper bound on its speed of ~100-200 m/s, however this does not likely rule out any mode, fast or slow.

Processed and enhanced images of a sequence of three Streak images (Figure 5.22) again reveal a remarkable geometric structure coordinated over large latitude spans, but again are too closely spaced in time to allow determination of their speed of propagation. Mitchell et al. (2011)
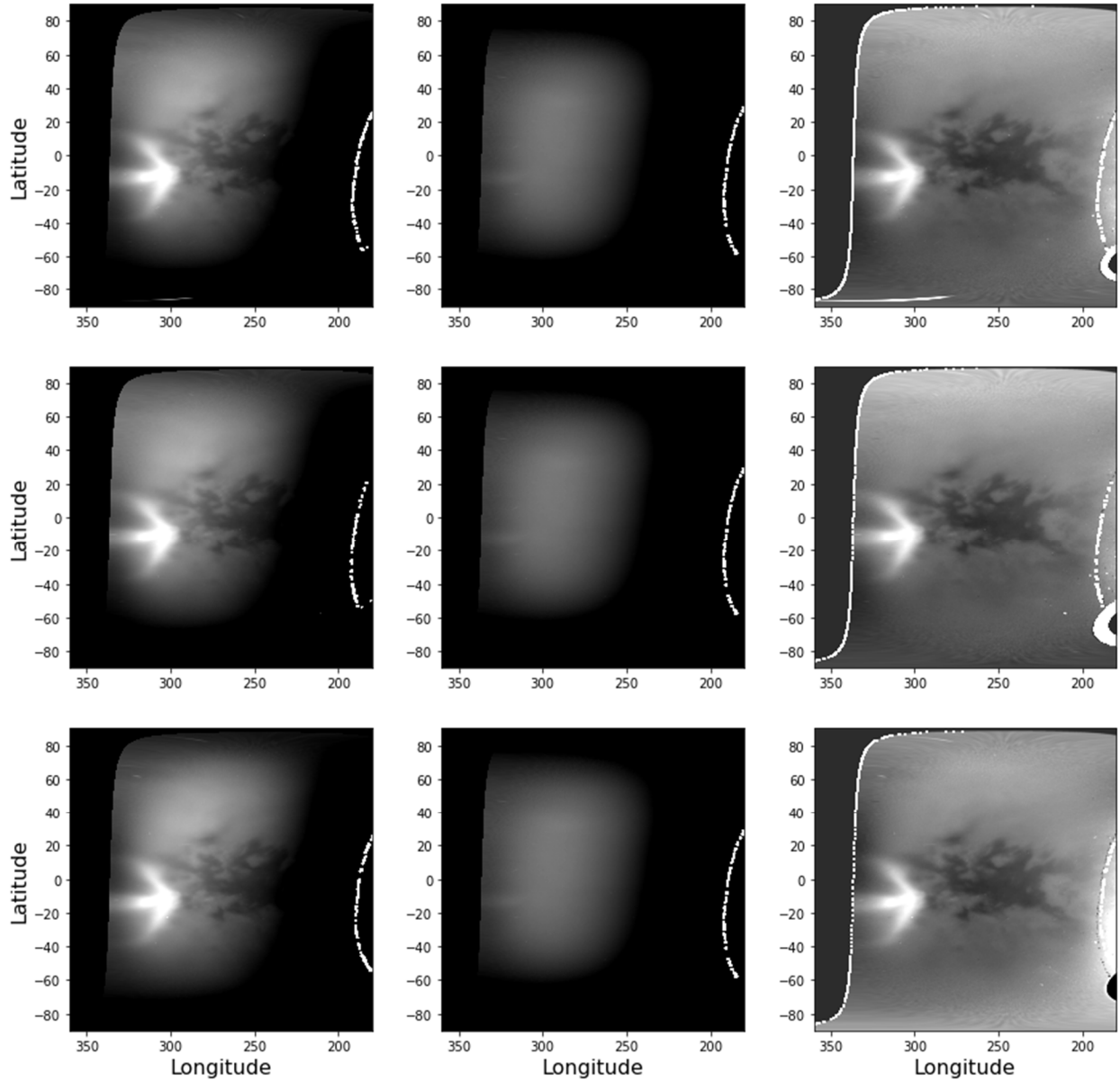
Figure 5.21. As in Figure 5.13 for three sequential images of the "Arrow" event.

compared these two events to leading modes of precipitation in an earlier version of the Titan climate model with a more idealized configuration. Similarly to the TAM simulations, a fast and slow mode dominate the simulation during the season of these observations. The fast mode is identified as an equatorial Kelvin wave, and the slow mode is a Rossby wave with surface fronts.
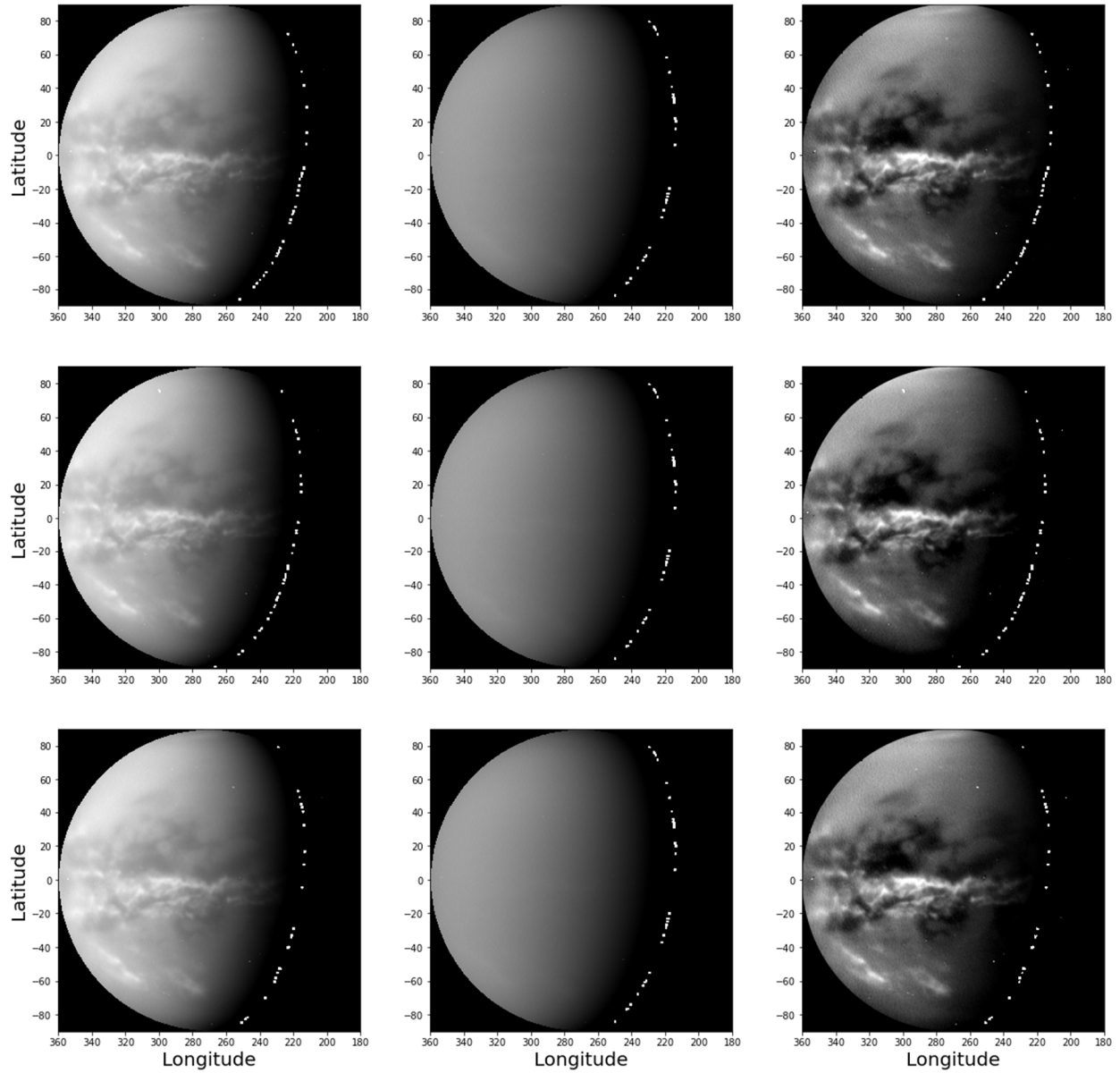
Figure 5.22. As in Figure 5.13 for three sequential images of the "Streak" event.

Figures 5.23 and 5.24 show the fast and slow modes during the "Arrow and Streak" epoch of the TAM simulation, which again are equatorial-Kelvin-like and (coordinated) Rossby-like, respectively. Although slightly different in detail, the modes identified in Mitchell et al. (2011) bear strong resemblance to the fast and slow modes found in TAM.
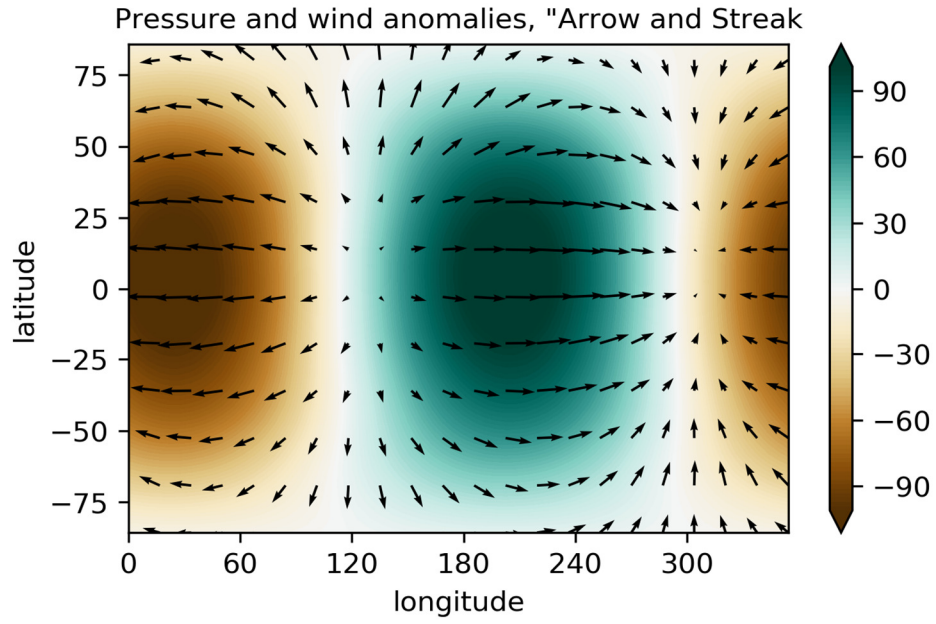
Figure 5.23. As in Figure 5.5 for the "Arrow and Streak" epoch of the TAM simulation.
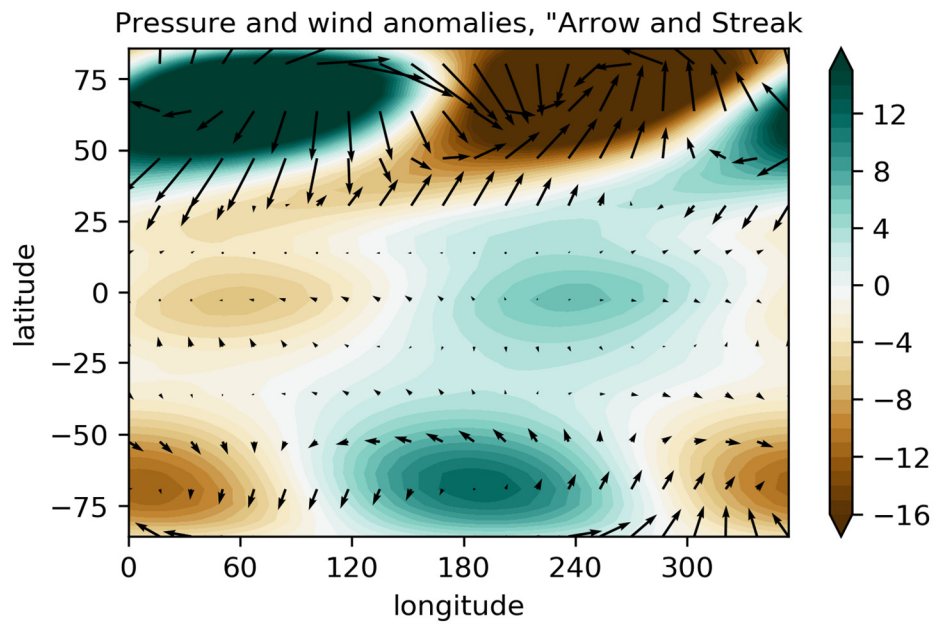
Figure 5.24. As in Figure 5.6 for the "Arrow and Streak" epoch of the TAM simulation.

5.6 Summary

Cassini cloud observations reveal the spatial, and in some cases temporal, distribution of Titan's storms, but they do not tell us directly about storm dynamics – how they form, propagate, etc. Comparing a TAM simulation of Titan's climate to the observed Streamer event revealed both a fast Kelvin-like and a slow Rossby-like mode dominating precipitation and surface wind variability. The two modes coordinate during the Streamer epoch to produce fast-eastward squall lines propagating through a slow-eastward wave packet. The fast mode is essentially always present in the simulation, providing a "heartbeat" to otherwise slowly evolving storms that may persist and persevere for weeks to years. It may be that if storms last this long, they could be observed on many different Cassini flybys, and if so, it would be useful to perform a global spatio-temporal search for repeating cloud features. Similar analysis could be done with monitoring of Titan with ground-based or Earth-orbiting telescopes. The slow mode is a global coordination of three modes separated in latitude, and their common steering level diagnosed in the simulation could reveal novel dynamics of inter-hemispheric interactions.

This methodology applied to two other cloud events – the "Fuzzy Streamers" and the "Arrow and Streak" – suggest the fast and slow modes observed and simulated during the Streamer event are likely to have primary control over the spatio-temporal distributions of Titan's clouds. This is a promising methodology going forward with studies of Titan's meteorology that could be extended, for instance, to ground-based (Schaller et al., 2009) or space-based (Dragonfly) observations of Titan's clouds/storms.

CHAPTER 6

Conclusion and Future Work

Conclusion

Titan exhibits sporadic outbursts of methane clouds that extend hundreds to thousands of kilometers across the globe. The spatial and seasonal distribution of these storms have been a subject of study since their discovery; however the evolution of individual storms has received somewhat less attention. Even though clouds have been observed for many years now, it is still challenging to time the beginning and end of a cloud storm because it is so difficult to observe an entire storm from the moment it forms until it dissipates. The goal of this work has been to study methane clouds on Titan using an incredible set of images that the Cassini space probe has provided since its Saturn orbit insertion in 2004. In particular, this dissertation: 1) imagines the process of methane cloud droplet formation, 2) explores new Cassini image processing techniques to investigate cloud formation, evolution and propagation, and 3) constrains the physical mechanisms affecting the behavior of the storms under Titan's atmospheric conditions.

A particular set of Cassini observations taken in sequence during a Titan flyby give unprecedented spatio-temporal resolution to a cloud event referred to as the "Streamers". Remarkably, two distinct traveling signals appear in the observations: a fast-eastward mode and a slow-eastward mode. The fast-eastward signals appear to propagate within the envelope of the slow-eastward mode. However, Cassini cloud observations alone reveal little about the underlying storm dynamics – *how* they form, propagate, evolve, etc. To learn more, a simulation of Titan's climate is compared to the Streamer event. Fast- and slow-

eastward propagating signals observed during the Streamer event closely match those of simulated storms at the same season as the observations.

Further analysis of the simulated Streamer-like storms reveals that two distinct types of waves are associated with the slow and fast modes of propagation for all the cloud events: Rossby and Equatorial-Kelvin-wave-like, respectively. The working hypothesis based on both the observations and simulations is that the slow mode is a globally coordinated collection of Rossby waves with frequency matching facilitated by advection due to the background zonal winds. The fast mode is equatorial-Kelvin-wave-like, and since equatorial trapping is quite weak due to Titan's weak rotation rate and small radius, the equatorial modes extend their influence over a much broader expanse in latitude. Both the fast and slow modes are global in extent. Spectral analysis suggests the Kelvin-like waves with fast phase speeds are modulated by the Rossby-like wave packet with slow group speeds advected by the mean wind. The fast mode is present throughout the simulated year, giving a persistent "heartbeat" to the simulated storms, and this signal could perhaps be found in other observational data.

The simulation is then used to uncover the dynamics of three other observed cloud events with dates just before and after the Streamer event. In all of these cases, fast-Kelvin-like waves and slow-Rossby-like waves are likely to be responsible for their formation. There are important implications of this dynamical interpretation. First of all, equatorially trapped modes appear to have a significant influence on Titan's mid-latitude weather. Perhaps one could have predicted this, as it was already seen in another cloud analysis (Mitchell et al., 2011). But it's often the case that mid-latitude cloud activity observed on Titan is attributed to the seasonal migration of the Inter-Tropical Convergence Zone (ITCZ). At least in the summer mid latitudes just following solstice, simulations of Streamer-like events suggest that planetary-scale wave dynamics can be

the dominant contributor to local weather. It stands to reason that our methodology can be applied to other regions and at other times, and significantly, the fast-Kelvin wave is predicted to be a persistent signal at other seasons and in other locations.

Future Work

There are many more Cassini images that have been processed, but are still in need of analysis in the context of the simulations, and so applying the full methodology for understanding storm dynamics would be straightforward in follow-on work. For instance, the fast-Kelvin-like mode persists throughout the simulated year, imprinting a periodic signal on any storm that forms, and this could be tested with other spatio-temporally resolved cloud observations. Also, the slow-Rossby-like mode, being globally coordinated, could conceivably cause inter-hemispheric coordination of storms/clouds that may be observable. There are surely many more possibilities, both known and unknown, hiding in the Cassini survey of Titan's clouds.

Appendix A

Sample of image reduction steps applied to the image and label files (IMG and LBL) of one raw

ISS image obtained from the PDS site:

```
$ source atlas_wget_script-1image.bat
$ ciss2isis from=img_number.LBL to= img_number.cub
$ spiceinit from=img_number.cub
$ cisscal from=img_number.cub to= img_number_cal.cub
$ cam2map from= img_number_cal.cub to= img_number_map.cub
$ isis2fits from= img_number_map.cub to= img_number_map.fits
```

Generally, for the mapping step, a template text file with instructions (as the one below)

to reset any default parameters is created:

```
Group = Mapping
  ProjectionName     = SimpleCylindrical
  CenterLongitude    = 180.0
  TargetName         = Titan
  EquatorialRadius   = 2575000.0 <meters>
  PolarRadius        = 2575000.0 <meters>
  LatitudeType       = Planetocentric
  LongitudeDirection = PositiveEast
  LongitudeDomain    = 180
  MinimumLatitude    = -90.0
  MaximumLatitude    = 90.0
  MinimumLongitude   = 0.0
  MaximumLongitude   = 360.0
  Scale              = 10.0 <pixels/degree>
 End_Group
```

The text file name (e.g., map.txt) is added to the cam2map command line:

```
$ cam2map from= img_number_cal.cub map=map.txt to= img_number_scylindrical_map.cub
```

When a large sample of images are to be processed together, which is the case through most of

our study, we produce batch files that run all previous steps, including the mapping with the

same parameters for all images in the set. More information is found in the posted "cookbook"

in the TPACE research group site: https://dept.atmos.ucla.edu/jonmitch.

References

Ádámkovics, M., Wong, M., Laver, C. & de Pater, I. Widespread morning drizzle on Titan. Science 318, 962–965 (2007).

Barth, E. L. & Toon, O. B. Microphysical modeling of ethane ice clouds in titan's atmosphere. Icarus 162, 94–113 (2003).

Barth, E. L. & Toon, O. B. Properties of methane clouds on Titan: Results from microphysical modeling. Geophys. Rev. Lett., 31 (2004) L17S07

Barth, E. & Toon, B. O. Methane, ethane, and mixed clouds in Titan's atmosphere: Properties derived from microphysical modeling. Icarus 182, 230–250 (2006).

Bird, M. K., *et al.* The vertical profile of winds on Titan, Nature, 438, 800–802 *(2005).*

Brown, Robert, Jean Pierre Lebreton, and Hunter Waite, eds. *Titan from Cassini-Huygens.* Springer Science & Business Media, 2009.

Burr, Devon M., et al. "Fluvial features on Titan: Insights from morphology and modeling." *Bulletin* 125.3-4 (2013): 299-321.

Coustenis, Athena, and Fredric William Taylor. *Titan: exploring an earthlike world.* Vol. 4. World Scientific, 2008.

Faulk, Sean P., et al. "Titan's climate patterns and surface methane distribution due to the coupling of land hydrology and atmosphere." *Nature Astronomy* 4.4 (2020): 390-398.

Fletcher, N. H. Size Effect in Heterogeneous Nucleation. J. Chem. Phys., 572 (1958).

Fletcher, Neville H. *The physics of rainclouds/NH Fletcher; with an introductory chapter by P. Squires and a foreword by EG Bowen.* Cambridge University Press, 1962.

Fulchignoni, M., et al. Titan's physical Characteristics measured by the Huygens Atmospheric Instrument (HASI). Nature 438, 785-791. (2005)

Griffith, C. A., et al. Radiative transfer analysis of Titan's tropical atmosphere. Icarus 218, 975-988 (2012).

Lamb, Dennis, and Johannes Verlinde. *Physics and chemistry of clouds*. Cambridge University Press, 2011.

Lora, Juan M., Jonathan I. Lunine, and Joellen L. Russell. "GCM simulations of Titan's middle and lower atmosphere and comparison to observations." *Icarus* 250 (2015): 516-528.

Lorenz, Ralph, and Jacqueline Mitton. *Titan unveiled*. Princeton University Press, 2010.

Niemann, H. B., *et al.* The abundances of constituents of Titan's atmosphere from the GCMS instrument on the Huygens probe, Nature, 438, 779–784 (2005*).*

Matsuno, Taroh. "Quasi-geostrophic motions in the equatorial area." *Journal of the Meteorological Society of Japan. Ser. II* 44.1 (1966): 25-43.

Mitchell, J. L., et al. The dynamics behind Titan's methane clouds. P. Natl. Acad. Sci. 103, 18421–18426 (2006).

Mitchell, J. L., The drying of Titan's dunes: Titan's methane hydrology and its impact on atmospheric circulation, J. Geophys. Res., 113, E08015 (2008), doi:10.1029/2007JE003017.

Mitchell, J., Pierrehumbert, R., Frierson, D. & Caballero, R. The impact of methane thermodynamics on seasonal convection and circulation in a model Titan atmosphere. Icarus 203, 250–264 (2009).

Mitchell, Jonathan L., and Geoffrey K. Vallis. "The transition to superrotation in terrestrial atmospheres." *Journal of Geophysical Research: Planets* 115.E12 (2010).

Mitchell, J. L. Locally enhanced precipitation organized by planetary-scale waves on Titan. Nat. Geo., 589-592 (2011).

Müller-Wodarg, Ingo, et al., eds. *Titan: Interior, surface, atmosphere, and space environment*. Vol. 14. Cambridge University Press, 2014.

Niemann, H. B., et al. "The abundances of constituents of Titan's atmosphere from the GCMS instrument on the Huygens probe." *Nature* 438.7069 (2005): 779-784.

Porco, Carolyn C., et al. "Cassini imaging science: Instrument characteristics and anticipated scientific investigations at Saturn." *Space Science Reviews* 115.1-4 (2004): 363-497.

Pruppacher, Hans R., and James D. Klett. *Microphysics of Clouds and Precipitation: Reprinted 1980.* Springer Science & Business Media, 2012.

Rannou, P., F. Montmessin, F. Hourdin, and S. Lebennois, The latitudinal distribution of clouds on Titan, Science, 311, 201–205 (2006), doi:10.1126/science.1118424.

Sagan, C. Titan in 2097. Planetary and Space Science, 887 (1996).

Schaller, E. L., H. G. Roe, T. Schneider, and M. E. Brown. "Storms in the tropics of Titan." *Nature* 460, no. 7257 (2009): 873-875.

Seinfeld, J. H., & Pandis, S. N. *Atmospheric chemistry and physics from air pollution to climate change*. New York: Wiley, 2006.

Taylor, F. W. *Planetary atmospheres*. Oxford: Oxford University Press, 2010.

Tokano, T. Meteorological assessment of the surface temperatures on Titan: constraints on the surface type. *Icarus* **173**, 222–242 (2005).

Turtle, E. et al. Seasonal changes in Titan's meteorology. Geophys. Res. Lett. 38, L03203 (2011).

Wheeler, Matthew, and George N. Kiladis. "Convectively coupled equatorial waves: Analysis of clouds and temperature in the wavenumber–frequency domain." *Journal of Atmospheric Sciences* 56.3 (1999): 374-399.

Yamamoto, Masaru. "Equatorial Kelvin-like waves on slowly rotating and/or small-sized spheres: Application to Venus and Titan." *Icarus* 322 (2019): 103-113.

Yau, Man Kong, and Roddy Rhodes Rogers. *A short course in cloud physics*. Elsevier, 1996.

Weblinks:

Robert Nemiroff & Jerry Bonnell, Astronomy Picture of the Day. (n.d.). *APOD: 2006 February 15*. Retrieved May 30, 2013. URL http://apod.nasa.gov/apod/ap060215.html

NASA Jet Propulsion Laboratory. *Cassini-Huygens - Saturn Missions* (n.d.). Retrieved January 23, 2013.URL http://www.jpl.nasa.gov/missions/cassini-huygens/

U.S. Geological Survey, ISIS - Integrated Software for Imagers and Spectrometers. Retrieved July 2, 2013 URL https://isis.astrogeology.usgs.gov/

Morphed Integrated Microwave Imagery at CIMSS, SSMI/SSMIS/TMI-derived Total Precipitable Water - North Atlantic. (n.d.). *MIMIC-TPW*. Retrieved December 5, 2013. URL http://tropic.ssec.wisc.edu/real-time/mimic-tpw/natl/main.html

NASA Jet Propulsion Laboratory. Voyager - The Interstellar Mission. (n.d.). *Voyager - The Interstellar Mission*. Retrieved July 10, 2013, from http://voyager.jpl.nasa.gov

Dortmund Data Bank. Welcome to DDBST GmbH. (n.d.). *DDBST*. Retrieved June 6, 2013. URL http://www.ddbst.com